E.O. Paton Electric Welding Institute of the National Academy of Science of Ukraine
International Association «Welding»

The Paton Welding Journal

09
2022

International Scientific-Technical and Production Journal ◊ Founded in January 2000 (12 Issues Per Year)

Address of Editorial Board
E.O. Paton Electric Welding Institute, 11 Kazymyr Malevych Str. (former Bozhenko), 03150, Kyiv, Ukraine
Tel./Fax: (38044) 205 23 90, E-mail: journal@paton.kiev.ua
https://patonpublishinghouse.com/eng/journals/tpwj

State Registration Certificate 24933-14873 ПР from 13.08.2021
ISSN 0957-798X, DOI: http://dx.doi.org/10.37434/tpwj

Subscriptions, 12 issues per year:
$384 — annual subscription for the printed (hard copy) version, air postage and packaging included;
$312 — annual subscription for the electronic version (sending issues in pdf format or providing access to IP addresses).

Representative Office of «The Paton Welding Journal» in China:
China-Ukraine Institute of Welding, Guangdong Academy of Sciences
Address: Room 210, No. 363 Changxing Road, Tianhe, Guangzhou, 510650, China.
Zhang Yupeng, Tel: +86-20-61086791, E-mail: patonjournal@gwi.gd.cn

The content of the journal includes articles received from authors from around the world in the field of welding, metallurgy, material science and selectively includes translations into English of articles from the following journals, published by PWI in Ukrainian:
- Automatic Welding (https://patonpublishinghouse.com/eng/journals/as);
- Technical Diagnostics & Nondestructive Testing (https://patonpublishinghouse.com/eng/journals/tdnk);
- Electrometallurgy Today (https://patonpublishinghouse.com/eng/journals/sem).

CONTENTS

ORIGINAL ARTICLES

INFORMATION

*Translated Article(s) from «Automatic Welding», No. 9, 2022.

**Translated Article(s) from «Electrometallurgy Today», No. 3, 2022.

DOI: https://doi.org/10.37434/tpwj2022.09.01

INFLUENCE OF ELECTRODE SHAPE ON STRESS-STRAIN STATE OF AMg6 ALLOY DURING ITS ELECTRODYNAMIC TREATMENT

L.M. Lobanov[1], M.O. Pashchyn[1], O.L. Mikhodui[1], A.A. Grynyuk[1], P.V. Honcharov[1], A.O. Alyoshyn[1], T.G. Solomiychuk[1], Yu.M. Sydorenko[2], P.R. Ustymenko[2], Yuhui Yao[3]

[1]E.O. Paton Electric Welding Institute of the NASU
11 Kazymyr Malevych Str., 03150, Kyiv, Ukraine
[2]National Technical University of Ukraine «Igor Sikorsky Kyiv Polytechnic Institute»
37 Peremohy Prosp., 03056, Kyiv, Ukraine
[3]Shenzhen Hanzhizi Science and Technology Co., Ltd. 6th Floor, Building B,
Bantian International Center, 5 Huancheng South Rd., Longgang District, Shenzhen,
Guangdong, PRC

ABSTRACT

The advantages of using electrodynamic treatment (EDT) of metal in the welding process as compared to EDT at room temperature were substantiated. The advantages and disadvantages of using electrode for EDT in the form of a cylindrical rod and a roller in the welding process were considered. Using the method of mathematical modeling in planar and axisymmetric statements, the effect of a shape of the electrode-indenter on stress-strain state of the welded plate from aluminium AMg6 alloy after applying the dynamic EDT component was evaluated. The features and differences of creation and use of developed mathematical models were described. The distribution of values of the stress-strain state throughout the thickness of the plate was determined, in particular, the values of the zone of plastic deformations and stresses during interaction of the plate with the electrode-indenter moving at a speed of 5 m/s. It was found that the use of a cylindrical indenter with a hemispherical working end (of axisymmetric shape) as compared to the roller (of planar elongated shape) is more effective from the standpoint of optimizing the residual stressed state in the plate. The use of a cylindrical indenter leads to the formation of compressive stresses in the plate with the values up to –120 MPa. This should have a positive effect on the distribution of residual welding stresses under the action of the dynamic EDT component.

KEYWORDS: electrodynamic treatment, aluminium alloy, impact interaction, mathematical modeling, residual stresses, plastic deformations, electrode-indenter, movement, elastoplastic environment

INTRODUCTION

The problem of regulating residual welding stresses and deformations in structures of aluminium alloys is relevant, which is caused by their use in various industries and transport, where stress-strain states significantly affect the service characteristics of products.

A prospective method of regulating stress-strain states of structures is electrodynamic treatment (EDT) of welded joints, which is based on initiating electrodynamic forces in the metal of products occurring while passing electric current pulse (ECP) in the latter [1, 2]. The use of EDT allows changing the stress-strain state (SSS) of welded joints by means of point impacts of the electrode-indenter in the welded joint zone with a simultaneous ECP passing. During EDT, the welded joint metal is subjected to electrodynamic action that initiates electroplastic effect in the treatment zone and, as a result, relaxation of residual welding stresses [3].

Realization of EDT of longitudinal welded joints, including also in the welding process, requires expanding capabilities of the method by optimizing the conditions of contact interaction of the electrode for EDT with the metal surface to be treated. The realization of the EDT method in the welding process provides shortening in the time of manufacturing a welded structure as a result of transition from successive to simultaneous welding and treatment. It also creates opportunities to automate this technology.

The hardware for the method is limited by organization of a synchronous movement of the welding torch and the electrode device for EDT – the "Torch + EDT Electrode" system. I.e., the "Torch + EDT Electrode" system is constantly moving along the weld. This requires structural and technological solutions, which are aimed at a qualitative providing of a discrete dynamic interaction of the contact surface of the EDT electrode, which moves constantly along the weld. At the same time, the interaction occurs at the moment of passing ECP throughout the electrode to the welded joint metal.

Two variants of interaction were considered. During realization of the first variant, a dynamic contact of the hemispherical end of a cylindrical electrode with a plane surface of the welded joint, subjected to

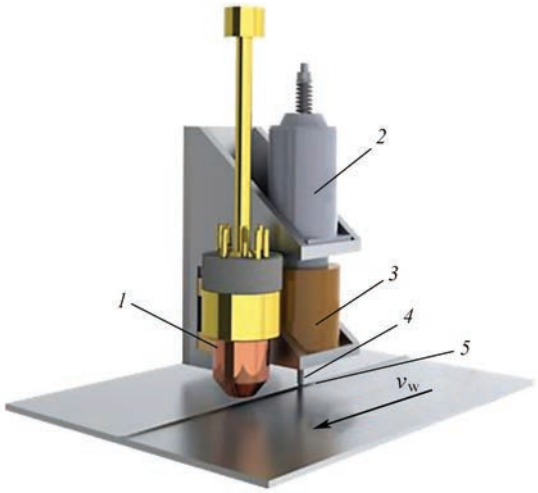

Figure 1. Variant of circuit diagram of contact of EDT electrode in the form of a cylinder with weld metal: *1* — torch for welding; *2* — inductor of linear vertical movement; *3* — electrode system; *4* — EDT electrode; *5* — weld; v_w — welding direction

EDT, was realized [1–3]. At the second variant, a dynamic contact of the surface of a cylindrical roller, rolled on the surface of the weld, subjected to EDT, was realized.

Figure 1 presents the circuit of a cylindrical electrode *4* with the weld metal *5*. The contact interaction of the hemispheric end of the electrode with a plane surface of the metal being treated was carried out using the inductor of a linear vertical movement *2*. The inductor was located along the total vertical axis with the electrode system *3* for fixing the electrode *4*. The disadvantages of the circuit in Figure 1 include the need in a discrete positioning of the electrode relative to the longitudinal central weld axis and counteracting jamming of the electrode in the process of continuous longitudinal movement of the "Torch + EDT Electrode" system in the welding process.

Figure 2 presents the circuit diagram of the contact of the electrode *4* in the form of a roller with the metal of the welded joint *5*, which is mounted on the assembly plate *6*. The roller has a shape of a cylinder that rolls on the surface of the welded joint. The contact interaction of the roller surface was carried out along the generating line of the cylinder using a linear displacement inductor *1*. The inductor was co-located with the system of fixing *3* the roller, fixed in the casing *2*. This design is simpler in realization than that presented in Figure 1, where there is a series of discrete dynamic contacts of the electrode with the surface of the weld in the process of producing a weld. In the design of the electrode in the form of a roller, the discreteness is eliminated due to a continuous rolling of the latter along the weld, which is accompanied by periodic ECP passing into the weld (through the roller).

When comparing the diagrams in Figures 1 and 2, it should be noted that the latter is simpler in realization because of elimination of the discreteness of a contact interaction due to rolling of the electrode on the weld surface. Until now, no studies of the influence of the electrode shape on SSS of the metal in the contact area after EDT have been conducted. Therefore, the evaluation of residual SSS of the metal, which is a consequence of its dynamic contact interaction with the electrode in the form of a cylinder or a roller, is relevant.

Some issues of experimental determination of stresses after welding were considered in [1], but such methods allow finding values of welding stresses only on the surface of the body and as a result of its partial destruction. In order to more fully evaluate SSS of such structures, modern means of mathematical modeling are used. The paper [2] describes the results of computer modeling of the process of impact interaction of the electrode-indenter with the welded plate (only dynamic EDT component was considered), which was carried out on the basis of the Prandtl–Reuss ratios [3], describing the movement of the medium

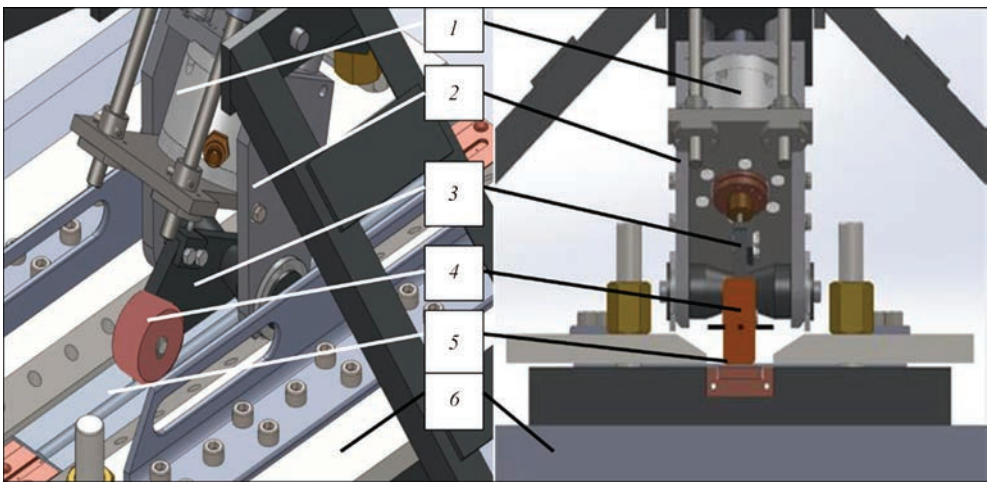

Figure 2. Variant of circuit diagram of contact of EDT electrode in the form of a roller with weld metal: *1* — inductor of linear movement; *2* — casing of roller fixation; *3* — roller fixation system; *4* — EDT electrode; *5* — welded joint; *6* — assembly plate

in the planar two-dimensional Lagrangian statement using the ANSYS/LS-DYNA software. It should be noted that the use of such a statement corresponds to the modeling of the EDT process of a plate with a planar electrode-indenter of an infinite length.

At the same time, EDT is carried out by electrode-indenters of an axisymmetric shape, for example, in a shape of a cylinder. Then, modeling of the EDT process with such an indenter should be carried out using another — axisymmetric statement.

Thus, the aim of the work is a mathematical evaluation of the influence of the electrode-indenter shape on the stress-strain state of the plate after applying the dynamic electrodynamic treatment component.

CALCULATION (MATHEMATICAL) MODEL OF THE PROBLEM

The calculation scheme of the process of treatment of the welded plate by the dynamic EDT component is presented in Figure 3.

In Figure 3, it is seen that in the process of impact interaction, two bodies take part. The first is a plate (*2*) with a thickness of 4 mm and a width of 50 mm, which is made of AMg6 alloy and is located on a completely rigid surface (desktop *3*). The second body is a copper electrode-indenter (*1*), which moves in the direction of the plate at a speed v_0 = 5 m/s.

A shape of the cross-section of the indenter conventionally consists of two elementary figures: a rectangle with a width of 20 mm and a height of 30 mm and a semicircle with a radius of 10 mm.

Since the cross-sections of the plate and indenter have geometric symmetry, then in Figure 3, only their right halves, relative to the *Y* axis (indenter line), are presented.

Thus, mathematical calculations using the planar statement will correspond to modeling the EDT process of a plate using a roller. A roller was modeled in the form of a plane electrode with a cross-section located across the conditional weld (Figure 4, *a*). This generally corresponds to the circuit diagram shown in Figure 2.

At the same time, calculations using the axisymmetric two-dimensional statement will correspond to modeling the EDT process of a plate by a cylindrical electrode with a hemispherical end. The electrode is located along the impact line (along the *Y* axis in Figure 3), as is shown in Figure 4, *b*. This generally corresponds to the circuit diagram shown in Figure 1.

The main difference between the two mathematical models mentioned above is that in the planar statement the contact of the electrode-indenter with the plate is realized along the line, and in the axisymmetric one — at the point.

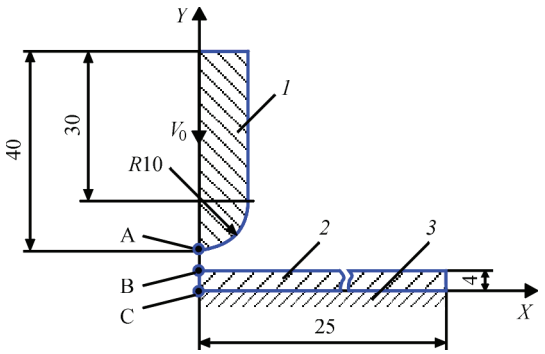

Figure 3. Calculation scheme of the process of treatment of the plate with the dynamic EDT component: *1* — electrode-indenter; *2* — treated plate; *3* — absolutely rigid table. Points along the impact line: A — on the surface of the indenter; B — on the facial surface of the plate; C — on the back surface of the plate

The finite-element model of the problem in both statements had the same quantity of finite elements and nodes, namely: a quantity of finite elements (SOLID 162 type) is 128203 units; a quantity of nodes is 131042 units. The behavior of materials of the plate and the electrode-indenter was described using a rheological elastoplastic model of materials, in which the value of the dynamic yield strength is assumed to be equal to the yield strength σ_y. The values of parameters of these models were as follows:

- AMg6 alloy (plate): density ρ = 2640 kg/m^3; Young's modulus of elasticity E = 71 GPa; Poisson's ratio μ = 0.34; yield strength σ_y = 150 MPa;
- copper of M1 grade (electrode-indenter): density ρ = 8940 kg/m^3; Young's modulus of elasticity E = = 128 GPa; Poisson's ratio μ = 0.35; yield strength σ_y = 300 MPa.

Thus, in order to evaluate the influence of a shape of the electrode-indenter (in planar or axisymmetric statements) on the effectiveness of the dynamic EDT component, a mathematical modeling of the process of its interaction with the plate metal at a contact speed V_c = 5 m/s was carried out. The value of V_c was set by the charging voltage of the capacitors U_{ch} = 500 V

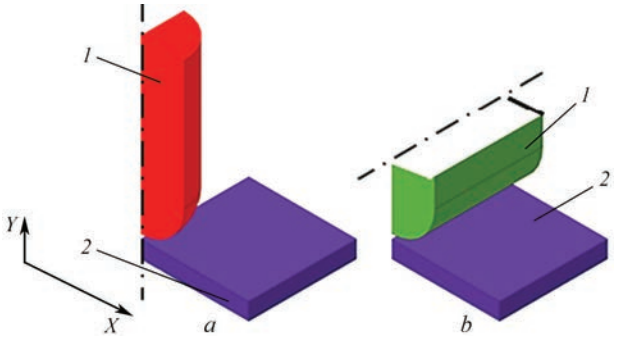

Figure 4. Appearance of electrode-indenter of a different shape, where *X* and *Y* is the direction of action of stress-strain state components (where *1* — electrode; *2* — plate): *a* — cylinder with a hemispherical working end; *b* — roller

Table 1. Calculation parameters of interaction between the electrode and the plate at the place of contact

Type of symmetry	Duration of contact, μs	Depth of penetration of the indenter into the plate, mm	Depth of contact zone in the plate, mm	Width of contact zone in the plate, mm
Planar	86	0.176	0.168	1.89
Axial	128	0.285	0.266	2.56

with a capacity of C = 6600 μF. This provided the energy of a single electrodynamic action E_{EDT} = 825 J.

The modeling was carried out using the ANSYS/LS-DYNA software based on the Prandtl–Reuss ratios, which describe the movement of an elastoplastic medium.

MODELING RESULTS AND THEIR COMPARISON

The conducted numerical calculations showed the main differences in the process of interaction of the electrode-indenter of a different shape with the plate, which are summarized in Table 1.

From the data in Table 1, it is seen that the duration of a contact between the bodies in the axisymmetric statement is by 42 μs (50 %) longer than the duration in the planar one. This is explained by the peculiarities of the energy exchange processes between the electrode-indenter and the plate. Accordingly, as the interaction time increases, deformations in the contact zone also grow, which affects its dimensions in the plate. The depth of the indenter penetration was determined as the maximum movement of the point A (see Figure 3) into the middle of the plate from its surface, and accordingly, the depth of the contact zone was determined as the movement of the point B (see Figure 3) from the initial position to the position corresponding to the end of the contact.

An increase in the depth of the contact zone by 55 % and its width by 35 % in the axisymmetric statement as compared to the planar one leads to a corresponding increase in the zone of plastic deformation and the amount of effective plastic deformations ε^p_{eff} across the thickness of the plate (Figure 5).

The distribution of ε^p_{eff} in the planar statement propagates over a half of the thickness of the plate (2 mm) and has a shape of a segment of a circle with a radius of 2 mm (Figure 5, *a*). In the axisymmetric statement, the zone of plastic deformation reaches the back surface of the plate and has a shape close to a trapezoid, the upper base of which is 8 mm long, and the lower one is 4 mm (Figure 5, *b*). Analyzing the data of Figure 5, it should be noted that the point contact interaction of the hemispherical end (axisymmetric statement) contributes to a greater intensity of plastic deformation as compared to a linear one (planar statement). When comparing the data of Figure 5, *a*, *b*, it can be seen that propagation of the zone of plastic deformation along the cross-section of the plate with the axisymmetric statement is greater than in the planar one.

Also from Figure 5, it is seen that in the planar statement, the maximum values ε^p_{eff} are formed on the contact surface of the plate with the electrode-indenter in the cross-section area near the plane of symmetry. In the case of the axisymmetric problem, the opposite occurs. As is seen from Figure 5, *b*, the peak values ε^p_{eff} are shifted by 1.8–2.0 mm from the impact line (axis of symmetry).

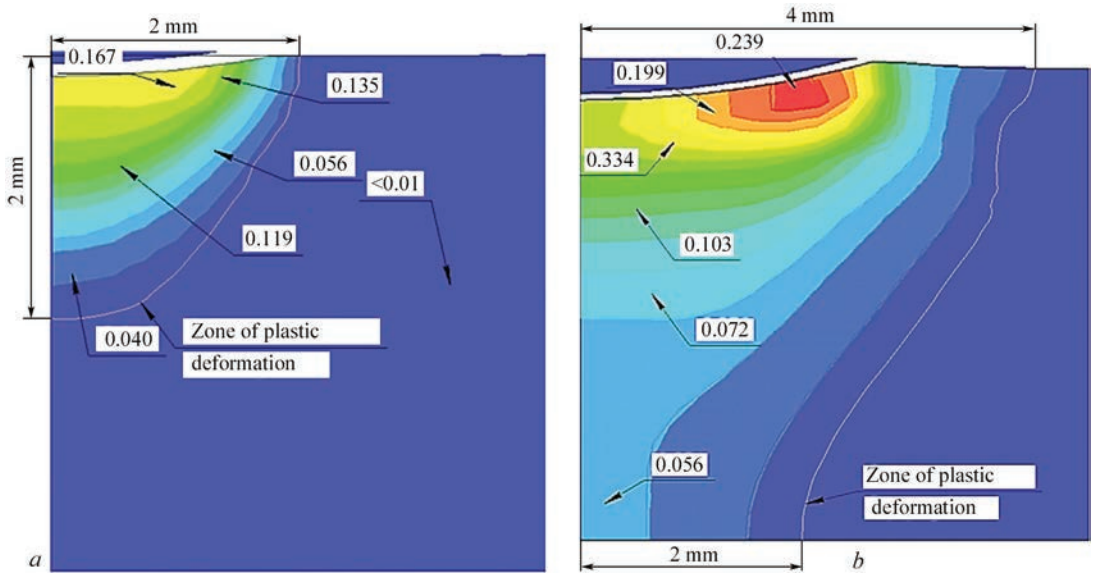

Figure 5. Calculation distribution of effective plastic deformations ε^p_{eff} in the middle of the plate in planar (*a*) and axisymmetric (*b*) statements

For comparison, the values of maximum ε^{p}_{eff} and the values ε^{p}_{eff} at the points B and C (Figure 3), located along the impact line, are given in Table 2. It is seen of the data from Table 2 that the use of an axisymmetric electrode-indenter as compared to the planar one leads to an increase in the maximum ε^{p}_{eff} by more than 1.4 times. When comparing the values ε^{p}_{eff} at the points B and C (see Table 2), it is seen that the change in a shape of the electrode-indenter almost does not affect ε^{p}_{eff} at the point B (the difference in values does not exceed 10 %), but ε^{p}_{eff} at the point C differs by an order. At the same time, the values ε^{p}_{eff} at the point C for both types of symmetry (variants of the indenter shape) are almost 4 times smaller than at the point B, which is explained by a gradual dissipation of the kinetic energy of the indenter throughout the thickness of the plate.

Based on the differences of the deformation pattern presented in Figure 5, it is relevant to evaluate the influence of each component of residual deformations on the final value ε^{p}_{eff} (Figure 6). The data of Figure 6, *a* indicate an almost uniform distribution of ε^{p}_{x} over the thickness of the plate in the planar statement, where the values of this component change within the range from –0.01 to 0.01. In the case of the axisymmetric problem, at the point of contact, a zone of tensile deformations with the peak values of about ε^{p}_{x} = 0.08 is created. In this case, under the pressure of the electrode-indenter, the material from the central tension zone is flowing in the radial direction from the impact line. This leads to the formation of compres-

Table 2. Values of effective plastic deformations ε^{p}_{eff} at different types of symmetry

Type of symmetry	Maximum values ε^{p}_{eff}	Values ε^{p}_{eff} on surfaces of the plate	
		Facial (point B, Figure 3)	Back (point C, Figure 3)
Planar	0.171	0.165	0.004
Axial	0.239	0.151	0.038

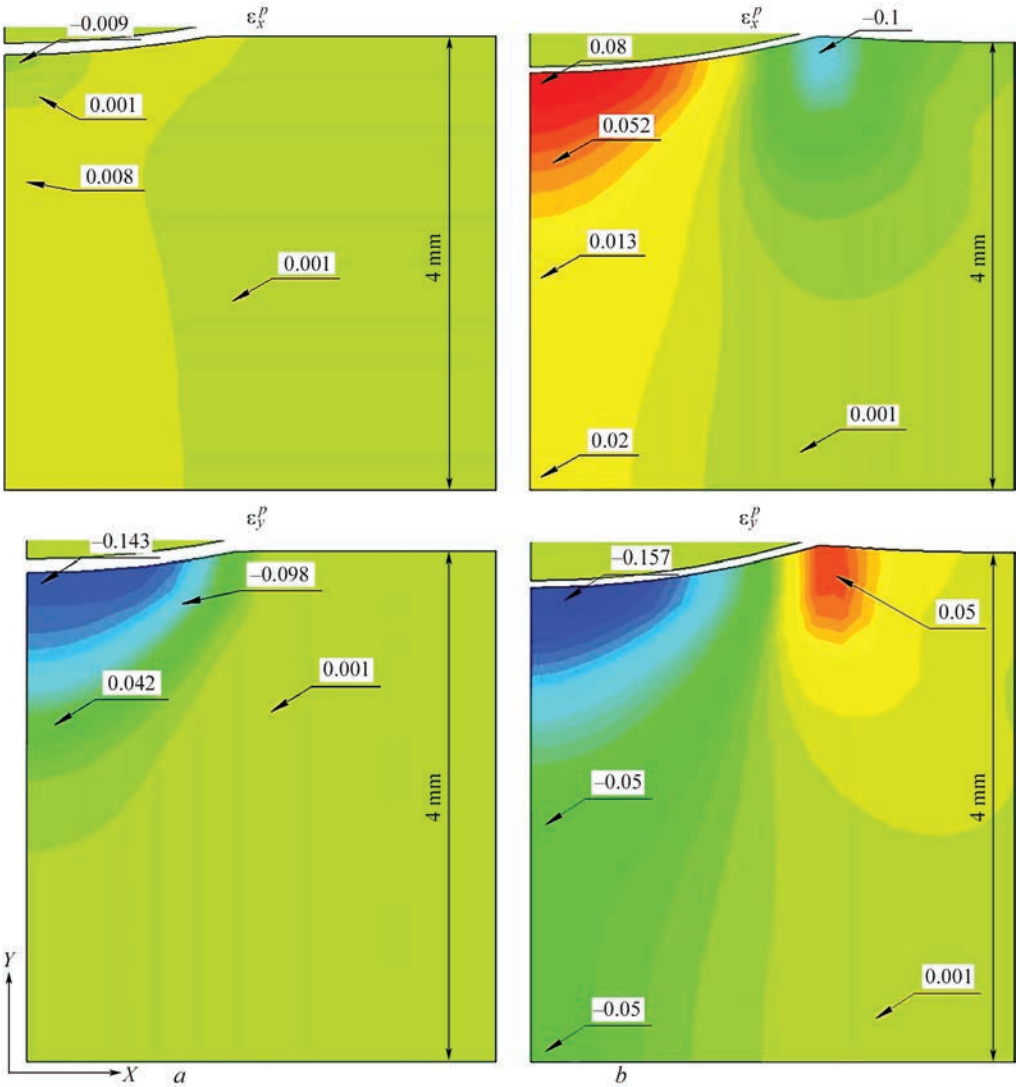

Figure 6. Calculation distribution of components of plastic deformations ε^{p}_{x}, ε^{p}_{y} for planar (*a*) and axisymmetric (*b*) statements

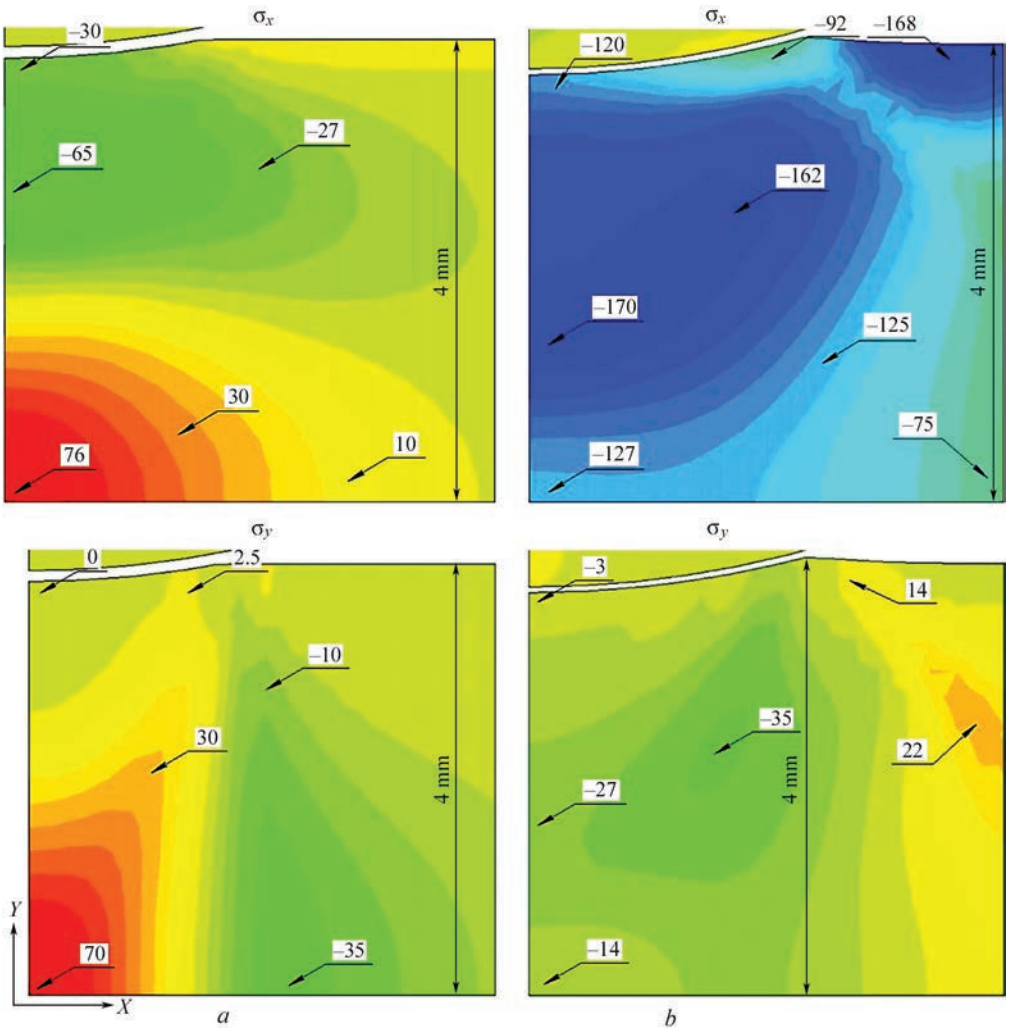

Figure 7. Distribution of values of components of residual stresses σ_x, σ_y (MPa) for planar (*a*) and axisymmetric (*b*) statements

sion deformations $\varepsilon^p_{eff} = -0.1$ on the facial surface of the plate of a sufficiently localized zone, which generally does not affect the overall strain state of the tested cross-section of the plate. When comparing the deformation patterns of Figure 6, it can be seen that the axisymmetric statement (Figure 4, *b*) provides a more optimal distribution of plastic deformations (as compared to the planar one — Figure 4, *a*), where tensile ε^p_{eff} have larger values. The consequence of this is the formation of residual compression stresses larger in values.

If we consider the distribution of values of another component of deformations ε^p_y then regardless of a shape of the indenter at the point B (Figure 3), the formation of almost identical zones of compression deformations is observed. In this place, the maximum values for the problem in the planar statement $\varepsilon^p_y = -0.14$ (Figure 6, *a*), and in the axisymmetric one $\varepsilon^p_y = -0.16$ (Figure 6, *b*).

As is known, a strain state is a consequence of action of the corresponding stresses in the structure. In order to analyze the distribution of values of the stressed state components over the thickness of the plate, appropriate calculation patterns of the distribution of σ_x and σ_y were plotted (Figure 7).

From Figure 7, it is seen that depending on a shape of the electrode-indenter (conditions of symmetry of the mathematical model), the residual stressed state formed in the plate has significant differences. For the problem in the planar statement, the distribution of residual stresses σ_x (directed perpendicular to the impact line — Figure 3) is formed in the form of two characteristic zones (Figure 7, *a*). The first is the compression zone near the facial surface of the plate with the values $\sigma_x = -22$ MPa. The second one is the tensile zone near the back surface of the plate with the stress values up to $\sigma_x = 76$ MPa. In the axisymmetric statement (Figure 7, *b*) only one zone is formed over the whole thickness of the plate — the zone of compression stresses with the maximum value up to $\sigma_x = -120$ MPa.

According to the results of analysing the pattern of distributing values of the component of the stressed state σ_y (directed along the impact line — Figure 3), which is formed in the case of using a plane indenter, it is possible to see an almost rectangular zone of ten-

Table 3. Calculation values of residual stressed state components σ_x and σ_y across the thickness of the plate (from the point B to the point C)

Type of symmetry	Stressed state component	Coordinate of the point across the thickness of the plate (along the impact line), mm				
		0 (point B)	1	2	3	4 (point C)
Planar	σ_x, MPa	–25	–56	–23	46	76
	σ_y, MPa	0.1	0.01	17	53	80
Axial	σ_x, MPa	–131	–155	–161	–164	–128
	σ_y, MPa	–0.08	–9	–15	–20	–5

sile stresses (Figure 7, *a*). The maximum values are reached by tensile stresses on the back surface of the plate (point C in Figure 3) σ_y = 76 MPa. Also, on the back surface at a distance of 2.5 mm from the impact line, the zone of compression stresses σ_y = –36 MPa is formed. The minimum values of tensile stresses are reached on the facial surface (point B) σ_y = 0.01 MPa.

In the axisymmetric statement (Figure 7, *b*), a pattern of stresses is somewhat different. Throughout the thickness of the plate, an almost uniform distribution of values of the component σ_y of compression stresses is formed. The difference between the maximum and minimum value of this component of stresses along the impact line does not exceed 20 MPa.

The calculation values of residual stressed state components σ_x and σ_y across the thickness of the plate (from the point B to the point C) are given in Table 3. The comparison of values of the stressed state components along the impact line (Table 3) shows that unlike a plane electrode-indenter, the use of an axisymmetric indenter leads to the formation of almost uniform distribution of both stress components σ_x and σ_y.

In addition, the use of a plane electrode-indenter (roller) leads to the formation of both compression stresses as well as undesired tensile stresses with values that can reach a half of the value of the yield strength of the material. However, the use of the electrode-indenter of an axisymmetric shape leads to the formation of both components of stresses as compression stresses, the values of which can reach –120 MPa. This can have a positive effect on residual stressed states of welded structures even applying only the dynamic EDT component [4].

But, as is shown above, the practical use of the electrode in the form of a roller has advantages over the cylinder from the standpoint of simplicity and ease of use. Considering the abovementioned, in the future, the studies of stressed states of welded structures after EDT with the use of a roller at higher power characteristics of electrodynamic actions, in particular, at an increase of ECP frequency should be provided.

CONCLUSIONS

1. The use of a cylindrical electrode-indenter with a hemispherical working end for EDT as compared to a plane elongated electrode in the form of a roller, at the same speed of their movement being 5 m/s, results in:

● distribution of the zone of effective plastic deformations ε_{eff}^{p} to the whole thickness of the plate, which has a shape close to a trapezoid (in the case of a plane indenter, the zone ε_{eff}^{p} extends to only half of a thickness of the plate and has a shape of a circle segment), and the values of maximum deformations are 1.4 times higher than similar values formed from the action of a plane indenter.

● formation of almost uniform distribution of both components of a stressed state — both σ_x and σ_y across the thickness of the plate, which, unlike the other (planar) statement of the problem are compression stresses, the values of which can reach –120 MPa.

2. The use of an axisymmetric electrode-indenter provides a more effective regulation of the dynamic EDT component and stressed state of the plate throughout the whole its thickness provided that other things are equal, which helps to reduce the level of residual welding tensile stresses.

3. It was proved that the practical use of the electrode in the form of a roller has advantages over the cylinder from the standpoint of simplicity and ease of use. Taken into account the abovementioned, the study of stressed states of welded joints after EDT with the use of a roller at higher power characteristics of electrodynamic actions is promising for optimizing the service characteristics of welded structures.

REFERENCES

1. Lobanov, L.M., Pivtorak, V.A., Savitsky, V.V., Tkachuk, G.I. (2006) Procedure for determination of residual stresses in welded joints and structural elements using electron speckle-interferometry. *The Paton Welding J.*, **1**, 24–29.
2. Lobanov, L.M., Pashchyn, M.O., Mikhodui, O.L. et al. (2021) Modeling of stress-strain states of AMg6 alloy due to impact action of electrode-indenter in electrodynamic treatment. *The Paton Welding J.*, **6**, 2–11. DOI: https://doi.org/10.37434/tpwj2021.06.01
3. Sidorenko, Yu.M., Shlenskii, P.S.(2013) On the assessment of stress-strain state of the load-bearing structural elements in

the tubular explosion chamber. *Strength of Materials*, 45(**2**), 210–220.
4. Lobanov, L.M., Pashchin, N.A., Mikhodui, O.L., Sidorenko, Y.M. (2018) Electric pulse component effect on the stress state of AMg6 aluminium alloy welded joints under electrodynamic treatment. *Strength of Materials*, 50(**2**), 246–253.

ORCID
L.M. Lobanov: 0000-0001-9296-2335,
M.O. Pashchyn: 0000-0002-2201-5137,
O.L. Mikhodui: 0000-0001-6660-7540,
A.A. Grynyuk: 0000-0002- 6088-7980,
P.V. Honcharov: 0000-0002-1980-2340,
A.O. Alyoshyn: 000-001-9696-6800,
T.G. Solomiychuk: 0000-0002-3038-8291,
Yu.M. Sydorenko: 0000-0001-8780-9459,
P.R. Ustymenko: 0000-0002-5318-2675,
Yuhui Yao: 0000-0001-7196-1317

CONFLICT OF INTEREST
The Authors declare no conflict of interest

CORRESPONDING AUTHOR
M.O. Pashchyn
E.O. Paton Electric Welding Institute of the NASU
11 Kazymyr Malevych Str., 03150, Kyiv, Ukraine.
E-mail: svarka2000@ukr.net

SUGGESTED CITATION
L.M. Lobanov, M.O. Pashchyn, O.L. Mikhodui, A.A. Grynyuk, P.V. Honcharov, A.O. Alyoshyn, T.G. Solomiychuk, Yu.M. Sydorenko, P.R. Ustymenko, Yuhui Yao (2022) Influence of electrode shape on stress-strain state of AMg6 alloy during its electrodynamic treatment. *The Paton Welding J.*, **9**, 3–10.

JOURNAL HOME PAGE
https://pwj.com.ua/en

Received: 19.07.2022
Accepted: 11.11.2022

DOI: https://doi.org/10.37434/tpwj2022.09.02

INFLUENCE OF INOCULANTS ON THE FEATURES OF WELD STRUCTURE FORMATION IN LOW-ALLOYED STEELS (REVIEW)

V.V. Holovko

E.O. Paton Electric Welding Institute of the NASU
11 Kazymyr Malevych Str., 03150, Kyiv, Ukraine

The paper presents a review of studies on the influence of inoculation of dispersed refractory compounds into the weld pool on formation of weld metal microstructure in low-alloyed high-strength steels. Features of the process of primary structure formation are considered in the presence of refractory nonmetallic inclusions in the liquid metal, as well as on the interface of δ-dendrites and γ-phase. Possibilities of inoculant influence on the temperature range of bainite transformations, formation of microstructural components with higher brittle fracture resistance, and improvement of weld metal toughness values are shown.

KEYWORDS: low-alloyed steels, welding, structure, inoculants, δ-dendrites, austenite, bainite

INTRODUCTION

Low-alloyed steels of higher and high strength (HSLA steels) have become widely accepted in fabrication of welded metal structures. Owing to application of special welding technologies and selection of appropriate welding consumables, welded joints of these steels are capable of providing high values of strength, ductility and toughness. Numerous studies were published in recent years in special literature devoted to the problems of formation of metal microstructure in welded joints of HSLA steels. Particular attention is paid here to the role of bainitic components of weld microstructure. Numerous studies, considering bainite initiation and growth in BCC iron alloys are indicative of the fact that the features of the process of formation of this microstructure are still not quite clear. To date two main mechanisms of γ-> α transformation in iron alloys have been quite well studied and described, namely the diffusion and the shear mechanism. Diffusion mechanism occurs at temperatures close to A_{c3}. It is described by the process of carbon redistribution between γ-(austenite) and α-phase (ferrite) and realized as pearlite transformation. The shear mechanism takes place at temperatures close to A_{c1}, it runs almost instantly and is realized in the form of martensite transformation. The complexity of description of the mechanism of intermediate transformation (bainite) consists in that it involves both these processes. There is a quite large number of factors, which determine the priority of this or that mechanism during bainite structure formation. This is exactly why the bainite structures are characterized by a considerable quantity of morphological forms (upper, lower, globular, acicular, lath, lamellar, intragranular, polyhedral bainite, etc.). Depending on the kind and composition, each of these structures has its values of strength, ductility and toughness. Formation of a particular kind of bainite in the weld metal has a significant influence on the mechanical properties of welded joint as a whole, so that a more profound understanding of the features of the processes of bainite initiation and development requires further investigations in order to expand our knowledge base on this subject.

The main alloying element, used in HSLA steels to increase the strength values, is carbon. Increase of the content of carbon (precipitating with formation of carbides) promotes steel hardening. Carbides, however, also lower brittle fracture resistance of the metal. To improve the steel strength, it is necessary to increase its carbon content, and, thus, more efforts are required to slow down carbide formation and their refinement. Well-known is the difference in carbide distribution between bainite, which forms at high or at low temperatures, i.e. between the intergranular and intragranular ones, respectively. In the upper region of bainite transformation, when the effectiveness of carbon diffusion in the solid solution is quite high, a considerable quantity of carbon has enough time to go beyond the grains, reach the boundaries, and precipitate in the form of carbides, while the ferrite grains proper remain free from the carbide precipitates. In the region of lower temperatures of bainite transformation, the carbon diffusion rate decreases markedly. Slower carbon diffusion, associated with lower temperature of bainite transformation, enables a certain quantity of carbon to precipitate in the oversaturated bainitic ferrite. In this case, fine dispersion of lamellar carbides in the single-crystal variant forms inside the grains, although more than one variant of carbide precipitation can be observed. Thus, both the size of primary austenite grains and the temperature range of bainite transformation have a significant role during formation of secondary microstructure.

INFLUENCE OF INOCULANTS ON PRIMARY STRUCTURE FORMATION

In general, whole technologies of low-alloyed steel welding consist in forming a fine-grained ferrite structure in the weld metal. It is believed that it should be promoted by formation of fine-grained structure of primary austenite. It should be noted that there are a lot of disputes in publications on the influence of the size of primary austenite grains on bainite transformation. Some researchers believe that the fine size of austenite grains leads to faster growth of bainite, others believe that the small grain size reduces the probability of the real transformation, and some do not notice any changes in bainite transformation at reduction of primary austenite grain size [1–3]. Differences of opinion on this issue are largely determined by the fact that initiation, growth and decomposition of primary structure, on the one hand, are poorly amenable to direct investigation because of the high temperature and speed of the processes, and on the other hand, because of a lack of experimentally confirmed physical values for description of thermodynamics and kinetics of the processes, as a perfect computer model of formation of primary structure of HSLA steels is not available. However, based on the considerations that development of metal microstructure, and of its mechanical properties, respectively, starts from formation and decomposition of the primary structure, the task of expanding our knowledge base on this question is highly relevant.

So far it is not possible to predict the size of austenite grain in the weld metal, as the factors, controlling the grain size, are by far not completely understood. The theory of grain growth envisages that nonmetallic inclusions, contained in the weld metal, should control the grain size through grain boundary blocking (Zener effect). Practice showed, however, that such an analogy is not justified, as austenite grains form as a result of δ-ferrite transformation, while Zener pinning-effect describes blocking of the grain boundaries during their growth from the liquid phase. The driving force of grain growth is usually equal to just several Joules per mole, whereas the activation energy of austenite transformation from δ-ferrite grows unlimitedly at overcooling. In this case blocking of δ/γ interfaces cannot be effective. The mechanism of blocking the boundaries of columnar austenite grains does not agree with the shape of these grains, either, as the movement of δ/γ interfaces along the direction of the maximum temperature gradient has no obvious limitations. In this case, if the pinning process were effective, the austenite grains should be isotropic as a result of their forming. North et al. in work [4] presented a description of such crystallization. However, additional investigations are needed to clarify these issues. The size of columnar austenite grain should in a certain way correlate with grain size in the base metal on the fusion line, as solidification occurs through epitaxial growth of these grains [5]. This connection, cannot be simple, however, as during solidification those grains, where the crystallographic orientation coincides with ⟨100⟩ direction, are located in parallel to the direction of the highest temperature gradient. Such grains grow quickly and inhibit the growth of grains with another crystallographic orientation. An experimental study, illustrating the influence of crystallographic texture on grain size [6], shows that nonmetallic inclusions located in the base metal (for instance, carbonitrides), can limit coarsening of weld metal grains on the fusion line and, thus, eventually result in smaller grain size in the fusion zone.

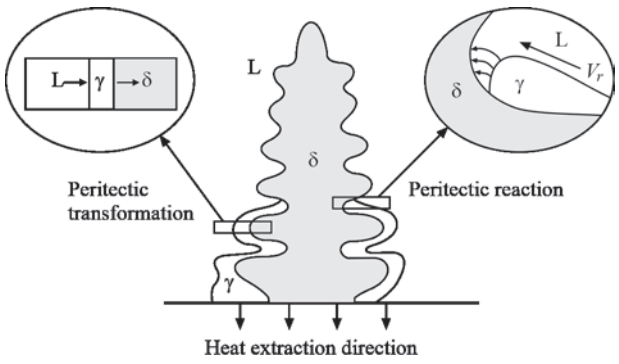

Figure 1. Mechanism of peritectic solidification [11]

When considering the processes of primary structure formation, it is necessary to take into account the fact that they proceed at contact of the three phases and are described by peritectic reactions, respectively. Peritectic crystallization of metal at its cooling occurs in two stages. At the first stage a peritectic reaction proceeds in the point of contact of three phases (L-liquid + δ-ferrite + γ-austenite) in the temperature range a little lower than the peritectic temperature, leading to separation of L-liquid and δ-ferrite with lateral growth of γ-austenite around δ/L interface. At the second stage peritectic transformation begins with thickening of the layer of γ-austenite at the expense of δ-ferrite phase and γ-austenite tip advancing into the liquid L-phase (Figure 1). Development of high-temperature laser scanning together with the confocal microscopy [7] allows observation with a high resolution of phase transformations in the high-temperature region in peritectic steel. Results of these investigations [8, 9] showed that the peritectic transient process is controlled by diffusion of the solutes. It was found that partial remelting of δ-phase also is influenced by diffusion of solutes. It is shown that γ-phase initiates and grows on the interface between δ- and L-phase, while γ-phase quickly separates them in the process of growth. A conclusion was made that the interface enrichment in carbon is increased with increase of the cooling rate that decelerates initiation of

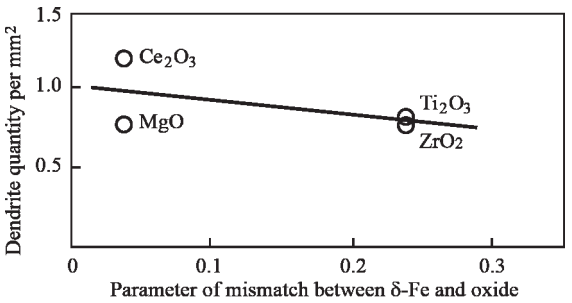

Figure 2. Dependence between the dendrite quantity and parameter of mismatch between δ-Fe and oxide [17]

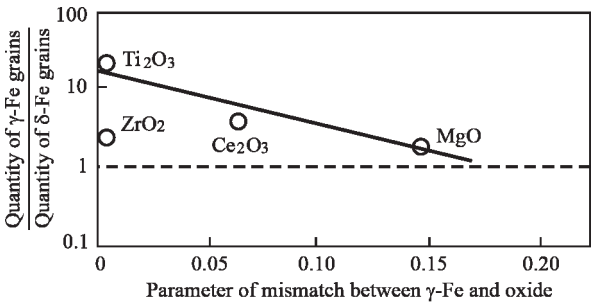

Figure 3. Dependence between mismatch parameter and density of γ-phase nucleation centers on the interface with δ-dendrite [17]

γ-phase. Moreover, it is shown [10] that the interface movement speed is influenced by elastic energy of the interface and coefficient of solute distribution.

Refractory inclusions with melting temperature above that of the metal melt, present in the thin layer on the surface of δ-dendrites, where γ-phase initiates and develops, depending on the wettability index, can be absorbed by the growing phase or can accumulate on the interfacial front and influence the interfacial energy. Experimental results given in publications confirm this conclusion. So, work [12] shows the results of investigation of the influence of inoculation of such refractory oxides as MgO, ZrO_2, Ti_2O_3, Ce_2O_3 into the steel melt. Determination of wettability index between the refractory oxides and liquid iron and δ-Fe showed that the contact angle of wettability changes depending on time and temperature of contact. This is indicative of the possibility of interfacial reactions. From the viewpoint of thermodynamics, reactions with oxygen evolution can be in place at temperatures characteristic for steel pool melts [13, 14, 17]:

$$Al_2O_3 \rightarrow 2Al + 3O, \Delta G^0 = 1225000 - 393.8T \text{ (J/mole)},$$
$$MgO \rightarrow Mg + O, \Delta G^0 = 89960 + 82.0T \text{ (J/mole)},$$
$$2TiO_2 = Ti_2O_3 + O, \Delta G^0 = 379908 - 97.069T \text{ (J/mole)},$$
$$3TiO_2 = Ti_3O_5 + O, \Delta G^0 = 387866 - 112.215T \text{ (J/mole)}.$$

It results in accumulation of decomposition products on δ→γ interface. As a result of the conducted studies, Bhadeshia et al. [15] came to the conclusion that increase of oxygen content in the steel melt does not affect the size of primary austenite grains, while authors of [16] express the idea that formation of γ-phase is influenced by accumulation of alloying elements on the interface, for instance magnesium, as a result of MgO decomposition. The density of distribution of potential centers of new phase initiation depends on the energy on the initial phase boundary. The activation energy is primarily affected by increase of grain boundary energy, as a result of increase of the content of alloying elements on them. Increase of grain boundary energy will lead to increase of the speed of formation of new phase nuclei.

Experimental data given in publications confirm this conclusion. So, work [15] gives the results of studying the influence of inoculation of such refractory oxides as MgO, ZrO_2, Ti_2O_2, Ce_2O_3 into the steel melt. It was found that formation of solidification microstructure is influenced by chemical composition of the inclusions, as well as parameter of mismatch between γ-Fe and oxide and δ-Fe and oxide (Figure 2).

Moreover, it is found that with increase of the parameter of mismatch between δ-Fe and oxide the quantity of γ-Fe grains which formed in the body of one dendrite, becomes greater (Figure 3).

INFLUENCE OF INOCULANTS ON SECONDARY MICROSTRUCTURE FORMATION

Change of primary structure morphology by inoculation of dispersed refractory compounds before welding influences formation of weld metal secondary microstructure. Work [18] gives the results of investigations on adding refractory oxides, carbides and nitrides to the weld pool. It is shown that depending on physico-chemical properties of the compounds, the inoculants influence the size of primary structure grains. Increase of primary austenite size should reduce the effectiveness of carbon diffusion that is confirmed by the change of temperature range of bainite transformation (Figure 4).

Lowering of bainite transformation temperature is accompanied by inhibition of carbon diffusion that causes carbide precipitation in the ferrite grain body, and by development of lower bainite structure in the weld metal (Figure 5) by deceleration of the processes

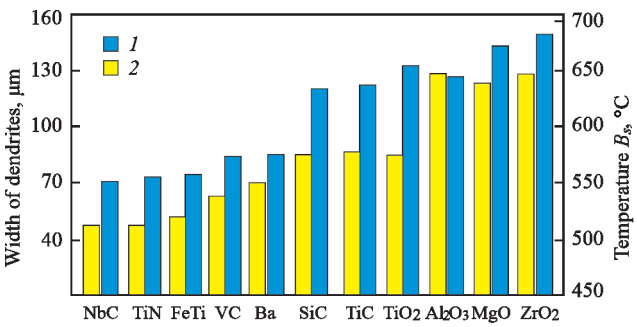

Figure 4. Influence of inoculation of refractory compounds on the change of dendrite size (*1*) and temperature of the start of bainite transformation B_s (*2*)

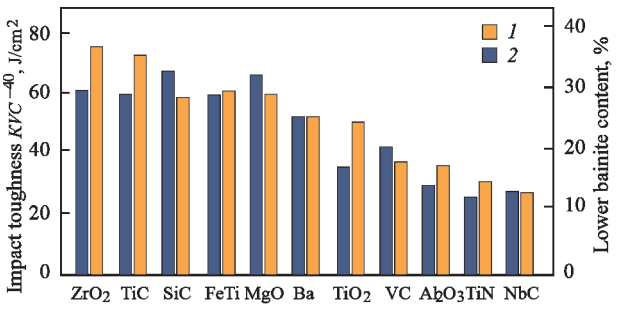

Figure 5. Influence of inoculation by refractory compounds on lower bainite content in the microstructure (*1*) and weld metal impact toughness (*2*)

of upper bainite and Widmanstatten ferrite formation. Change of microstructural composition results in improvement of weld metal toughness values (Figure 5).

Experimental results given in work [18] confirm the possibility of inoculant influence on weld metal structure. It is found that addition of dispersed particles of refractory compounds with the respective physico-chemical properties to the weld pool allows changing the primary structure grain size, and promotes shifting of bainite transformations to lower temperature region. Increase of lower bainite content in the weld microstructure, owing to upper bainite and Widmanstatten ferrite, as a result of development of such processes, allows improvement of their mechanical properties.

CONCLUSION

Formation of weld metal microstructure takes place during a continuous process, which starts from initiation and development of primary structure and ends by formation of a secondary microstructure. Primary structure grain size depends on the energy of interfaces between δ- and γ-phases, and it is determined by the effectiveness of carbon diffusion during γ→α transformation. Inoculation of refractory compounds to the weld pool liquid metal enables influencing the processes of primary structure formation, temperature range of bainite transformation and formation of a secondary microstructure with higher content of lower bainite in the metal of HSLA steel welds.

REFERENCES

1. Lee, S.J., Lee, Y.K. (2008) Prediction of austenite grain growth during austenitization of low alloy steels. *Mater. Des.*, 29(**9**), 1840–1844.
2. Lambert-Perlade, A., Gourgues, A.F., Pineau, A. (2004) Austenite to bainite phase transformation in the heat-affected zone of a high strength low alloy steel. *Acta Mater.*, 52(**8**), 2337–2348.
3. Matsuzaki, Bhadeshia H.K.D.H. (1999) Effect of austenite grain size and bainite morphology on overall kinetics of bainite transformation in steels. *Mater. Sci. Technol.*, 15(**5**), 518–522.
4. North, T. H., Mao, X., Nakagawa, H. (1990) The metallurgy, welding and qualification of microalloyed (HSLA) steel weldments. *Inter. Conf., American Welding Society.* Eds J.T. Hickey, D.G. Howden and M.D. Randall, 219–248.
5. Davies, G.J., Garland, J.G. (1975) Solidification structures and properties of fusion welds. *Int. Metallurgical Rev.*, **20**, 83–10.
6. Babu, S.S., Bhadeshia, H.K.D.H., Svensson, L.-E. (1991) Crystallographic texture and the austenite grain structure of low-alloy steel weld deposit. *J. of Materials Science Letters*, **10**, 142–144.
7. Yin, H., Emi, T., Shibata, H. (1999) Morphological instability of δ-ferrite/γ-austenite interphase boundary in low carbon steels. *Acta Mater.*, **47**, 1523.
8. Griesser, S., Bernhard, C., Dippenaar, R. (2014) Effect of nucleation undercooling on the kinetics and mechanism of the peritectic phase transition in steel. *Acta Mater.*, **81**, 111–20.
9. Griesser, S., Bernhard, C., Dippenaar, R. (2014) Mechanism of the peritectic phase transition. *ISIJ Int.*, **54**, 466–73.
10. Fukumoto,, S., Kurz, W. (1998) Prediction of the δ- to γ-transformation in austenitic stainless steels during laser treatment. *ISIJ Int.*, 38, **1**, 71–77.
11. Stefanescu, M. (2006) Microstructure evolution during the solidification of steel. *ISIJ Int.*, 46(**6**), 786–794.
12. Cuixin, Chen, Haitao, Xue, Huifen, Peng et al. (2014) Inclusions and microstructure of steel weld deposits with nano-size titanium oxide addition. *J. of Nanomaterials*, Article ID 138750, 7.
13. *Hideaki* Suito, Hiroki Ohta, Shuhei Morioka (2006) Refinement of solidification microstructure and austenite grain by fine inclusion particles. *ISIJ Inter.*, 46(**6**), 840–846.
14. Furukawa, T., Saito, N., Nakashima, K. (2021) Evalution of interfacial energy between molten Fe and Fe–18 % Cr–9 % Ni alloy and non-metallic inclustion-type oxides. *ISIJ Inter.*, 61(**9**), 2381–2390.
15. Bhadeshia, H.K.D.H., Svensson, L.E. (1993) Modelling the evolution of microstructure in steel weld metal. *Mathematical Modelling of Weld Phenomena*. Eds by H. Cerjak, K.E. Easterling. Institute of Materials, London, 109–182.
16. Isobe, K. (2010) Effect of Mg addition on solidification structure of low carbon steel. *ISIJ Inter.*, 50(**12**), 1972–1980.
17. Xuan, Ch., Shibata, H., Sukenaga, S. et al. (2015) Wettability of Al_2O_3, MgO and Ti_2O_3 by liquid iron and steel. *ISIJ Inter.*, 55(**9**), 1882–1890.
18. Holovko, V.V., Yermolenko, D.Y., Stepanuk, S.N. et al. (2020) Influence of introduction of refractory particles into welding pool on structure and properties of weld metal. *The Paton Welding J.*, **8**, 9–15.

ORCID

V.V. Holovko: 0000-0002-2117-0864

CORRESPONDING AUTHOR

V.V. Holovko
E.O. Paton Electric Welding Institute of the NASU
11 Kazymyr Malevych Str., 03150, Kyiv, Ukraine.
E-mail: v_golovko@ukr.net

SUGGESTED CITATION

V.V. Holovko (2022) Influence of inoculants on the features of weld structure formation in low-alloyed steels (Review). *The Paton Welding J.*, **9**, 11–14.

JOURNAL HOME PAGE

https://pwj.com.ua/en

Received: 28.06.2022
Accepted: 11.11.2022

DOI: https://doi.org/10.37434/tpwj2022.09.03

INFLUENCE OF PARAMETERS OF MAGNETRON SPUTTERING PROCESS ON PHASE COMPOSITION AND STRUCTURE OF CARBON NITRIDE COATINGS

Yu.S. Borysov[1], O.V. Volos[1], N.V. Vihilianska[1], V.G. Zadoya[1], V.V. Strelchuk[2]

[1]E.O. Paton Electric Welding Institute of the NASU
11 Kazymyr Malevych Str., 03150, Kyiv, Ukraine
[2]V.E. Lashkaryov Institute of Semiconductor Physics of the NAS of Ukraine
45 Nauki Prosp., 02000, Kyiv, Ukraine

ABSTRACT

Deposition of CN_x-coatings was carried out using two magnetron devices with titanium and graphite targets in the mixture of Ar/N_2 gases. The influence of gas mixture (Ar/N_2) composition, pressure (0.35, 1 and 2 Pa) and temperature (100–200 °C) on the structure of the CN_x coating were investigated. It was found that the structure of the coating represents an amorphous disordered graphite-like structure with sp^3-, sp^2- and sp^1 electron bonds of carbon. The most ordered structure is observed in the CN_x coatings (the least ID/IG = 1.16 and 1.2), produced at a pressure of 0.35 Pa, the temperature of the specimen is 130 °C, the content of nitrogen is 40 and 58 %. The influence of a titanium sublayer and a transition TiCN layer on adhesive properties of the CN_x coating was studied. When a titanium sublayer and a transition TiCN layer are used together, the adhesion of the coating to the bases of titanium and Khl8N10T steel grows at a thickness of the coating being 2–3 μm.

KEYWORDS: magnetron sputtering, CN_x coating, structure, phase composition, Raman spectroscopy

INTRODUCTION

Over the last decade, the carbon nitride CN_x coating has attracted a considerable attention [1]. In 1989, Liu and Cohen theoretically calculated a new superhard structure, carbon nitride C_3N_4 [2]. By then, numerous efforts were aimed at the synthesis of this new material. Carbon nitride amorphous film was one of the results of such studies. It was found that it has higher hardness and wear resistance [3] as compared to the film made of a diamond-like carbon. Amorphous coatings have already found a widespread use as protective coatings on hard drives and read-write heads [4] due to their excellent properties. As compared to hydrogenated diamond-like carbon coatings, CN_x has a higher wear resistance at a low friction coefficient [5]. Another advantage of nitrogen incorporation in the coating is an increase in surface energy, which in turn provides a high wettability [6].

CN_x films are mainly composed of carbon and nitrogen, and also can be alloyed with hydrogen. Since these elements are widespread in a living body, the coatings have the properties of biocompatibility [7].

CN_x coatings can be synthesized by such methods as plasma chemical deposition from acetylene with nitrogen gas mixture; vacuum-arc spraying in nitrogen medium from carbon plasma flows generated by cathode spots of vacuum-arc discharges [8]. The use of reactive magnetron sputtering of a graphite target in the mixture of Ar/N_2 gases for this purpose is also interesting [9]. Under certain conditions of deposition, the magnetron CN_x coating can be of great importance of a normalized H/E hardness (more than 0.12), which determines its elasticity and wear resistance under friction conditions (in tribotechnical contact) [10]. In [11] it is proposed to evaluate the elastic properties of the CN_x coating during indenting by the percentage of elastic recovery $R(\%) = (h_{max}–h_{res})/h_{max}\cdot 100$, where h_{max} is the depth of introducing indenter in the coating at a maximum load; h_{res} is the depth after relieving the load. Due to elastic properties, the CN_x coating was called a “superhard rubber”. In [12], the results of studying mechanical and tribotechnical properties of the CN_x coating, deposited on titanium bases, which confirm its high resistance to plastic deformation, are presented. Thus, while depositing the CN_x coating to titanium, elastic surface recovery (R, %) increases from 30 to 81 %.

Wear resistance and adhesive strength of the CN_x coating depends on the effect of ion bombardment conditions [13]. In [14], the technology of producing the CN_x coating with a high adhesion to the surface of the bases of stainless steel with the use of a chromium sublayer is considered. To deposit chromium, the method of high-power impulsed magnetron sputtering (HIPIMS) was used. A distinctive feature of HIPIMS is a high level of ionization of a sprayed material and a high level of dissociation of gas molecules.

The magnetron power with a chrome target was carried out from the pulsed voltage source: U = 500–= 1000 V, f = 150 Hz, t_p = 100 ms, the displacement voltage source had the following parameters: U_d = = 500–1000 V, f = 150 Hz , t_p = 100 ms. The CN_x coating was deposited by spraying the graphite target at DC at a negative displacement voltage U_d = –25 V. Determination of adhesive strength of the CN_x coating by scratching method showed that as compared to the variant when a chromium sublayer was deposited while powering the magnetron from the direct voltage source, the critical load of destruction of the CN_x coating more than 3 times increased.

In [13], it is noted that ion bombardment of amorphous CN_x films improves their mechanical properties, providing high hardness, high resistance to plastic deformation and high elastic recovery.

The aim of the work was the study of a reactive magnetron discharge with a graphite target in the mixture of Ar/N_2 gases, as well as the study and development of the process of producing the CN_x magnetron coating on stainless steel and titanium bases.

PROCEDURE OF EXPERIMENTS AND STUDIES

The coating was deposited using a modernized VU-1BS vacuum unit equipped with a DC magnetron sputtering module consisting of two magnetrons: magnetron 1 with a disc target (88 mm diameter, 4 mm thickness) made of MPG-7 graphite with a purity of 99.98 % and the magnetron 2 with a rectangular target (90×58×4 mm) made of VT1-0 titanium (Figure 1). The magnetrons are mounted on a one flange in such a way that the angle between the surfaces of the targets is equal to 150 °C. As a result, it was possible to simultaneously or alternately deposit coatings on a stationary base from two magnetrons with the same distance between the base and the targets, equal to 110 mm. The magnetron 2 was designed for the deposition of an adhesive sublayer of titanium on metal bases.

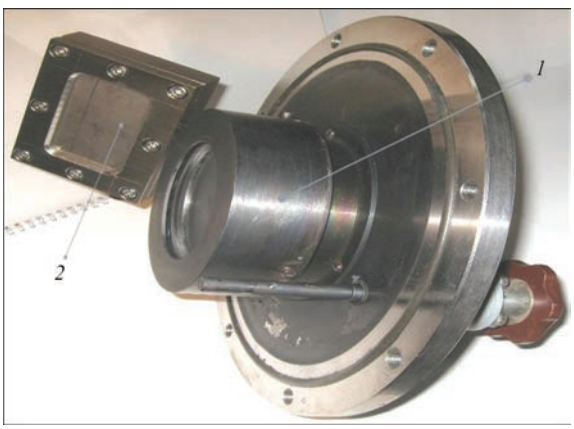

Figure 1. Magnetron sputtering module: *1*, *2* — magnetron 1 and magnetron *2*, respectively

The study of the characteristics of a reactive magnetron discharge with a graphite target was carried out at different values of the working pressure p, the mixture of Ar/N_2 gases, and the percentage of nitrogen in it.

For the initial experiments on studies of the process of the CN_x coating formation, glass bases (65×30×4 mm) were used. This choice was predetermined by the possibility of accurate measurement of the coating thickness using a profilograph-profilometer.

To study the process of forming the CN_x coating on metal materials, as a base, the specimens of Kh18N10T steel and VT1-0 titanium with a size of 65×30×0.5 mm, as well as the specimens of VT1-0 titanium with a diameter of 25 mm and a thickness of 5 mm were used. Before placing in the vacuum chamber, the specimens were cleaned in an ultrasonic bath, which is gradually filled with acetone and ethyl alcohol. In a vacuum at a pressure of $5.0 \cdot 10^{-4}$ Pa, the specimen was heated at a temperature of 150 °C for 20 min, then without turning off the heater, the surface of the specimen was cleaned by bombardment with argon ions (especially pure) in a direct current discharge at a pressure of 1.3 Pa, at a voltage of 1100 V for 20 min.

The specified variants of the specimens treatment were one of the components of the process of increasing the adhesion of the CN_x coating to the base surface. The conducted preliminary experiments showed that in order to increase the adhesive strength of the CN_x coating on the specified bases, it is necessary to deposit an adhesive layer of titanium and an intermediate Ti–C–N layer on their surface. The latter was intended for smoothing the transition interface between materials with different physical characteristics of the base CN_x and adhesive layers of titanium.

Three stages of the process of forming the CN_x coating layers on the surface of Kh18N10T and VT1-0 titanium specimens were determined, as well as the ranges of changing deposition parameters of the layers:

- deposition of a titanium sublayer (δ = 0.3 μm) in argon at an operating pressure p = 0.35 Pa, specific power of a magnetron discharge with a titanium target Δ_{PTi} = 3.5 W/cm, deposition rate V_{Ti} = 25 nm/min and a change in the negative displacement on the base of U_d from –300 to –1400 V;
- deposition of the intermediate Ti–C–N layer (δ = = 0.25 μm) using joint reactive magnetron sputtering of graphite and titanium targets on a direct current in the mixture of Ar/N_2 gases at pressures of p = 0.35, 1 and 2 Pa, average values of Δ_{PC} = 10.4 W/cm and Δ_{PTi} = 3.4 W/cm, $U_{d\,CN_x}$ = 0– –40 V;

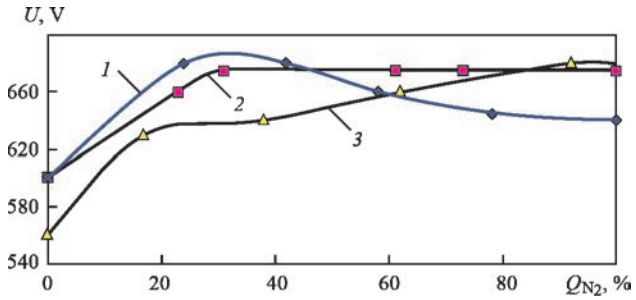

Figure 2. Dependence of the magnetron discharge voltage with a graphite target of MPG-7 on the content of nitrogen in the mixture of Ar/N_2 at I = 1 A, p = 0.35 (*1*), 1 (*2*), 2 (*3*) Pa

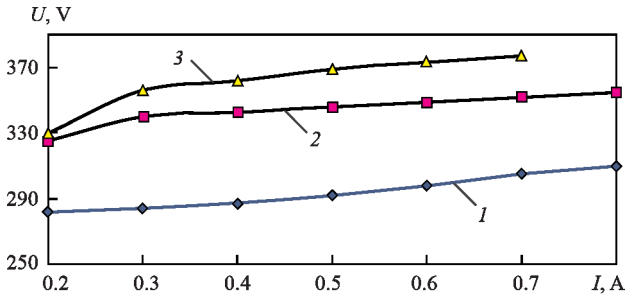

Figure 3. VACh of a magnetron discharge with a titanium target in the mixture of Ar/N_2 gases at p = 0.35 PA: *1* — N_2 = 0; *2* — 25.6; *3* — 45 %

● deposition of the base CN_x layer (δ = 2.0–3.9 μm) in the mixture of Ar/N_2 gases at p = 0.35, 1 and 2 Pa, Δ_{PC} = 10 W/cm, $U_{d\ CN_x}$ = 0– –40 V, T_b = 130, 200, 350 °C.

The phase analysis of the coatings was carried out by the X-ray diffraction method using an X-ray diffractometer Philips X'Pert-MPD with a CuK_α X-ray source (wavelength λ = 0.15418 nm). X-ray diffraction spectra were taken in the Bragg–Brentano geometry (2Th-omega-scanning) — the full angular range of diffraction spectrum registration by 2θ = 25–75°.

The combining Raman spectroscopy method (CRS) was used to determine the configurations of carbon chemical bonds in the coating. The micro Raman spectra were measured in the reflection geometry at a room temperature using a triple Raman spectrometer T-64000 Horiba Jobin-Yvon equipped with a cooling CCD detector. For excitation, an Ar–Kr laser line with a wavelength of 488 nm was used. The radiation was focused on the specimen using a 50× objective, the power of the radiation falling on the specimen was about 0.25 mW.

RESULTS OF EXPERIMENTS AND THEIR DISCUSSION

In order to determine the optimal conditions for deposition of the CN_x coating, the characteristics of a DC magnetron discharge with a graphite target from MPG-7 in the mixture of Ar/N_2 gases were investigated. The experiments were carried out at p = 0.35, 1 and 2 Pa. It was found that at the indicated pressures the discharge is stable and breakdowns of a discharge gap at P = 11 W/cm are absent.

The most complete idea of the nature of a magnetron discharge burning with a graphite target in the mixture of Ar/N_2 gases is given by the dependence of the voltage on a percentage content of nitrogen N_2 consumption in the mixture, which is determined by the ratio of nitrogen consumption to the sum of argon and nitrogen consumption — $Q_{N_2}/(Q_{N_2}+Q_{Ar})100$ (Figure 2). At N_2 = 0, with an increase in the pressure to 2 Pa, the discharge voltage decreases from 600 to 560 V. At p = 0.35 Pa with an increase in N_2 to 24 %, the discharge voltage reaches a maximum U = 690 V, and further decreases at N_2 = 100 % U = 640 V. A somewhat different character of the change in the discharge voltage was detected at pressures equal to 1 and 2 Pa. Thus, at p = 1 Pa and N_2 = 24 %, the voltage also reaches a maximum U = 675 V, but does not change further to N_2 = 100 %.

The volt-ampere characteristics (VACh) of a direct current magnetron discharge with a VT1-0 titanium target (magnetron 2) in the mixture of Ar/N_2 gases at p = 0.35, 1, 2 Pa were also studied. The voltage of discharge burning increases with an increase in N_2 due to the formation of a TiN film on the surface of the target (Figure 3).

During a simultaneous operation of two magnetrons, the surface of a titanium target is partially dusted with a carbon film, which also leads to an increase in the voltage of a discharge burning and a sharp increase in the ignition voltage. For p = 0.35, 1, and 2 Pa, the corresponding boundary values of N_2 were determined, equal to 45, 73, and 66 %, at which a stable excitation and maintenance of the discharge with a titanium target was provided.

Figure 4 shows the dependences of the rate of depositing CN_x coating on glass substrates on the nitrogen content in the Ar/N_2 mixture under the following conditions: working pressures p = 0.35, 1 and 2 Pa, discharge current I = 1 A. At each of the specified pressures, the coating was deposited at six values

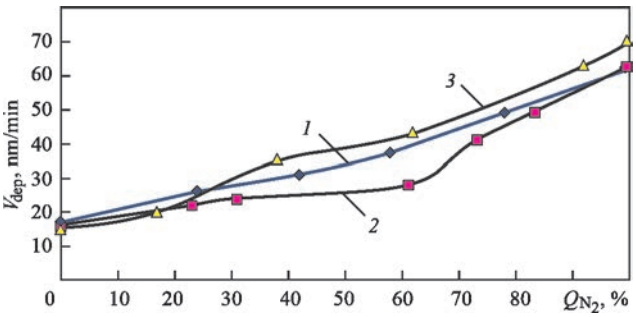

Figure 4. Dependence of the rate of depositing the CN_x coating on the content of nitrogen in the mixture of Ar/N_2 at p = 0.35 (*1*), 1 (*2*), 2 (*3*) Pa

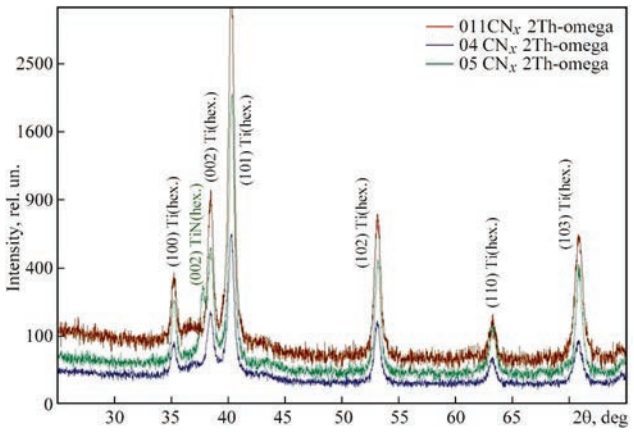

Figure 5. X-ray patterns of specimens 04CN$_x$, 05CN$_x$ and 011CN$_x$ produced in the geometry of Bragg–Brentano

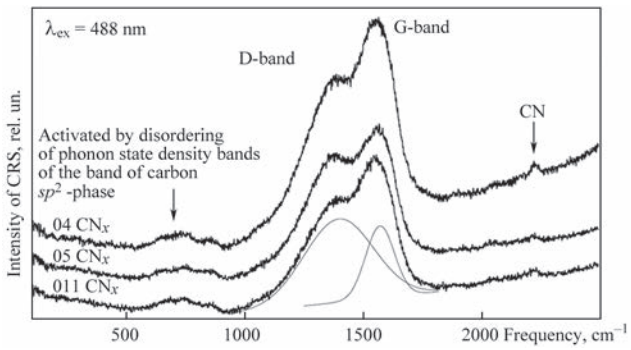

Figure 6. CRS spectra of CN$_x$ coating specimens (in all CRS spectra two D- (≈ 1390 cm^{-1}) and G-bands (≈ 1580 cm^{-1}) are recorded, which are characteristic of inelastic light scattering in carbon structures)

of the N_2 nitrogen content consumption in the Ar/N_2 mixture. At the same time, the specific power of the magnetron discharge P varied within the ranges of 9.3–11.4 W/cm.

As is seen from Figure 4, with an increase in the nitrogen content in the mixture of gases at all pressures, the deposition rate increases. At p = 0.35 and 2 Pa, the growth is uniform. At p = 1 Pa, an increased growth in the deposition rate occurs with an increase in N_2 from 60 to 100 %. At N_2 = 0, in the argon atmosphere, a carbon coating was deposited on the base at a rate V_C = 16 nm/min (0.96 μm/h). At N_2 = 100 %, the CN$_x$ coating was formed with the maximum nitrogen content at an average rate V_{CN_x} = 60 nm/min (3.6 μm/h). Therefore, when N_2 changed from 0 to 100 %, the rate of the coating deposition increased by 3.8 times, and the specific power of the discharge, proportional to which the rate of ion sputtering of materials usually changes, increased by only 1.2 times (from 9.3 to 11.4 W/cm).

A significant difference in the degree of the specific power and deposition rate indicates a more complex mechanism of spraying graphite in the mixture of Ar/N_2 gases. The work [15] states that an increase in the deposition rate is possible with an increase in the spraying coefficient of a graphite target due to a reduced cohesive bonding of carbon atoms during the chemical reaction between nitrogen and carbon atoms. In addition, flying CN radicals can be formed, that are easily sprayed on the target surface.

The results of X-ray structural analysis of the magnetron CN$_x$ coatings are presented in Figures 5, 6. The parameters of the process of depositing CN$_x$ coatings are given in Table 1.

As is seen from Figure 5, on the spectra of X-ray diffraction from all specimens 04CN$_x$, 05CN$_x$ and 011CN$_x$ the presence of the titanium (hexagonal) phase, which corresponds to the presence of the adhesion layer of titanium (δ = 0.35 μm) is seen. In the specimen 05CN$_x$, a TiN phase is also present, which most likely formed due to an increased deposition temperature. No reflexes from the layers of CN$_x$ and Ti–C–N are observed, which indicates their amorphous state.

Table 1. Parameters of the process of depositing magnetron Ti + (Ti–C–N) + CN$_x$ coating (bases — VT1-0 titanium)

Specimen number	p, Pa	T_b, °C	Coating sputtering conditions					
			Ti		Ti–C–N		CN$_x$	
			P_{Ti}, W	U_d, W	N_2,%	P_C/P_{Ti}, rel. un.	N_2,%	P_C, W
03CN$_x$	0.35	200	184	–150	25.6	2.7	58	570
04CN$_x$	0.35	130	184	–150	25.6	2.8	58	560
05CN$_x$	0.35	350	184	–300	25.6	2.8	58	560
06CN$_x$	0.35	130	184	–300	–	–	58	580
011CN$_x$	0.35	130	184	–300	25.6	2.8	42	540
012CN$_x$	0.35	350	180	–300	25.6	2.8	42	540
07CN$_x$	1.0	130	190	–300	22.8	2.85	100	580
08CN$_x$	1.0	350	187	–300	22.8	2.9	100	560
010CN$_x$	1.0	200	180	–300	22.8	3.0	100	560
09CN$_x$	2.0	130	180	–300	66.0	2.75	100	560

Table 2. Frequency positions (ω), full width at half maximum (FWHM), ratio of integral intensities for D- and G-bands (ID/IG)

Specimen number	D-band (sp^2)			G-band (sp^3)			ID/IG
	ω, cm^{-1}	FWHM, cm^{-1}	FWHM, rel. un.	ω, cm^{-1}	FWHM, cm^{-1}	FWHM, rel. un.	
04 CN_x	1400.6	349.4	822	1574.5	140.2	683	1.20
05 CN_x	1393.3	336.1	621	1578.8	135.2	470	1.32
011 CN_x	1396.9	345.3	565	1570.6	142.6	488	1.16

The CRS spectra of the studied specimens are presented in Figure 6.

For modeling G- and D-bands, the Gauss functions with a preliminary subtraction of a modeled base line were used (Figure 6). Table 2 shows the results of the analysis of frequency positions, FWHM and ratios of integral intensity of D- and G-bands, which were performed by the decomposition of CRS spectra on the corresponding components. With regard to nitrogen-containing carbon films, in addition to the fluctuations caused by carbon C = C bonds, the contribution to the oscillatory lines is also made by the fluctuations of C = N bonds with the type of sp^2-configuration of chemical bonds. In the experimental CRS spectra in a general case, it is very difficult to divide these deposits. Changing the position and shape of these oscillatory bands occurs as a result of structural changes, formation of disordering, aromatic rings, microcrystalline graphite, etc. [15].

A weak signal in the area of 600–900 cm^{-1} is associated with an induced disordering of sp^2 structural carbon phase by scattering processes with the participation of phonons with non-zero wave vectors.

A Raman band with a spectral position of about 2220 cm^{-1}, which is observed in the CRS spectra of the CN_x coating is associated with the formation of triple C ≡ N chemical bonds with sp^1-hybridization in the studied structures.

The least value of ID/IG = 1.16 ratio indicates the highest carbon ordering in the structure of the CN_x coating (011CN_x specimen), produced at T_b = 130 °C and N_2 = 42 %.

CONCLUSIONS

1. The process of depositing a nanocomposite carbon nitride CN_x coating (2–3 μm thickness) on the bases of Kh18N10T and VT1-0 titanium with the use of the adhesive layer of titanium and intermediate Ti–C–N layer by the method of combined DC reactive magnetron sputtering of titanium and graphite targets in the mixture of Ar/N_2 gases was developed.

2. The studies of the CN_x coating showed that it has an amorphous disordering graphite-like structure with sp^3, sp^2 and sp^1 electron bonds of carbon. The most ordered structure was obtained in the CN_x coatings (ID/IG = 1.16 and 1.2) at p = 0,35 Pa and T_b = = 130 °C, N_2 = 40 and 58 %.

REFERENCES

1. Hultman, L., Neidhardt, J., Hellgren, N. et al. (2003) Fullerene-like carbon nitride: A resilient coating material. *MRS Bulletin*, 28(**03**), 194–202. DOI: https://doi:10.1557/mrs2003.62
2. Liu, A.Y., Cohen, M.L. (1989) Prediction of new low compressibility. *Solids*. *Science*, 245(**4920**), 841–842. DOI: https://doi:10.1126/science.245.4920.841
3. Liu, D., Ruan, C.F., Zhang, P. et al. (2021) Structural, interface texture and toughness of TiAlN/CN multilayer films. *Materials Characterization*, **178**, 111301. DOI: https://doi:10.1016/j.matchar.2021.111301
4. Vyas, A., Shen, Y., Zhou, Z., Li, K. (2008) Nano-structured CrN/CN_x multilayer films deposited by magnetron sputtering. C*omposites Sci. and Technology*, 68(**14**), 2922–2929. DOI: https://doi:10.1016/j.compscitech.2007.11.002
5. Nishimura, H., Umehara, N., Kousaka, H., Tokoroyama, T. (2016) Clarification of relationship between friction coefficient and transformed layer of CN_x coating by in-situ spectroscopic analysis. *Tribology Inter.*, **93**, 660–665. DOI: https://doi:10.1016/j.triboint.2014.12.015
6. Chen, R., Tu, J.P., Liu, D.G. et al. (2012) Structural and mechanical properties of TaN/a–CN_x multilayer films. *Surface and Coatings Technology*, 206(**8–9**), 2242–2248. DOI: https://doi:10.1016/j.surfcoat.2011.09.072
7. Wang, M., Toihara, T., Sakurai, M. et al. (2014) Surface morphology and tribological properties of DC sputtered nanoscale multilayered TiAlN/CN_x coatings. *Tribology Inter.*, **73**, 36–46. DOI: https://doi:10.1016/j.triboint.2014.01.008
8. Contreras, E., Bolívar, F., Gómez, M.A. (2017) Influence of nitrogen variation on the microstructrual, mechanical and tribological properties of CN_x coatings deposited by dc unbalanced magnetron sputtering. *Surface and Coatings Technology*, **332**, 414–421. DOI: https://doi:10.1016/j.surfcoat.2017.05.095
9. Cui, F.Z., Qing, X.L., Li, D.J., Zhao, J. (2005) Biomedical investigations on CN_x coating. *Surface & Coating Technology*, 200(**1–4**), 1009–1013. DOI: https://doi:10.1016/j.surfcoat.2005.02.157
10. Kovács, G.J., Veres, M., Koós, M., Radnóczi, G. (2008) Raman spectroscopic study of magnetron sputtered carbon–nickel and carbon nitride-nickel composite films: The effect of nickel on the atomic structure of the C/CN_x matrix. *Thin Solid Films*, 516(**21**), 7910–7915. DOI: https://doi:10.1016/j.tsf.2008.04.081
11. Mubumbila, N., Tessier, P.-Y., Angleraud, B., Turban, G. (2002) Effect of nitrogen incorporation in CN_x thin films deposited by RF magnetron sputtering. *Surface and Coatings Technology*, **151–152**, 175–179. doi:10.1016/s0257–8972(01)01569–9
12. Broitman, E., Czigány, Z., Greczynski, G. et al. (2010) Industrial–scale deposition of highly adherent CN_x films on steel substrates. *Surface and Coatings Technology*, 204(21–22), 3349–3357. DOI: https://doi:10.1016/j.surfcoat.2010.03.038
13. Charitidis, C., Patsalas, P., Logothetidis, S. (2005) Effects of energetic species during the growth of nitrogenated amorphous

carbon thin films on their nanomechanical properties. *Thin Solid Films*, 482(**1–2**), 177–182. DOI: https://doi:10.1016/j.tsf.2004.11.167

14. Tétard, F., Djemia, P., Angleraud, B. et al. (2002) Surface and bulk characterizations of CN_x thin films made by r.f. magnetron sputtering. *Surface and Coating Technology*, **151–152**, 184–188. DOI: https://doi:10.1016/s0257–8972(01)01574–2
15. Gradowski, M.V., Ferrari, A.C., Ohr, R. et al. (2003) Resonant Raman characterisation of ultra-thin nano-protective carbon layers for magnetic storage devices. *Surface and Coating Technology*, **174–175**, 246–252. DOI: https://doi:10.1016/s0257–8972(03)00602–9

ORCID
Yu.S. Borysov: 0000-0002-6019-8464,
O.V. Volos: 0000-0002-9073-2840,
N.V. Vihilianska: 0000-0001-8576-2095,
V.G. Zadoya: 0000-0002-1286-985X,
V.V. Strelchuk: 0000-0002-6894-1742

CONFLICT OF INTEREST
The Authors declare no conflict of interest

CORRESPONDING AUTHOR
N.V. Vihilianska
E.O. Paton Electric Welding Institute of the NASU
11 Kazymyr Malevych Str., 03150, Kyiv, Ukraine.
E-mail: pewinataliya@gmail.com

SUGGESTED CITATION
Yu.S. Borysov, O.V. Volos, N.V. Vihilianska, V.G. Zadoya, V.V. Strelchuk (2022) Influence of parameters of magnetron sputtering process on phase composition and structure of carbon nitride coatings. *The Paton Welding J.*, **9**, 15–20.

JOURNAL HOME PAGE
https://pwj.com.ua/en

Received: 04.07.2022
Accepted: 11.11.2022

DOI: https://doi.org/10.37434/tpwj2022.09.04

INFLUENCE OF HEAT TREATMENT OF SPECIMENS FROM Ti6Al4V MANUFACTURED BY THE TECHNOLOGY OF SELECTIVE LASER MELTING ON STRUCTURE AND MECHANICAL PROPERTIES

S.V. Adzhamskyi[1], **G.A. Kononenko**[1,2], **V.R. Podolskyi**[1,2,3]

[1]LLC "Additive Laser Technology of Ukraine"
31 v Str., Serhiy Podolynskyi, 49000, Dnipro, Ukraine
[2]Z.I. Nekrasov Iron and Steel Institute of the NASU
1 Academician Starodubov Sq., 49000, Dnipro, Ukraine
[3]Ukrainian State University of Science and Technologies
4 Gagarina Prosp., 49000 Ukraine, Dnipro, Ukraine

ABSTRACT

Additive manufacturing, in particular, selective laser melting (SLM) is a modern method of manufacturing parts and assemblies of a complex geometry from metal powder, which are difficult or impossible to be reproduced in the states of traditional manufacturing. This technology is featured by residual stresses formed at the stage of manufacturing parts. Since titanium alloys are characterized by low thermal conductivity, the problem of forming residual stresses is of particular relevance for them and heat treatment for their removal is mandatory for products manufactured using SLM technology. Since the structural state of products manufactured by SLM technology differs from that formed with the use of traditional technologies, it is necessary to study the effect of annealing for residual stress removal on mechanical properties and microstructure of Ti6Al4V alloy manufactured by SLM technology. The specimens were studied after annealing with an exposure time of 1–5 h at 800 °C. It was found that as compared to the initial state after manufacturing, the ultimate strength after heat treatment for 1–5 h undergoes a decrease by 20.55– –23.03 % and relative elongation has an increase by 31.33–35.57 %. At the same time, the nature of variation in the values of relative reduction in area is non-uniform: annealing with an exposure of 1 h does not cause significant changes; with an increase in the exposure time to 2, 3, and 4 h, a decrease in this characteristic is observed, respectively, by 9.03; 45.97 and 62.56 % as compared to the initial state; after exposure for 5 h, the value of relative reduction in area undergoes an increase in this characteristic as compared to the values after exposure for 4 h — by ~26.12 %. According to the results of the correlation analysis of the values of mechanical properties and microstructure parameters, it was found that the shape factor of α-phase lamellas has a high ratio with the values of ultimate strength, and the amount of α-phase is most correlated with the values of relative reduction in area at static tension

KEYWORDS: selective laser melting, heat treatment, titanium Ti6Al4V alloy, mechanical properties, microstructure

INTRODUCTION

Technologies of additive manufacturing (AM), also known as 3D-printing, are increasingly used in the recent times, as well as a number of materials and methods that can be used is expanding.

Since manufacturing processes are ever improved and developed, a demand for more rapid and less expensive manufacturing processes provided the development of a number of rapid prototyping (RP) processes. Using additive manufacturing, almost any geometry with variations in size and complexity can be manufactured with a high degree of accuracy (Simchi & Asgharzadeh, 2004). RP technologies allow manufacturing parts with a complex three-dimensional geometry using AM.

By means of the process of selection laser melting (further — SLM-technology), specimens with a complex geometry from metal powder are manufactured, which are impossible or difficult to be made by other traditional methods of manufacturing [1].

One of the advantages of AM is only a small amount of further treatment (polishing, sandblasting, heat treatment) of products, thus expensive processes with the additional cost can be minimized [2]. Due to a significant widespread of AM technologies, the treatment of such materials has become of particular importance in recent years [3].

One of the features of SLM technology, according to a number of authors [1, 4–7], is the formation of defects that have a different nature as compared to the traditional method of manufacturing, and the possibilities of eliminating these defects at the stage of manufacturing process, or at the stage of further treatment. One of the main defects of additive manufacturing is residual stresses [5, 7], which are formed at the stage of manufacturing parts, their value depends on the parameters of the technological process, they can lead to distortion of the geometry (Figure 1, *a*), cracking

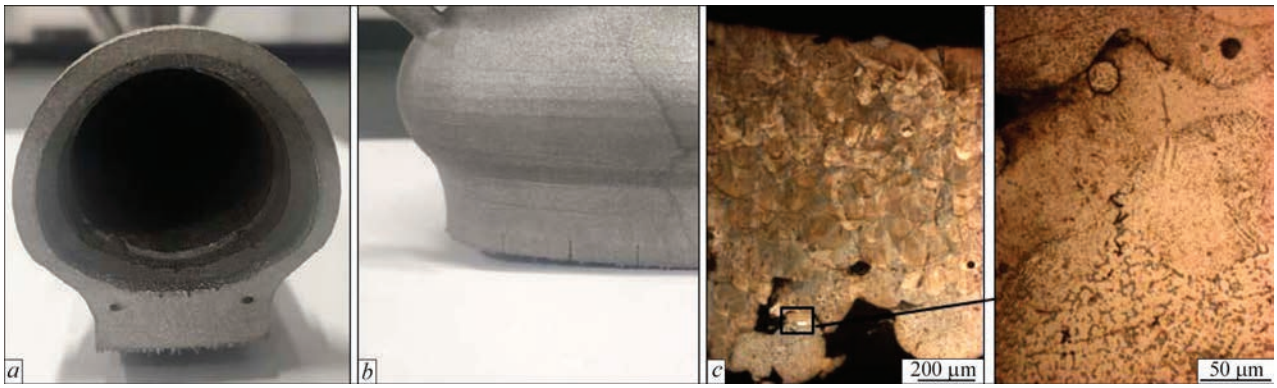

Figure 1. Defects of residual stresses: *a* — distortion of geometry; *b* — cracking; *c* — liquation cracking

of a 3D-product (Figure 1, *b*) and liquation cracking (Figure 1, *c*).

The occurrence of inner residual stresses in parts manufactured using SLM technology is associated with the process of very rapid solidification of the melt pool, several times recrystallization and a local coexistence of hot and cold metal. During cooling in the melt pool, tensile stresses occur as a result of solidification shrinkage and thermal compression during phase transformations in the process of crystallization. Under the action of these stresses, a system of microscopic compressive stresses can be formed, which can lead to cracking. As inner residual stress concentrators, also splashes of liquid alloy on the substrate in the process of powder scanning may be. As far as they have a lower temperature, as a consequence, a large temperature gradient and microcracking arise. Distortion of the geometry during the scanning process and a subsequent application of powder can lead to uneven application of the next layer of powder. Further, this will increase distortions, which provokes an emergency stop of the process of manufacturing parts by using SLM technology, since this technology has a tendency to accumulation of inner residual stresses.

The previous studies [5, 7], aimed at finding the ways of reducing inner stresses, allowed establishing, that the use of rational energy parameters of the powder scanning (beam movement speed and laser power) and a certain building strategy allow reducing deformations under the action of residual stresses without the loss of a product density.

Ti6Al4V alloy has been widely used in manufacturing products of different purpose, including those using AM due to the optimal combination of technological and mechanical properties. However, titanium alloys are characterized by low thermal conductivity, which makes the problem of residual stress formation even more relevant, and the heat treatment for their removal is mandatory for products manufactured using SLM technology. However, it should be noted that the structural state of products manufactured using SLM technology is different from the one that is formed using traditional technologies. Therefore, it is necessary to conduct studies of the impact of annealing for relief of residual stresses on mechanical properties and microstructure of Ti6Al4V alloy, manufactured using SLM technology.

The heat treatment of titanium alloys mostly includes only annealing for relief of residual stresses at 800 °C, which is carried out in an inert atmosphere to prevent surface oxidation. This work will determine the impact of different exposure time during heat treatment of experimental specimens of Ti6Al4V alloy on the mechanical properties during tensile tests.

The aim of the work is the determination and comparing of mechanical properties of tensile test specimens before and after the heat treatment at different exposure time.

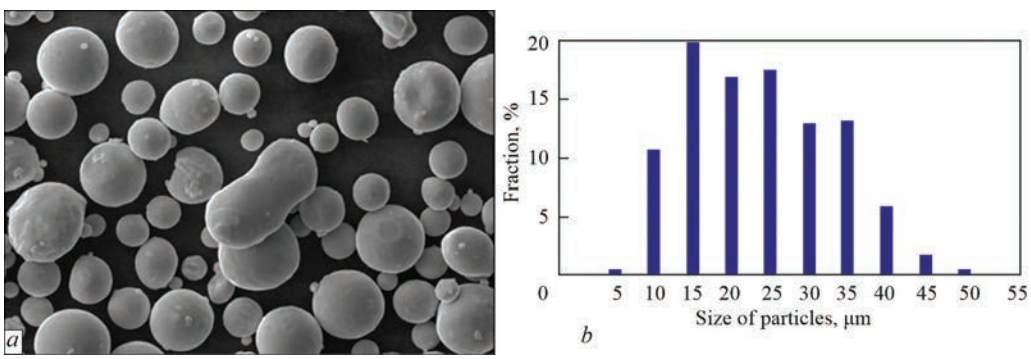

Figure 2. Particles of the initial material of Ti6Al4V at the magnification of 500 (*a*) and the results of granulometric analysis (*b*)

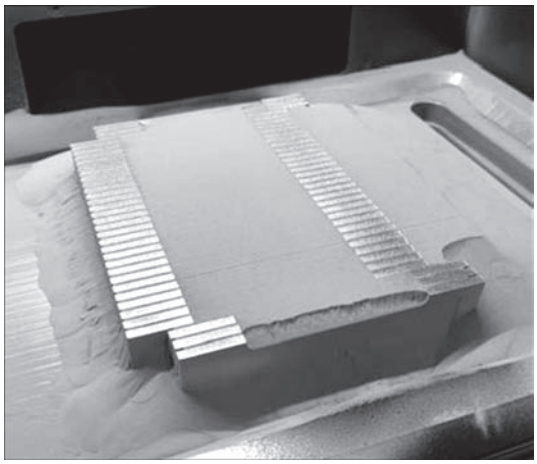

Figure 3. General view of manufactured experimental specimens

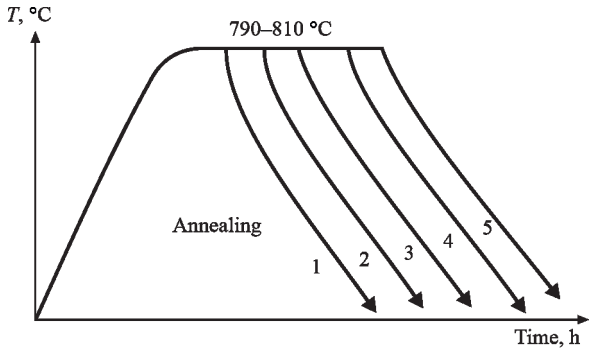

Figure 4. Scheme of heat treatment of experimental specimens

MATERIAL AND RESEARCH PROCEDURE

The studies were conducted on the specimens, manufactured of powder material using SLM technology. The printing of the specimens was conducted in the 3D printer Alfa-280 of the "ALT Ukraina" LLC [5, 6]. The material used in this study was titanium Ti6Al4V alloy with the size of particles from 5 to 40 μm. The chemical composition of Ti6Al4V powder in wt.% is the following: 6.21 Al; 4.03 V; 0.04 Fe; 0.1 C; 0.02 N; Ti is the base.

The initial material was investigated by means of the scanning electron microscope REM-106 (Figure 2, *a*) for determination of shape and sizes of particles. Figure 2, *b* shows the results of the analysis.

The experimental specimens for tensile tests were manufactured according to GOST 1497 — proportional flat specimens with the heads of type I of 3 mm thickness (Figure 3). The heat treatment was carried out at a temperature of 800 °C with an exposure of 1–5 h with a step of 1 h, the scheme of heat treatment is presented in Figure 4. Mechanical treatment of the specimens until reaching net sizes was performed using the lathe HAAS YT4.

The heat treatment was carried out in the ShMP-27 shaft type furnace with the use of a protective environment (argon). The mechanical properties were determined during the tensile test by a standard procedure on the PHYWE machine. Metallographic sections were made according to standard procedures using diamond pastes. Microstructure examinations were performed with the use of Axiovert 200M optical microscope.

The statistical analysis was performed using a standard Excel package of data analysis.

EXPERIMENTAL RESULTS

According to the results of the analysis (Table 1), it was found that the values of mechanical properties after annealing are changed as compared to initial state after manufacturing. The comparative analysis of the values of ultimate strength of all experimental specimens after annealing at a temperature of 800 °C and with the range of 1–5 h exposures with a step of 1 h (specimens Nos 1–5) allows establishing a stable reduction in values by (–20.55– –23.03 %) with a slight discrepancy of ~2.5 % as compared to the initial state (specimen No. 6). Relative elongation after anneal-

Table 1. Mechanical properties of experimental specimens manufactured of titanium Ti6Al4V alloy using selective laser melting technology after heat treatment and in the initial state

Number	State	Ultimate strength, MPa	Δσ, %	Relative elongation, %	Δδ, %	Relative reduction in area, %	Δψ, %
1	Annealing at 800 °C, 1 h exposure	1003.73	–21.64	23.16	34.71	10.32	2.48
2	Annealing at 800 °C, 2 h exposure	989.987	–22.71	23.42	35.43	9.16	–9.03
3	Annealing at 800 °C, 3 h exposure	1017.65	–20.55	22.18	31.83	5.44	–45.97
4	Annealing at 800 °C, 4 h exposure	1008.47	-21.27	23.47	35.57	3.77	–62.56
5	Annealing at 800 °C, 5 h exposure	985.937	–23.03	22.02	31.33	6.4	–36.44
6	Initial state after manufacturing	1281	–	15.12	–	10.07	–

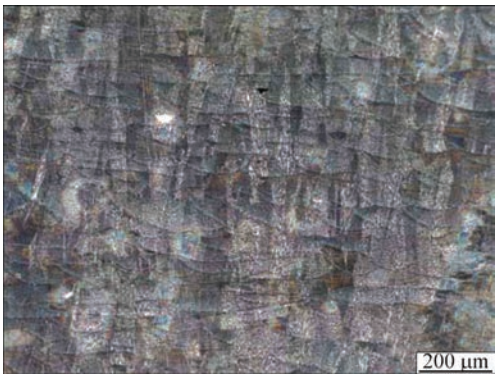

Figure 5. Structure of experimental specimen No. 6 (initial state after manufacturing)

ing undergoes stable changes (31.33–35.57 %) with a slight discrepancy of about 4 % as compared to the initial state. When analyzing changes in relative reduction in area, it was found, that annealing at 800 °C at 1 h exposure does not cause significant changes and with an increase in exposure time to 2, 3 and 4 h, a decrease in this characteristic by 9.03; 45.97; 62.56 % as compared to the initial state is observed. After 5 h exposure, the values of relative reduction in area undergo an increment of this characteristic as compared to the values after 4 h exposure by ~26.12 %, which may indicate changes in the microstructure of Ti6Al4V alloy.

As a result of the analysis of the values of mechanical properties, it was found that ultimate strength after heat treatment is reduced on average by ~21.84 % as compared to the initial state after manufacturing and relative elongation is increased by ~33.7 %.

The studies of experimental specimens in a polished state have shown that they all have a density of about 99.97 %, in most cases among defects there are separate globular pores with a diameter of 3–7 μm. During the microstructure examination, it was found that the experimental specimen No. 6 in the state after manufacturing has a scaly structure typical for the 3D process, which is formed as a result of solidification of individual melt pools. The microstructure was formed by α- and β-phases with columnar elongated grains, which grow crossing several layers (Figure 5).

According to the results of the microstructure examinations (Figures 6–11) of the heat-treated experimental specimens, it was found that the titanium alloy has α+β-structure. After exposure during 1 h (experimental specimen No. 1), a number of α-phase was 34.06 % (Figure 6), the ratio of the sides (width, length) of the α-phase lamella corresponded to ~ 0.5 (Figure 11).

While studying the ratio of the sides of the α-phase of the experimental specimens Nos 2–4, it was found that the α-phase has approximately the same geometric parameters and their ratio is in the range of 0.48–0.50, and its amount was 29.7, 31.11 and 30.87 % respectively (Figures 7–9, 11). The experimental specimen No. 5 has a structure α+β, while studying the α-phase, the ratio of the sides is 0.46, the percentage of which

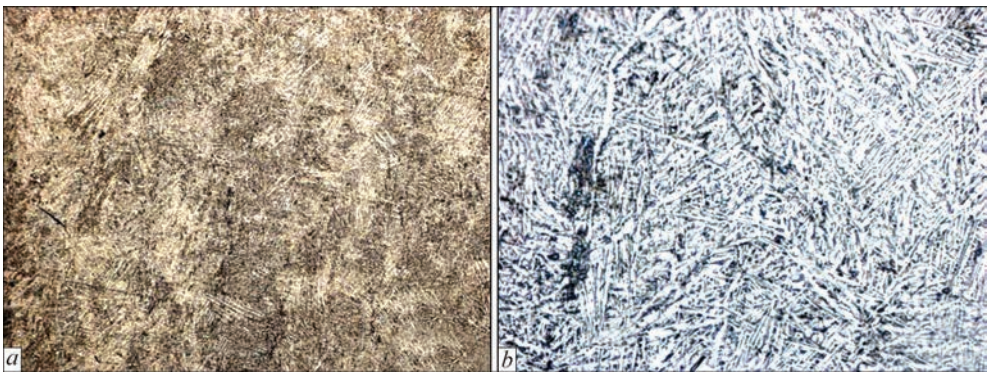

Figure 6. Structure of experimental specimen No. 1 after annealing at 800 °C with 1 h exposure: *a* — ×100; *b* — ×800

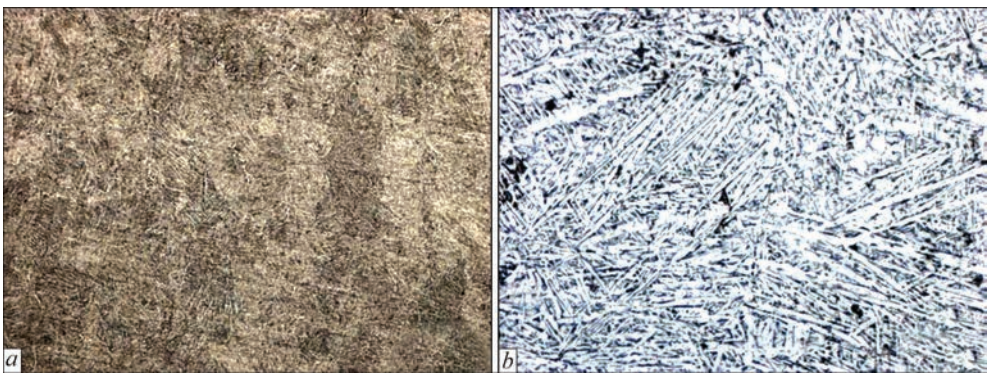

Figure 7. Structure of experimental specimen No. 2 after annealing at 800 °C with 2 h exposure: *a* — ×100; *b* — ×800

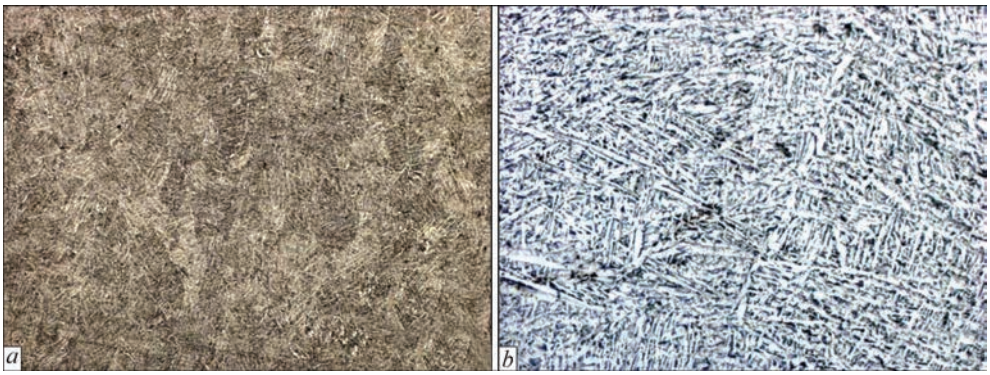

Figure 8. Structure of experimental specimen No. 3 after annealing at 800 °C with 3 h exposure: *a* — ×100; *b* — ×800

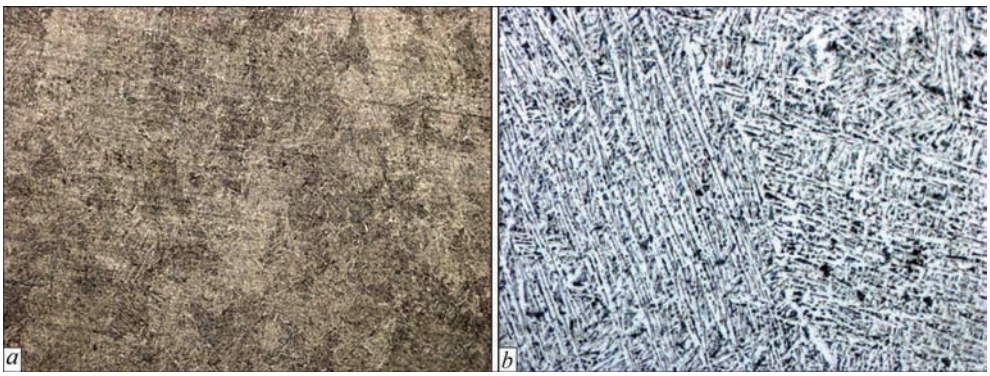

Figure 9. Structure of experimental specimen No. 4 after annealing at 800 °C with 4 h exposure: *a* — ×100; *b* — ×800

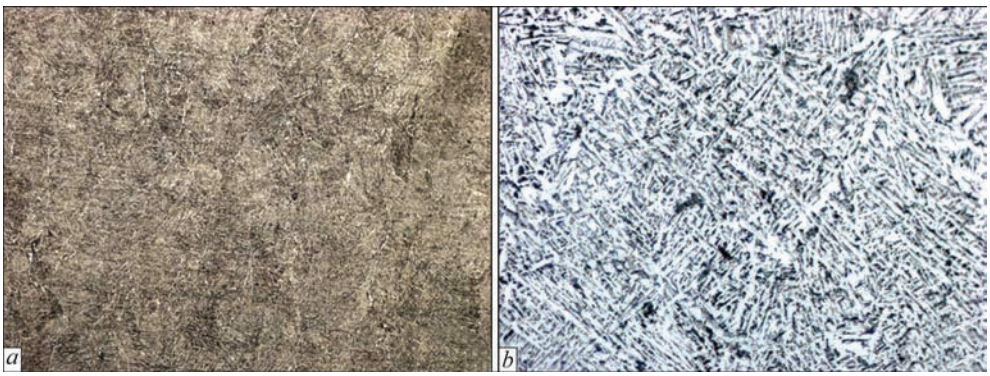

Figure 10. Structure of experimental specimen No. 5 after annealing at 800 °C with 5 h exposure: *a* — ×100; *b* — ×800

was 30.38 % (Figures 10, 11). According to the results of the microstructure examinations, the microstructure represents an α+β-structure with a slight change in the thickness of α-phase lamellas. According to the quantitative evaluation, it was found that the share of α-phase in all experimental specimens amounts to 29.7–34 %. It was found, that heat treatment with slow cooling, which is realized during cooling with a furnace, usually leads to the formation of α+β-lamellar microstructure and a small amount of equiaxial α-phase.

The results of the analysis of a paired correlation of the values of mechanical properties and parameters of the microstructure are presented in Table 2.

This criterion is used to measure the degree of linear dependence between two variables. The value of the coefficient of a paired correlation can vary from –1 to 1. At negative values of coefficient, the influence is negative and at positive values it is positive. At

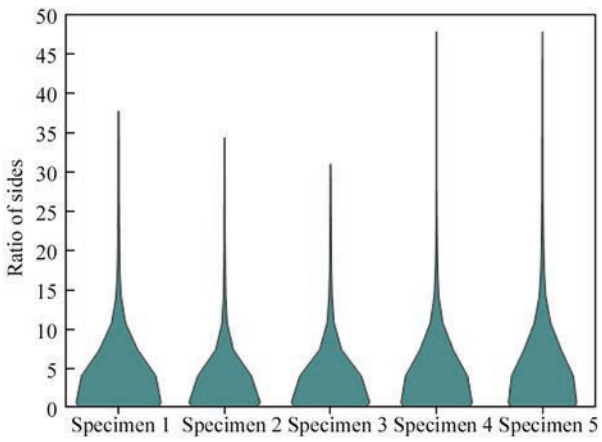

Figure 11. Violin plot of the α-phase size distribution

Table 2. Coefficients of paired correlation of mechanical properties and parameters of the structure after heat treatment of different duration

Parameter	Duration of annealing, h	Relative reduction in area, %	Ultimate strength, MPa	Relative elongation, %	Fraction of α-phase, %	Shape factor of α-phase
Duration of annealing, h	1	–	–	–	–	–
Relative reduction in area, %	–0.77806	1	–	–	–	–
Ultimate strength, MPa	–0.20611	–0.3955	1	–	–	–
Relative elongation, %	–0.50588	0.240275	0.014956	1	–	–
Fraction of α-phase, %	–0.58448	0.441543	0.372066	0.121644	1	–
Shape factor of α-phase	–0.53033	-0.09419	0.88632	0.437112	0.536141	1

values in the range of 1.0–0.5 (–1.0– –0.5), the ratio is considered high, at values of the coefficient in the range of 0.5–0.3 (–0.5– –0.3), the ratio is average, at 0.3–0.1 (–0.3– –0.1), the ratio is low, at lower values, the ratio is absent.

It was found that the ratio of the sides of α-phase precipitations has a high correlation with the values of ultimate strength, and the amount of α-phase is most correlating with the values of relative reduction in area at static tension.

CONCLUSIONS

1. As a result of the analysis of mechanical properties values it was found that ultimate strength after heat treatment of Ti6Al4V alloy, manufactured using the technology of selective laser melting, undergoes a decrease as compared to the initial state after manufacturing using the technology of selective laser melting by ~21.84 % and relative elongation was increased by ~33.7 %.

2. It was established that the heat treatment with slow cooling with the furnace of Ti6Al4V alloy, manufactured using the technology of selective laser melting, leads to the formation of α+β-lamellar microstructure and a small amount of equilibrium α-phase.

3. According to the results of the microstructure examination, it was found that after heat treatment, a change in the thickness of α-phase lamellas occurs, according to the quantitative evaluation it was found that the α-phase after 1–5 h exposure at 800 °C amounts to 29.7–34 %.

4. According to the analysis of results of the values of mechanical properties and parameters of the microstructure, a number and sizes of α-phase lamellas more significantly affects the relative reduction in area than other mechanical properties, shape factor has a close connection with the values of ultimate strength.

REFERENCES

1. Mahoney, M.W. (1989) *Superplatic properties of alloy 718*. Superalloy 718: Metallurgy and Applications. Ed. by E.A. Loria, TMS, 391–405.
2. Conner, B.P., Manogharan, G P., Martof, A.N. et al. (2014) Making sense of 3D printing; creation map of additive manufacturing products and services, *Additive Manufacturing*, **1–4**, 64–74.
3. Frazier, W.E. (2014) Metal additive manufacturing: A review. *J. of Materials Eng. and Performance*, 23(**6**), 1917–1928.
4. Kruth, J.-P., Leu, M.-C., Nakagawa, T. (1998) Progress in additive manufacturing and rapid prototyping. *CIRP Ann.-Manuf. Technol.*, 47(**2**), 525–540.
5. Adjamskyi, S.V., Kononenko, G.A., Podolskyi, R.V. (2021) Influence of SLM-process parameters on formation of boundary region of parts from high-temperature nickel alloy Inconel 718. *Kosmichna Nauka i Tekhnologiya*, 27(**6**), 133, 105–114 [in Ukrainian]. DOI: https://doi.org/10.15407/knit2021.06.105
6. Adjamskyi, S.V., Kononenko, G.A., Podolskyi, R.V. (2020) Influence of technological parameters of SLM-process on porosity of metal products. *The Paton Welding J.*, **10**, 13–18. DOI: https://doi.org/10.37434/tpwj2020.10.03
7. Shifeng, W., Shuai, L., Qingsong, W. et al. (2014) Effect of molten pool boundaries on the mechanical properties of selective laser melting parts. *J. Mater. Process. Technol.*, 214, **11**, 2660–2667.

ORCID

S.V. Adzhamskyi: 0000-0002-6095-8646,
G.A. Kononenko: 0000-0001-7446-4105,
V.R. Podolskyi: 0000-0002-0288-0641

CONFLICT OF INTEREST

The Authors declare no conflict of interest

CORRESPONDING AUTHOR

V.R. Podolskyi
E.O. Paton Electric Welding Institute of the NASU
11 Kazymyr Malevych Str., 03150, Kyiv, Ukraine.
E-mail: rostislavpodolskij@gmail.com

SUGGESTED CITATION

S.V. Adzhamskyi, G.A. Kononenko, V.R. Podolskyi (2022) Influence of heat treatment of specimens from Ti6Al4V manufactured by the technology of selective laser melting on structure and mechanical properties. *The Paton Welding J.*, **9**, 21–26.

JOURNAL HOME PAGE

https://pwj.com.ua/en

Received: 30.06.2022
Accepted: 11.11.2022

DOI: https://doi.org/10.37434/tpwj2022.09.05

CHEMICAL OVERLAP WELDING OF EPOXY VITREMERS AND THEIR NANOCOMPOSITES

A.V. Vashchuk, S.I. Motrunich, V.L. Demchenko, M.V. Iurzhenko, M.O. Kovalchuk, E.P. Mamunya

E.O. Paton Electric Welding Institute of the NASU
11 Kazymyr Malevych Str., 03150, Kyiv, Ukraine

ABSTRACT

In this work, the technology of chemical overlap welding of polymer materials based on epoxy resins (transparent film) and their nanocomposites with oxidized graphene (black film) was developed. The overlap welding of film materials with a thickness of 0.5 mm was carried out under the conditions of isothermal heating of 150 °C and pressure of the limiting plate. The selection of an effective welding mode was performed at different duration of welding: 30 and 60 min. Mechanical tests of the produced welded joints showed their strength at the level of the base material. Features of the structural organization of welded joints of composites were investigated by the method of wide-angle X-ray diffraction. The chemical structure of the material of welded joints was investigated by the Fourier transmission infrared spectroscopy. Modeling of stresses that occur in the specimens of welded joints was calculated using the values of the modulus of elasticity and the coefficient of linear expansion, experimentally found by the method of thermal mechanical analysis.

KEYWORDS: epoxy nanocomposites, oxidized graphene, vitremers, welded joints, chemical welding

INTRODUCTION

Development of shape-memory materials capable of reacting to environmental changes (temperature, power, electromagnetic field, solvent, humidity, etc.) and correcting their mechanical parameters (shape, position, deformation, etc.) for recovery to original state, is an important and relevant direction of development of construction machinery [1], structures deployed in space [2], artificial muscles [3], biomedical devices [4], sensors [5], and energy converters [6]. Solution of this problem is closely related to application of crosslinked polymers that is attributable to their high heat resistance, fixing ability and shape recovery rate. Fabrication of structures with shape-memory effect can be simplified by application of welding.

In the case of diffusion welding of dissimilar materials it is necessary to take into account the features of thermal impact on each of the welded polymer materials. The compatibility of material combinations is determined by the ratio of their coefficients of linear expansion (a_1/a_2). According to literature, the high strength of the joints produced by diffusion welding can be achieved only in such material combinations, for which $a_1/a_2 < 1.2$ [7], that essentially limits the applicability of welding.

Unlike diffusion welding which is due to the forces of intermolecular interaction in the joint zone, chemical welding takes place due to interaction of functional groups on the contacting surfaces with bond formation. Chemical welding of dissimilar materials into one part is rational for building more complex and multifunctional structures. In particular, joining polymer composites with discrete vitrification temperatures is one of the methods of producing thermosensitive shape-memory materials. Thus, the shape of each part is deformed and recovered at certain temperatures, independently one from another [8]. Another strategy of transformation of flat films into 3D-static structures is creation of two layers with further application of external stimuli (photo-, chemical or other treatment) [9, 10]. Active 3D-static structures were recently obtained by chemical welding of liquid-crystal elastomers based on epoxy resins and their composites with polydopamine (PDA) with their further two-directional tension [11]. So, the difference in the response to NIR-radiation (1.0 W/cm^2) led to specific 3D deformation in keeping with the pattern: the composite recovers its initial length, while the transparent film does not react to light and keeps its elongated shape, making the sample bend through 90° (Figure 1, *a*). Similarly, the linear pattern can be controlled by sample bending in the form of a circular arc (Figure 1, *b*), spiral (Figure 1, *c*), and claws (Figure 1, *d*). It should be noted that 2D-dynamic structures are required, which demonstrate automatic reversible change of shape, convenient for transportation and storage.

In this work a technology of chemical welding of transparent polymer films, based on epoxy resins and their composites with oxidized graphene, is proposed, features of structural organization of the produced welded joints were studied, and their mechanical and thermal properties were established.

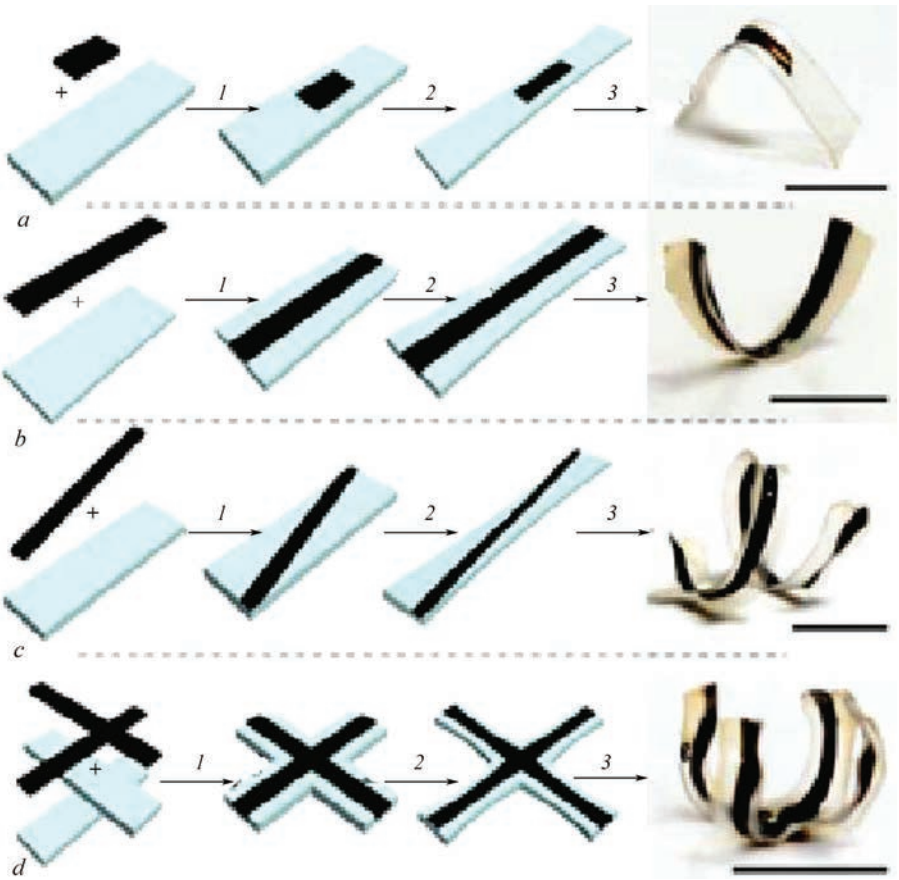

Figure 1. Schematic illustration of producing the welded joints and images of the respective 3D structures: composite film in the center (*a*), in the middle (*b*), diagonally (*c*) and crosswise (*d*)

MATERIALS AND EXPERIMENTAL PROCEDURES

Diglycyl ether of bisphenol A (4.4′-isopropylenediphenol diglycidyl ether, 2.2-bis[4-(glycidyloxy)phenyl]propane, DGEBA) with the following main characteristics: epoxy equivalent mass of 172–176, M = = 340.41 g/mole, ρ = 1.21 g/ml at 25 °C.

Trimethylolpropane tris(3-mercaptopropionate) (T_3M) with the following main characteristics: ≥95.0 %, $T_?$ = 220 °C/0.3 mm. Hg, n_{20D} = 1.518, M = = 398,56 g/mole, ρ = 1.16 g/ml at 25 °C.

Tin 2-ethylhexanoate (II) (tin octoate, tin salt of 2-ethylhexanoic acid, tin (II) 2-ethyhexanoate, $Sn(Oct)_2$) with the following main characteristics: 92.5–100.0 %, n_{20D} = 1.493, M = 405.12 g/mole, ρ = = 1.251 g/ml at 25 °C.

Oxidized graphene (OG). Nanoparticles of oxidized graphene consisted of blocks of 15–20 weakly bonded graphene layers with the following main characteristics: 4–10 % of oxidized edges (epoxy, carbonyl, hydroxyl, phenol groups) ρ = 1.8 g/cm^3. Detailed OG structure is still not understood, because of irregular application of the layers.

Transparent polymer films (polyDGEBA/T_3M)) were obtained by thermal solidification of DGEBA and T_3M at equal molar ratio of thiol and epoxy groups in the presence of 5.0 wt.% $Sn(Oct)_2$. Composite films (poly(DGEBA/T_3M)/OG) were obtained with OG addition to the produced mixture with filling concentration of 1.0 wt.% [12]. Mixture preparation was conducted in BAKU BK-2000 ultrasonic bath at 44 Hz frequency and 50 °C for 30 min. Mixture polymerization was performed under the conditions of step-like isothermal heating: 120, 150 °C/2 h. Thickness of the produced poly(DGEBA/T_3M) and poly(DGEBA/T_3M)/OG films was equal to 0.5 mm.

Testing for static uniaxial tension was conducted in keeping with ISO 527 standard in upgraded tensile testing machine 2054 R-5 fitted with 500N strain gauge. The samples were first cut out in the form of 60 mm long and 25 mm wide strips. Samples of film materials and welded joints were tested with the rate of 2 mm/min and temperature control (25 °C). Young's modulus E for each sample was calculated as the slope of σ–ε deformation curve between 0.25 and 0.5 % ε deformation. Elongation at rupture was determined as strain value at stress lowering to 10 % of the maximum strength value. Stresses at destruction for base material and samples of overlap joints were determined by the following formula:

$$\sigma_{br} = \frac{P_{br}}{S_c},$$

where σ_{br} are the breaking stresses, MPa; P_{br} are the breaking loads, N; S_c is the cross-sectional area in the fracture site, mm^2.

Morphological features of welded joint sections were studied using Versamet-2 microscope in the transmission mode in keeping with DSTU EN12814-5:2018. Recording of the obtained results was performed using a digital photocamera, with which the microscope is fitted.

Features of structural organization of poly(DGEBA/T_3M) and poly(DGEBA/T_3M)/OG films, as well as welded joints on their base were studied by the method of wide-angle radiography in XRD-7000 diffractometer (Shimadzu, Japan), where the X-ray optical scheme is made by the Debye-Scherrer method for passage of the primary beam through the studied sample, using CuK_α-radiation (λ = 1.54 A) and graphite monochromator. Investigations were performed by the method of automatic step-by-step scanning in the mode of 30 kV for 30 mA in the range of scanning angles (2θ) from 3.0 to 55° at exposure time of 5 s. Temperature of conducting the investigations was equal to 20 ± 2 °C. Mean distance between the molecular layers in amorphous polymers (*d*) was determined in keeping with Wulff–Bragg equation:

$$d = n\lambda(2 \sin \theta_m)^{-1},$$

where *n* is the ordinal number of the diffraction maximum (equal to a unity in studies of all the polymer types, as the structure of macromolecular compounds is of a relaxation nature); λ is the wave length of the characteristic X-ray radiation (λ = 1.54 A for CuK_α radiation), θ_m is the angular position of the diffraction maximum on scattering profile.

Chemical structure of the welded joints was studied by Fourier transmission infrared spectroscopy (FTIR), using Tensor 37 spectrometer of Bruker Company in the frequency range of 4000–600 cm^{-1}. For each spectrum 32 sequential scans with the resolution of 4 cm^{-1} were averaged. Intensity of absorption band with the maximum at 1607 cm^{-1}, which corresponds to phenyl group oscillations, was used as the internal standard.

Additional studies of the stressed-strained state of samples of base material (poly(DGEBA/T_3M) and poly(DGEBA/T_3M)/OG) and welded joints, were performed to assess the possible strains and stresses at sample heating. They were conducted using the ANSYS19.1 finite element analysis software. Modelling was performed at heating the samples from 40 to 100 °C. Experimentally established values of the modulus of elasticity and coefficient of linear expansion, obtained by the method of thermal mechanical analysis, were taken as the initial data for SSS calculation. Sample model of 60×10×0.5 mm size was broken down into a simple hexagonal finite-element mesh with element size of 0.25 mm.

EXPERIMENTAL PART AND DISCUSSION

Chemical overlap welding of (poly(DGEBA/T_3M) and poly(DGEBA/T_3M)/OG) was conducted by the thermomechanical method under the conditions of isothermal heating at 150 °C and pressure of the limiting plate, coated by antiadhesive film in MTS651.06E-04 Environmental Chamber (USA). Effective welding mode was selected on the base of the change of welding process duration. Two soaking scenarios were considered: 30 and 60 min. Scheme of overlap welded joint formation is shown in Figure 2, *a*. Energy supply into the joint zone by thermal heating ensured formation of 1.0 mm thick joint. Primary control of the joint quality by visual examination showed absence of defects, namely change of colour, OG pressing outside, as well as traces of burns-through, pores and cavities (Figure 2, *b*). It should be noted that no transition of (poly(DGEBA/T_3M) and poly(DGEBA/T_3M)/OG) into the plastic state took place during welding that is confirmed by the stability of their dimensions and absence of deformations after the joint formation (Figure 2, *b*).

A complex of tests and investigations was conducted for assessment of physico-mechanical properties of the produced (poly(DGEBA/T_3M) and poly(DGEBA/T_3M)/OG) films, as well as their overlap welded joints. It was found that destruction of welded joints produced during 30 min, runs through the weld, at

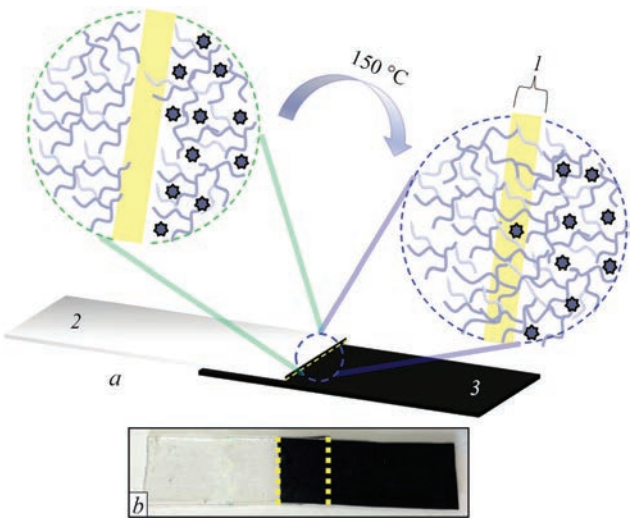

Figure 2. Schematic image of material structure recovery in the weld zone during chemical welding (*a*): *1* — weld zone; *2* — transparent film; *3* — composite; *b* — appearance of the produced overlap welded joint

Strength of the produced films and their welded joints

Sample	Welding mode		σ_{fr}, MPa	Fracture
	T, °C	*t*, min		
Poly(DGEBA/T_3M)	–		18.1–19.9	–
Poly(DGEBA/T_3M)/OG	–		20.1–22.4	–
Welded joint	150	30	8.1–9.5	Weld
		60	12.1–13.5	Poly(DGEBA/T_3M) base material

8.1–9.5 MPa (Table). At the same time, at increase of welding duration to 60 min, welded joints fail through base material (poly(DGEBA/T_3M), beyond the welded joint. It should be noted that in this case welded joint σ_{fr} is on the level of that of (poly(DGEBA/T_3M) base material.

Conducted studies of the macrostructure of experimental welded joints revealed absence of any signs of the interphase (Figure 3). Thus, during chemical welding no formation of an independent continuous phase, which would differ by its properties from those of poly(DGEBA/T_3M) and poly(DGEBA/T_3M)/OG base materials, was observed.

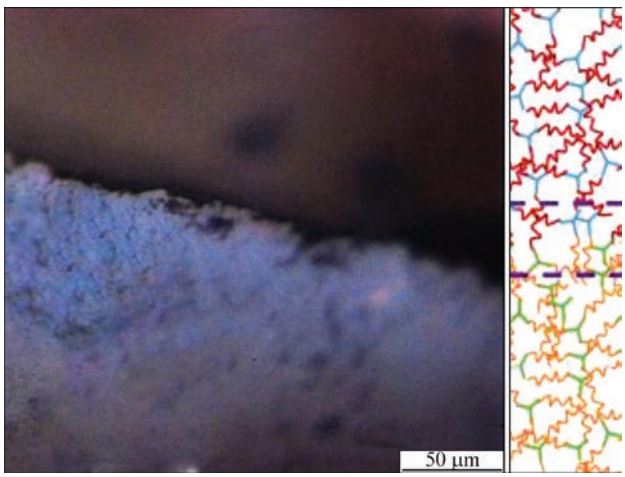

Figure 3. Optical photography of welded joint sections

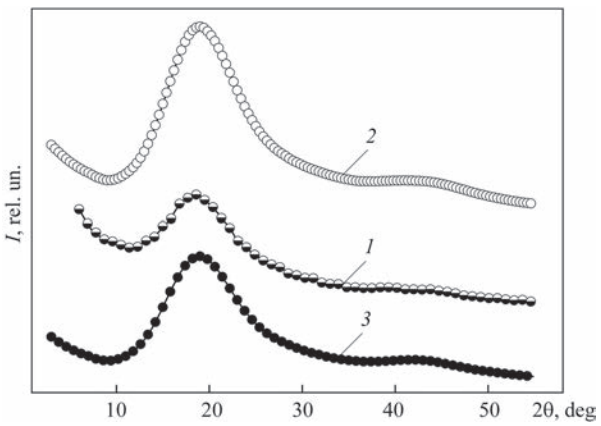

Figure 4. Wide-angle R-ray diffraction patterns of the welded joint: weld zone (*1*); poly(DGEBA/T_3M) (*2*); poly(DGEBA/T_3M)/OG (*3*)

Analysis of wide-angle X-ray diffraction patterns (Figure 4) showed that the welded joint is characterized only by short-range ordering during translation in space of fragments of internodal molecular links. This is evidenced by appearance on the diffraction pattern of one diffraction maximum of the diffuse type (amorphous halo) with $2\theta_m$ angular position close to 18.8°. However, mean distance between the layers of internodal molecular links in the welded joint is equal to 2.5 Å in keeping with Bragg's equation. At the same time, compared to base material of optically transparent (Figure 4, curve *2*) and composite films (Figure 4, curve *3*) no shifting of the diffraction maximum of diffuse type is recorded on the diffraction pattern of weld sample (Figure 4, curve *1*). It is indicative of the fact that the mean distance between the layers of molecular links does not change as a result of weld formation.

As was anticipated, 3441, 1735, 1607, 1509, 1244, 1032, 825 cm^{-1} absorption bands, typical for (poly(DGEBA/T_3M) base material were recorded in FTIR-spectra of the weld zone (Figure 5, curve *1*). Spectra of poly(DGEBA/T_3M) (Figure 5, curve *2*) and poly(DGEBA/T_3M)/OG (Figure 5, curve *3*) were used for comparison. It should be noted that absence of multiplet peaks in the frequency range of 500–400 cm^{-1} (characteristic for poly(DGEBA/T_3M)/OG) in the weld zone spectrum (Figure 5, curve *1*), confirms formation of the weld, which is identical to poly(DGEBA/T_3M) by its chemical structure.

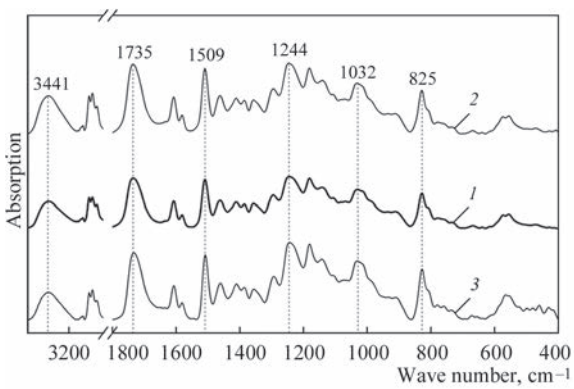

Figure 5. Typical FTIR spectra of the welded joint: weld zone (*1*); poly(DGEBA/T_3M) (*2*); poly(DGEBA/T_3M)/OG (*3*)

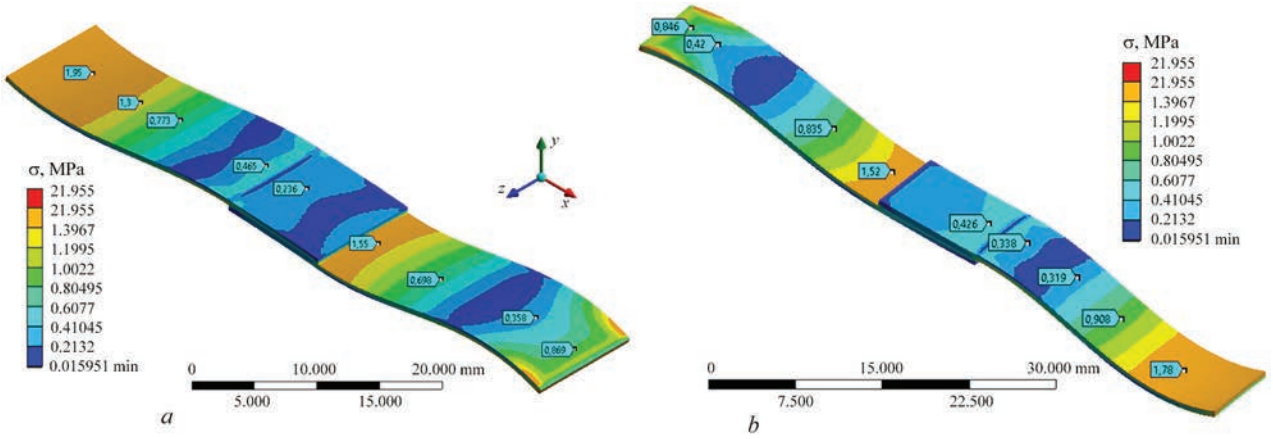

Figure 6. Stresses arising in the sample of overlap welded joint at calculation model I (poly(DGEBA/T_3M left part, poly(DGEBA/T_3M)/OG right part), at its heating from 40 to 100 °C (markers indicate stresses on the surface); *a* — top view; *b* — bottom view

Figures 6, 7 give the results of calculations of stresses arising in samples of overlap welded joints at their heating from 40 up to 100 °C (calculation model I and model II). It is shown that stresses arising in model I (poly(DGEBA/T_3M left part and poly(DGEBA/T_3M)/OG right part) are close to 1.95 MPa and in calculation model II (poly(DGEBA/T_3M left part), middle part with properties established for the weld zone, and poly(DGEBA/T_3M)/OG right part) they are equal to 2.36 MPa, at the same distance from the fixing point.

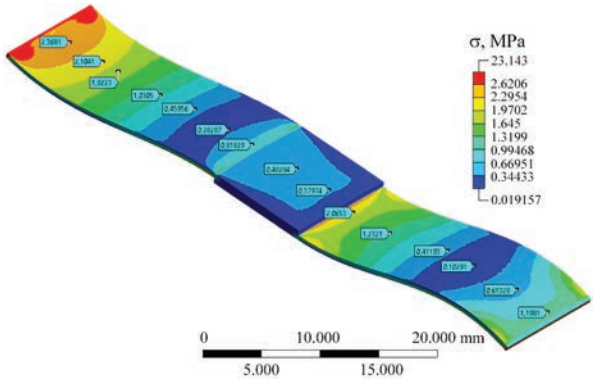

Figure 7. Stresses arising in the sample of overlap welded joint at calculation model II poly(DGEBA/T_3M left part), middle part with properties established for the weld zone, poly(DGEBA/T_3M)/OG right part)) at its heating from 40 up to 100 °C (markers indicate surface stresses)

CONCLUSIONS

Chemical welding of different materials into one part is rational for fabrication of more complex and multifunctional structures. This work gives the results of studies on development of the technology of chemical welding of transparent polymer films based on epoxy resins (transparent film) and their composites, filled with 1.0 wt.% of oxidized graphene (black film). Investigation showed that heating at 150 °C for 60 min is sufficient in general for formation of a sound welded joint. Visual examination of welds showed absence of the change of colour, pressing of oxidized graphene outside, or traces of burns-through, pores and cavities on the welded joint surface that ensures tightness and mechanical characteristics of the welded joint. Investigations of physico-mechanical properties of welded joints, produced at 60 min duration of welding showed that fracture occurs beyond the welded joint from the side of the transparent film material, and the strength limit is on the level of 12.1–13.5 MPa, respectively. Here, the overlap welded joint remains practically undamaged. Microstructural investigation of experimental welded joints showed that the images of the produced weld surface do not reflect formation of independent continuous interphase. FTIR spectral studies enabled establishing a full correlation between the spectra of the weld zone and transparent polymer film. It is found that during weld formation the mean distance between the layers of molecular links does not change that is confirmed by the results of wide-angle roentgenography. Finite element studies of the stress-strain state at higher temperatures in simple welded polymer products, using the obtained coefficients of linear expansion showed that the stresses arising in calculation model I, are close to 1.95 MPa, whereas in calculation model II they are equal to 2.36 MPa at the same distance from the fixing point.

Investigations were performed under the project of the Research Laboratories of Young Scientists of the NAS of Ukraine No. 11/01-2021(2) for conducting investigations in the priority directions of development of science and technology in 2020-2021 (Program No. 6541230).

REFERENCES

1. Zheng, Y. Dong, Y.H. Li (2018) Resilience and life-cycle performance of smart bridges with shape memory alloy (SMA)-cable-based bearings. *Construct. Build. Mater.*, **158**, 389–400.
2. Li, F., Liu, Y.J., Leng, J.S. (2019) Progress of shape memory polymers and their composites in aerospace applications. *Smart Mater. Struct.*, **28**, 103003.

3. Yuan, J.K., Neri, W., Zakri, C. et al. (2019) Shape memory nanocomposite fibers for untethered high-energy microengines. *Science*, **365**, 155–158.
4. Shin, Y.C., Lee, J.B., Kim, D.H. et al. (2019) Development of a shape-memory tube to prevent vascular stenosis. *Advanced Materials*, **31**, 1904476.
5. Li, Z., Qi, X.M., Xu, L. et al. (2020) A self-repairing, large linear working range shape memory carbon nanotubes/ethylene vinyl acetate fiber strain sensor for human movement monitoring. ACS Appl. Mater. *Interfaces*, 37(**12**), 42179–42192.
6. Xu, W., Wong, M.C., Guo, Q.Y. et al. (2019) Healable and shape-memory dual functional polymers for reliable and multipurpose mechanical energy harvesting devices. *J. Mater. Chem.*, **7**, 16267–16276.
7. Volkov, S.S. (2001) *Welding and adhesive bonding of polymer materials*. Moscow, Khimiya [in Russian].
8. Ji, F., Liu, X., Sheng, D., Yang, Y. (2020) Epoxy-vitrimer composites based on exchangeable aromatic disulfide bonds: Reprocessibility, adhesive, multishape memory effect. *Polymer*, **197**, 122514.
9. Na, J.H., Evans, A.A., Bae, J. et al. (2015) Programming reversibly self-folding origami with micropatterned photocrosslinkable polymer trilayers. *Advanced Materials*, **27**, 79–85.
10. Silverberg, J.L., Evans, A.A., McLeod, L. et al. (2014) Using origami design principles to fold reprogrammable mechanical metamaterials. *Science*, **345**, 647–650.
11. Li, Z., Yang, Y., Wang, Z. et al. (2017) Polydopamine nanoparticles doped in liquid crystal elastomers for producing dynamic 3D structures. *J. of Mater. Chem. A*, **5**, 6740–6746.
12. Vashchuk, A.V., Motrunich, S.I., Demchenko, V.L., Iurzhenko, M.V. (2022) Chemical welding of nanocomposites based on epoxy and oxidized graphene. *Avtomatychne Zvaryuvannya*, **4,** 50–53. DOI: https://doi.org/10.37434/as2022.04.07

ORCID
A.V. Vashchuk: 0000–0002–4524–4311,
S.I. Motrunich: 0000–0002–8841–8609,
V.L. Demchenko: 0000–0001–9146–8984,
M.V. Iurzhenko: 0000–0002–5535–731X,
M.O. Kovalchuk: 0000–0003–2161–643X,
E.P. Mamunya: 0000–0003–3855–2786

CONFLICT OF INTEREST
The Authors declare no conflict of interest

CORRESPONDING AUTHOR
M.V. Iurzhenko
E.O. Paton Electric Welding Institute of the NASU
11 Kazymyr Malevych Str., 03150, Kyiv, Ukraine.
E-mail: 4chewip@gmail.com

SUGGESTED CITATION
A.V. Vashchuk, S.I. Motrunich, V.L. Demchenko, M.V. Iurzhenko, M.O. Kovalchuk, E.P. Mamunya (2022) Chemical overlap welding of epoxy vitremers and their nanocomposites. *The Paton Welding J.*, **9**, 27–32.

JOURNAL HOME PAGE
https://pwj.com.ua/en

Received: 11.05.2022
Accepted: 11.11.2022

DOI: https://doi.org/10.37434/tpwj2022.09.06

MATHEMATICAL MODEL OF DETERMINATION OF RESIDUAL STRESSES AND STRAINS IN FRICTION STIR WELDING OF ALUMINIUM ALLOY

B.R. Tsaryk, O.F. Muzhychenko, O.V. Makhnenko

E.O. Paton Electric Welding Institute of the NASU
11 Kazymyr Malevych Str., 03150, Kyiv, Ukraine

ABSTRACT

A rater simple and efficient mathematical model of the process of friction stir welding (FSW) was developed, which is focused on fast determination of residual welding stresses and strains with engineering precision. The model is based on application of the method of thermoelastoplastic deformation of the material, which is used at modeling of arc welding, but instead of the model of arc heat source a model of heat evolution from the working tool friction against the material of the joint element was developed. The model also takes into account the conditions specific to FSW of rigid restraint of the joint elements during welding. The developed FSW model was used to conduct calculations of a butt joint of plates from AMg6 aluminium alloy and to present the results of the characteristic distribution of residual stresses and plastic strains, compared to arc welding of the butt joint. Calculation results derived using the developed model confirm the conclusions of other researchers that at FSW of aluminium alloys undesirable residual stresses and strains also form, but they are lower than with the traditional arc welding methods. Developed model can be effectively used for on-line calculation definition of residual stresses and plastic deformations in the zone of welded joints produced by FSW, with the purpose of further assessment of welded joint strength or prediction of general deformations of large-sized structures. Ways of further improvement of the developed model were outlined with the purpose of further increase of prediction accuracy, also by allowing for degradation of mechanical properties (softening) of the aluminium alloy during heating.

KEYWORDS: friction stir welding, aluminium alloy, residual stresses, plastic strains, mathematical modeling

INTRODUCTION

Nowadays the technology of friction stir welding (FSW) is becoming ever wider accepted when making butt joints of critical structures in such industries as aerospace, shipbuilding, automotive and railway transport, etc. Considering the high requirements to structures operating at high loads, determination of residual stresses and strains in FSW welded joints and development of the mathematical model of their determination is an urgent task.

During FSW, when the working tool, immersed into the welded joint metal, rotates and advances along the weld line, an intensive process of the tool shoulder friction against the surface of the joint elements and of the surface of the pin against the material occurs in the product volume. The process of metal stirring in the volume near the surface of contact of the pin and shoulder with the joint elements also takes place The tool shape and FSW process parameters can significantly influence the welded joint quality. [1, 2].

For effective modeling of this process, different researchers use diverse approaches, depending on the posed objectives. This can be prediction of the quality of welded joint formation for optimization of the welding technology or prediction of residual welding stresses and strains, which influence the performance of such a structure.

The simplest mathematical models of the heat source at FSW [3] define heat evolution only as a result of the process of the tool friction against the material of the joint elements. More detailed models further take into account the contribution of plastic strains into element heating. In such models [4, 5], in addition to the friction process, it is also necessary to predict the process of material stirring, so as to determine the balance of contributions of friction and plastic strains into the joint element heating.

In work [6] not a constant, but variable temperature-dependent coefficient is used in FSW model. In the mathematical model, presented in [6], also the amount of plastic work, converted into heat, is equal to 80 %, although the authors note that in many studies this value does not reach even 5 %.

In works [3, 5–9] the finite element model, alongside the welded joint, also includes the working tool and fixture for fastening its elements that allows determination of heat losses of the heating source into the tool and the fixture. Other researchers [4] use semi-analytical thermal model of FSW process which reduces the computation time.

All the models of the stress-strain state determination at FSW take into account the action of thermal stresses on the processes of elastoplastic deformation of the material during welding and further cooling [9]. The main feature of modeling the FSW process

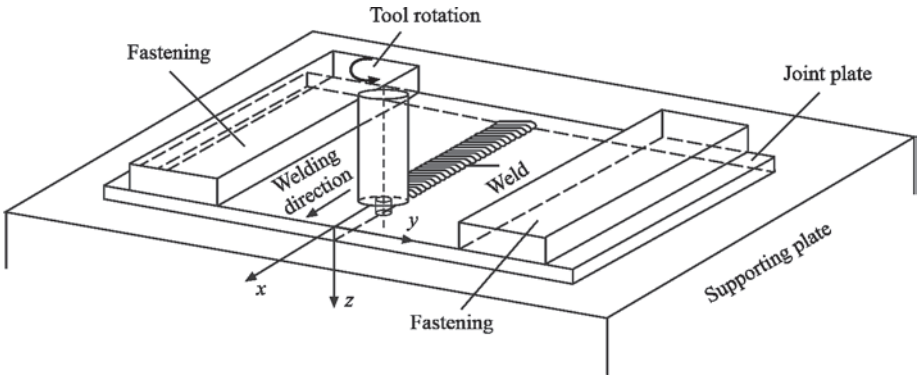

Figure 1. Scheme of FSW process

is rather rigid fastening of the joint elements during welding [6, 8].

MATHEMATICAL MODEL

Analysis of the available works on mathematical modeling of the processes of thermoelastoplastic deformation and mass transfer at FSW resulted in development of a rather simple model, aimed at quick determination of residual welding stresses and strains with engineering precision with the purpose of further assessment of welded joint strength, under the conditions of operational loading or prediction of total strains of large-sized structures with a large number of welded joints by shrinkage function method [10].

It is known that heat evolution at FSW, produced as a result of deformation, does not exceed 5 % of the total amount of heat evolution [11]. Thus, in the proposed model heat evolution from metal deformation can be neglected, for quick derivation of the data on residual welding stresses and strains at FSW of aluminium alloy elements. More over, in order to simplify the model, while preserving engineering precision of prediction, the following factors were ignored: dependence of the friction coefficient on material temperature, heat removal into the working tool and fixture for fastening the joint elements (supporting plate and clamps), partial lowering of heat evolution from friction as a result of material stirring, as well as the softening effect — lowering of mechanical properties of the aluminium alloy during heating [12].

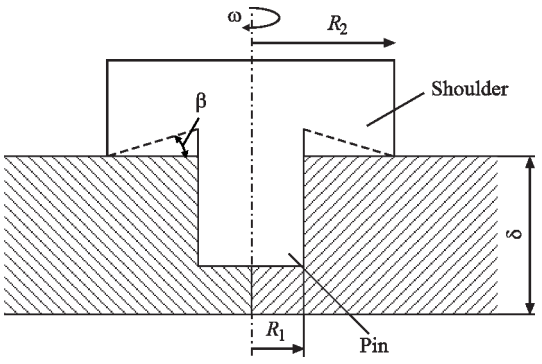

Figure 2. Scheme of the working tool in welding

Modeling of temperature fields at FSW was performed using the equation of nonstationary heat conductivity, which takes into account the bulk welding heat source $W(x, y, z, t)$

$$\frac{\partial}{\partial x}\left(\lambda\frac{\partial T}{\partial x}\right)+\frac{\partial}{\partial y}\left(\lambda\frac{\partial T}{\partial y}\right)+\frac{\partial}{\partial z}\left(\lambda\frac{\partial T}{\partial z}\right)+ +W(x,y,z,t)=c\rho\frac{\partial T}{\partial t}, \quad (1)$$

where ρ is the material density; c is the specific heat content, λ is the coefficient of heat conductivity.

In the general form for welded product at FSW (Figure 1) during the movement of the center (x_0, y_0, z_0) of working tool (Figure 2) at welding speed v_w the power of heat evolution per a unit of the area of contact between the tool and joint material in an arbitrary point (x, y, z) at moment of time t is described by the following dependence

$$-\lambda\frac{\partial T(x,y,z,t)}{\partial n}=\mu P_n\omega r, \quad (2)$$

- at $z = 0$ and $R_1 < r < R_2$ (on the surface in the tool shoulder zone),
- at $0 < z < \delta$ and $r = R_1$ (by thickness in the tool pin zone),

where μ is the friction coefficient; P_n is the normal force per a unit of area (pressure) in the contact point; ω is the angular speed of the tool rotation; $r=\sqrt{(x-x_0)^2+(y-y_0)^2}$ is the distance of the considered point of contact from the axis of working tool rotation (x_0, y_0); R_1 is the pin radius; R_2 is the shoulder radius; δ is the thickness of the elements being welded. The shoulder angle of inclination β can be ignored, as a small angles ≤ 2–3° the increase of the area of contact in the shoulder zone that does not exceed 5 %.

Boundary conditions on the surfaces of joint elements (Figure 3), taking into account the convective heat exchange with the environment, were assigned as follows:

$$q = -h(T_{out} - T), \quad (3)$$

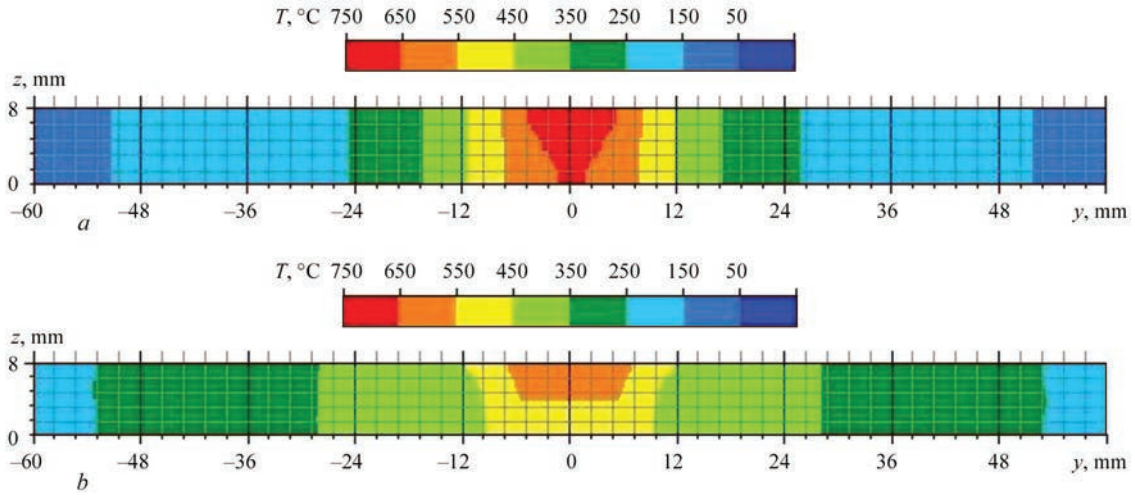

Figure 3. Results of numerical calculation of temperature distribution across the plate thickness in the cross-section in welding butt joints for a model of arc welding (*a*) of 500×500 mm plate, δ = 8 mm and model of FSW (*b*) of a 300×300 mm plate, δ = 8 mm

where T_{out} is the ambient temperature; q is the heat flow; h is the coefficient of heat transfer from the surface at convective heat exchange with the environment (usually under the conditions of natural convection in air T_{out} = 20 °C, h = 10–20 W/(m²·°C).

After establishing the temperature distributions at FSW numerical determination of the stresses and strains is conducted by a similar algorithm, as for arc welding, by successive observation during the occurrence of thermodeformational processes in the joint material from the beginning of heating to complete cooling by elastoplastic analysis and finite elements methods [13]. The difference of the model of stress and strain determination at FSW and model for arc welding is the condition of rigid fastening of the elements during welding and subsequent cooling, i.e. boundary conditions in the fastening zone along the entire length of the elements being welded are found at a short distance ≈ 30–40 mm) from the weld

$$U_x(x, y, z, t) = U_y(x, y, z, t) = \\ = U_z(x, y, z, t) = 0 \text{ at } |y| > y_w, \quad (4)$$

where U_x, U_y, U_z are the movements in the longitudinal and transverse directions and across the thickness of the joint elements; y_w is the distance from the welded joint axis to location of the fastening devices.

In the elastoplastic definition the strain tensor can be presented in the following form:

$$\varepsilon_{ij} = \varepsilon^e_{ij} + \varepsilon^p_{ij} \quad (i, j = x, y, z), \quad (5)$$

where ε^e_{ij}, ε^p_{ij} is the tensor of elastic and plastic strains, respectively. Components of tensors of stresses σ_{ij} and elastic strains ε^e_{ij} are related to each other by Hooke's law:

$$\varepsilon^e_{ij} = \frac{\sigma_{ij} - \delta_{ij}\sigma}{2G} + \delta_{ij}(K\sigma + \varphi), \quad (6)$$

where δ_{ij} is the unit tensor (δ_{ij} = 0, if $i \neq j$, δ_{ij} = 1, if $i = j$); $\sigma = \frac{1}{3}(\sigma_{xx} + \sigma_{yy} + \sigma_{zz})$; $G = \frac{E}{2(1+\nu)}$ is the shear modulus; $K = \frac{1-2\nu}{E}$ is the volumetric compliance, E is the Young's modulus; ν is the Poisson's ratio; φ is the function of relative elongations (volumetric changes), caused by temperature change:

$$\varphi = \alpha(T - T_0), \quad (7)$$

where α is the coefficient of relative temperature elongation of the material.

Plastic strains are related to the stressed state by the equation of the theory of plastic nonisothermal flow, associated with Mises yield conditions:

$$d\varepsilon^p_{ij} = d\lambda(\sigma_{ij} - \delta_{ij}\sigma) \quad (i, j = x, y, z), \quad (8)$$

where $d\varepsilon^p_{ij}$ is the increment of tensor ε^p_{ij} at the given moment of time t due to the deformation history, stresses σ_{ij} and temperature T; $d\lambda$ is the scalar function, which is defined by the yield conditions:

$$\begin{gathered} d\lambda = 0, \text{ if } f = \sigma_i^2 - \sigma_y^2(T) < 0 \\ \text{or } f = 0 \text{ at } df < 0; \\ d\lambda = 0, \text{ if } f = 0 \text{ and } df > 0; \\ f > 0 \text{ state is inadmissible,} \end{gathered} \quad (9)$$

where σ_i is the stress intensity

$$\sigma_i = \frac{1}{\sqrt{2}} \times \\ \times \sqrt{(\sigma_{xx} - \sigma_{yy})^2 + (\sigma_{xx} - \sigma_{zz})^2 + (\sigma_{yy} - \sigma_{zz})^2 + 6(\sigma_{xy}^2 + \sigma_{xz}^2 + \sigma_{yz}^2)},$$

$\sigma_i(T)$ is the material yield point at temperature T.

Mechanical and thermophysical properties of AMg6 aluminium alloy [13, 14]

T, °C	E, MPa	σ_y, MPa	ν	$\alpha \cdot 10^6$, 1/°C	λ, W(cm·°C)	$c\rho$, J/(cm^3·°C)
20	71440	155	0.324	22.7	1.18	2.40
100	68770	152	0.327	23.4	1.22	2.51
200	64790	149	0.332	24.5	1.27	2.62
300	60330	143	0.337	25.5	1.33	2.73
400	55400	98	0.343	26.6	1.38	2.85
500	49590	70	0.351	27.6	1.43	3.00

Note. σ_y — yield point. Material density $\rho = 2640$ kg/m^3, melting temperature range $T_{sol} = 560$ °C, $T_{liq} = 640$ °C, specific melting heat of fusion $Q_{liq} = 390$ kJ/kg [14].

In order to derive results for components of residual stresses σ_{ij} and stains ε_{ij}, the process of development of elastoplastic strains should be considered during a period beginning from a certain initial state. Traditionally used for this purpose is the method of successive observation, when for moment t the solution is sought, if the complete solution for moment $(t - \Delta T)$ is known, where Δt is the step of observation of the development of elastoplastic strains, within which it is possible to approximately assume that this development occurs by a fairly simple loading path. In his case, the connection between the end increment of the tensor of strains $\Delta\varepsilon_{ij}$ and tensor of stresses σ_{ij}, according to [13], can be written as:

$$\Delta\varepsilon_{ij} = \psi(\sigma_{ij} - \delta_{ij}\sigma) + \delta_{ij}(K\sigma) - b_{ij}, \qquad (10)$$

where ψ is the function of the material state in point (x, y, z) at moment t,

$$\psi = \frac{1}{2G} \text{ if } f < 0, \psi = \frac{1}{2G} \text{ if } f = 0, \quad f > 0 \text{ state is inadmissible;} \qquad (11)$$

b_{ij} is the tensor function of additional strains, which is determined by increment of $\Delta\psi$ volumetric

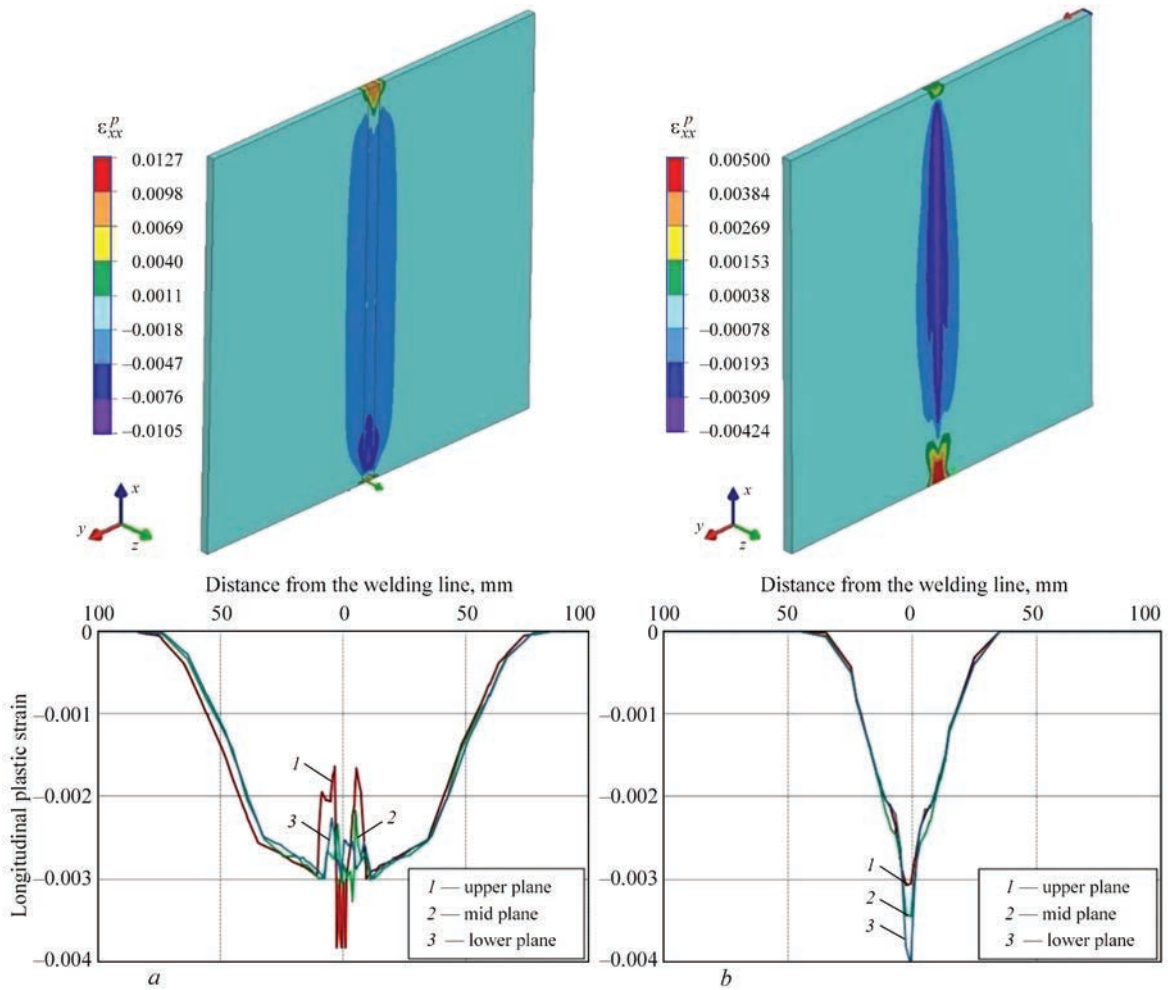

Figure 4. Results of numerical calculation of the distribution of longitudinal plastic strains for welded butt joints in the model of arc welding (*a*) of 500×500 mm plate; δ = 8 mm and model of FSW (*b*) of 300×300 mm plate, δ = 8 mm

changes and known results of the previous stage of observation:

$$b_{ij} = \left[\frac{\sigma_{ij} - \delta_{ij}\sigma}{2G} + \delta_{ij}(K\sigma) \right]_{t-\Delta t} + \delta_{ij}\Delta\varphi \quad (i, j = x, y, z). \tag{12}$$

Yield conditions in the form of (9) include considerable physical nonlinearity in the function of material state ψ, which is usually realized using iteration processes. As a result at each iteration, the physically nonlinear problem becomes a linear problem of the theory of elasticity with a changeable shear modulus, equal to 1/2ψ, and with additional strains b_{ij}.

MODELING RESULTS

The developed FSW model (1)–(12) was used for calculation of a butt joint of plates of a limited size (300×300 mm, δ = 8 mm, welding mode R_1 = 5 mm, R_2 = 10 mm, ω = 700 rpm, μ = 0.4, P_n = 70 MPa, v_w = 1.7 mm/s) and for presentation of the results of the characteristic distribution of residual stresses and plastic strains, compared to arc welding of a butt joint for a plate of 500×500 mm size, δ = 8 mm (TIG mode: I = 230 A, U = 15 V, v_w = 3 mm/s, efficiency η = 0.6). Mechanical and thermophysical properties of the material, depending on temperature, were taken as those for AMg6 aluminium alloy at modeling (Table).

The results of numerical calculation showed (Figure 3) that the maximum heating temperature at FSW (up to 500–550 °C) is much lower than at arc welding (up to 750 °C and higher) and higher, and it does not reach the melting temperature of the aluminium alloy T_{liq} = 650 °C. The longitudinal component of residual plastic strains at FSW is distributed in a narrower zone than that in arc welding, that is why the integral value of longitudinal shrinkage is approximately 3 times lower (Figure 4). The transverse component of residual plastic strains at FSW is 3 times lower by absolute value than in arc welding (Figure 5). Residual longitudinal stresses at FSW by the maximum value of tensile stresses (up to 150 MPa) are approximately equal to residual longitudinal stresses in arc welding, but the zone of tensile stresses at FSW is much (3 times) narrower (Figure 6). Residual transverse stresses at FSW (up to 14 MPa) are much lower by absolute value than in arc welding (up to 40 MPa) (Figure 7).

Thus, the calculation results obtained using the developed FSW model confirm that undesirable residual

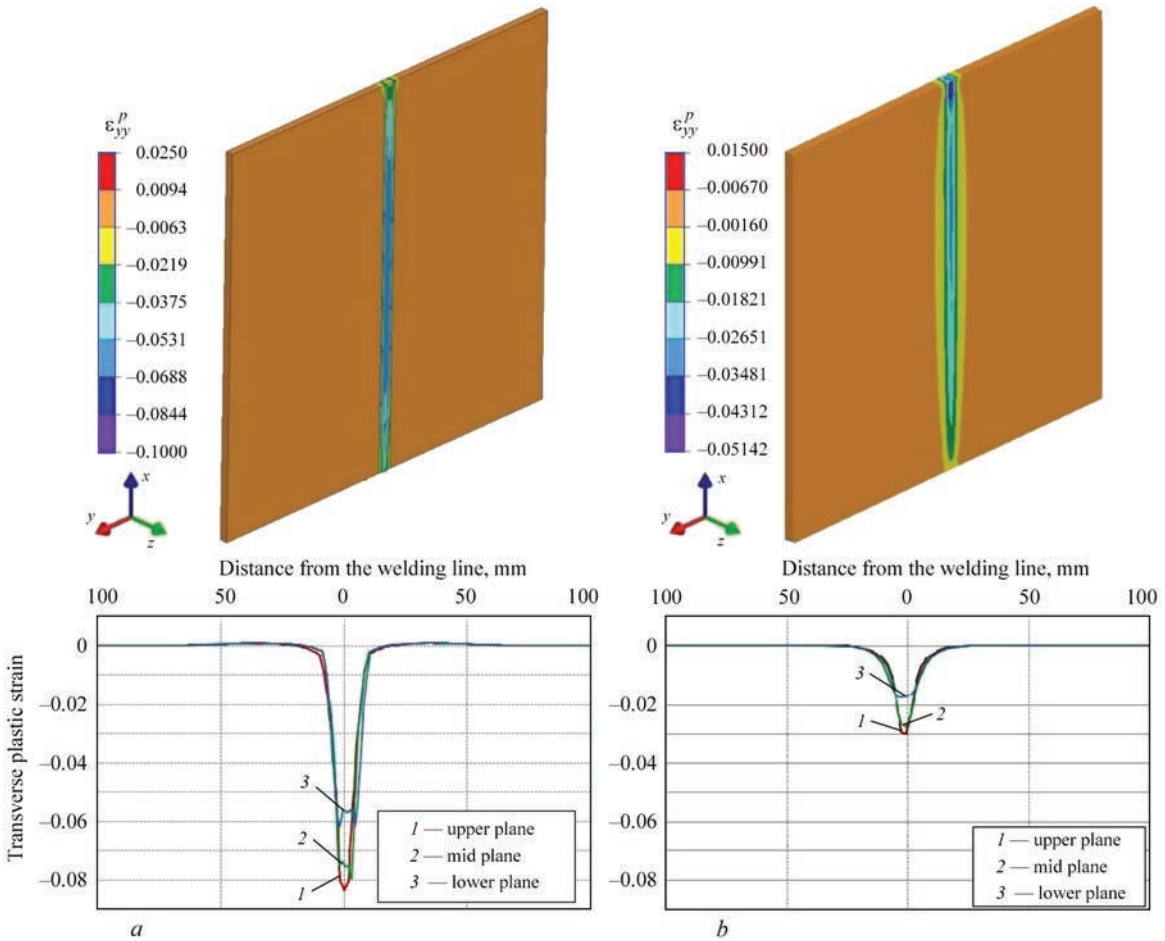

Figure 5. Results of numerical calculation of the distribution of longitudinal plastic strains for welded butt joints in the model of arc welding (*a*) of 500×500 mm plate, δ = 8 mm and model of FSW (*b*) of 300×300 mm plate, δ = 8 mm

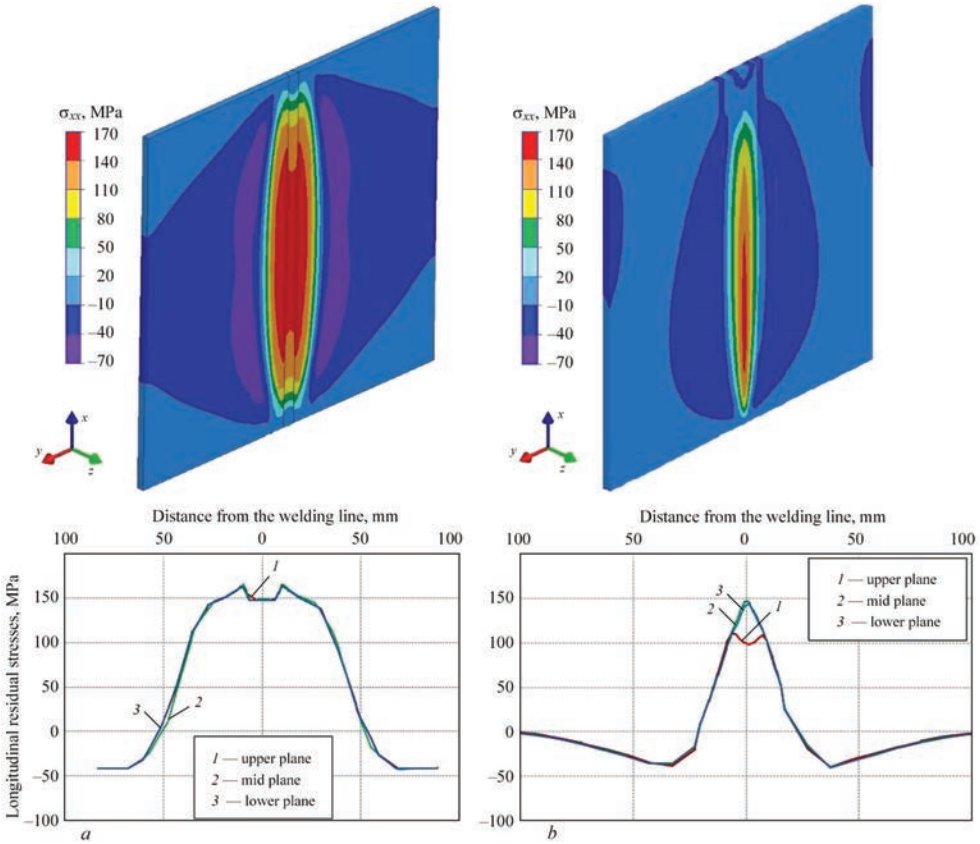

Figure 6. Results of numerical calculation of the distribution of longitudinal plastic stresses for welded butt joints in the model of arc welding (*a*) and model of FSW (*b*)

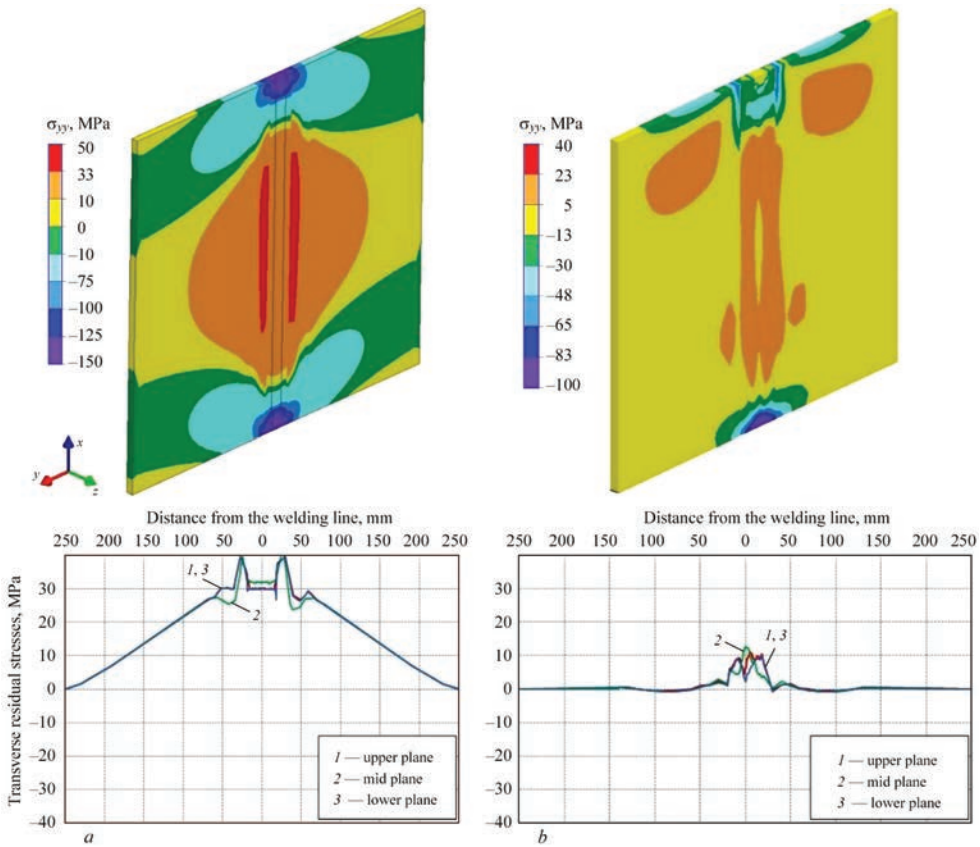

Figure 7. Results of numerical calculation of the distribution of transverse plastic stresses for welded butt joints in the model of arc welding (*a*) and model of FSW (*b*)

stresses and strains form in FSW of aluminium alloys. The residual stresses (particularly the longitudinal component) are close by their magnitude and distribution nature to residual stresses in arc welding, and the level of residual strains is much lower than in the traditional arc welding processes.

More over, there is a whole number of factors, which can influence the prediction accuracy of the developed model. This is, for instance, the dependence of friction coefficient on material temperature, removal of part of the heat into the working tool and fixture for fastening the welded joint elements, as well as partial reduction of evolution of friction heat as a result of material stirring and additional heat evolution from the material plastic strains. Taking these factors into account will, probably, allow more adequate determination of heat evolution in the heat source model, but will greatly increase the complexity of the mathematical model. There is, however, one factor which must be allowed for at FSW modeling in case of aluminium alloys: this is the softening effect, i.e. degradation of mechanical properties of the aluminium alloy in the HAZ. Therefore, at further improvement of the developed model it is rational to analyze consideration of these factors.

CONCLUSIONS

1. A calculation model was developed on the base of the approaches of thermoelastoplastic analysis for numerical determination of residual stresses and strains in the zone of welded butt joints of aluminium alloys produced by FSW. The model has the following main features:

- heat evolution from working tool friction against the joint material;
- conditions of rigid restraint of the joint elements specific to FSW;
- successive observation of the duration of thermodeformational processes in the joint material from the start of heating up to complete cooling.

2. Calculation results obtained from the developed model in welding 8 mm plates from AMg6 alloy confirm the conclusions of the other researchers that undesirable residual stresses and strains form at FSW of aluminium alloys, but their level can be lower than in the traditional arc welding processes. The longitudinal component of residual plastic strains at FSW is close by its magnitude, but it is distributed in a narrower zone, than in arc welding, so that the integral value of the defined longitudinal shrinkage is approximately 3 times lower. The transverse component of residual plastic strains at FSW is three times lower by its magnitude than in arc welding. Residual longitudinal stresses at FSW by the maximum value of tensile stresses (up to 150 MPa) are approximately equal to residual longitudinal stresses in arc welding, but the zone of tensile stresses at FSW is much narrower (3 times). Residual transverse stresses at FSW (up to 140 MPa) are much lower by its absolute value than in arc welding (up to 40 MPa).

3. In order to further increase the prediction accuracy of the developed model it is rational to perform analysis of allowing for such factors as: dependencies of the friction coefficient on material temperature, heat removal into the working tool and fastening fixture, reduction of heat evolution from friction due to material stirring, additional heat evolution due to material plastic strains, as well as degradation of aluminium alloy mechanical properties (softening) at heating during welding.

REFERENCES

1. İpekoğlu, G., Akçam, Ö., Çam1, G. (2018) Effect of plate thickness on weld speed in friction stir welding of AA6061-T6 Al-alloy plates. *The Paton Welding J.*, **12**, 7–11. DOI: https://doi.org/10.15407/tpwj2018.12.08
2. Krasnovsky, K., Khokhlova, Yu.A., Khokhlov, M.A. (2019) Influence of tool shape for friction stir welding on physicomechanical properties of zones of welds of aluminium alloy EN AW 6082-T6. *The Paton Welding J.*, **7**, 7–12. DOI: https://doi.org/10.15407/tpwj2019.07.02
3. Riahi, M., Nazari, H. (2011) Analysis of transient temperature and residual thermal stresses in friction stir welding of aluminum alloy 6061-T6 via numerical simulation. *Int. J. Adv. Manuf. Techn*., 55, 143–15. DOI 10.1007/s00170-010-3038-z
4. Ferro, P., Bonollo, F. (2010) A semi-analytical thermal model for friction stir welding. *Metallurg. and Mater. Transact. A*, 41, 440–449. DOI: 10.1007/s11661-009-0104-y
5. Majstrenko, A.L., Nesterenkov, V.M., Dutka, V.A. et al. (2014) Modeling of thermal processes for improvement of structure of metals and alloys by friction stir welding. In: *Proc. of 7th Int. Conf. (Ukraine, Odessa, 15–19 September 2014)*.
6. Aziz Saad, B., Dewan Mohammad, W., Huggett, D.J. et al. (2016) Impact of friction stir welding (FSW) process parameters on thermal modeling and heat generation of aluminum. *Acta Metall. Sin*. DOI: https://doi.org/10.1007/s40195-016-0466-2
7. Andrade, D.G., Leitão, C., Dialami, N. et al. (2020) Modelling torque and temperature in friction stir welding of aluminium alloys. *Int. J. Mech. Sciences*, 182. DOI: https://doi.org/10.1016/j.ijmecsci.2020.105725
8. Dresbach Christian, Marinus J. van Enkhuizen, Ulises Alfaro Mercado, Stefan Reh (2014) Simulation of thermal behavior during friction stir welding process for predicting residual stresses. *CEAS Aeronaut J*. DOI: https://doi.org/10.1007/s13272-014-0145-9
9. Meyghani, B., Awang, M., Emamian, S., Khalid Nor M. (2017) Developing a finite element model for thermal analysis of friction stir welding by calculating temperature dependent friction coefficient. In: *Proc. of 2nd Int. Conf. on Mech., Manuf. and Process Plant Eng*., 107–126. DOI: https://doi.org/10.1007/978-981-10-4232-4_9
10. Makhnenko, O.V. (2008) Combined application of method of thermoplasticity and method of shrinkage function for studying of hot straightening of shipbuilding panels. *Matematych-*

ni Metody ta Fizyko-Mekhanichni Polia, 51(**4**), 193–201 [in Russian].
11. Nandan, R., Roy, G.G., Lienert, T.J., DebRoy, T. (2007) Three-dimensional heat and material flow during friction stir welding of mild steel. *Acta Materialia*, **55**, 883–895. DOI: https://doi.org/10.1016/j.actamat.2006.09.009
12. Ishchenko, A.Ya., Podielnikov, S.V., Poklyatsky, A.G. (2007) Friction stir welding of aluminium alloys (Review). *The Paton Welding J.*, **11**, 25–30.
13. Makhnenko, V.I. (1976) *Calculation methods for study of kinetics of welding stresses and strains*. Kyiv: Naukova Dumka [in Russian].
14. Beletskij, V.M., Krivov, G.A. (2005) *Aluminium alloys (composition, properties, technology, application)*. Kyiv, Comintekh [in Russian].

ORCID
B.R. Tsaryk: 0000-0002-8929-7722,
O.F. Muzhychenko: 0000-0002-4870-3659,
O.V. Makhnenko: 0000-0002-8583-0163

CONFLICT OF INTEREST
The Authors declare no conflict of interest

CORRESPONDING AUTHOR
O.V. Makhnenko
E.O. Paton Electric Welding Institute of the NASU
11 Kazymyr Malevych Str., 03150, Kyiv, Ukraine.
E-mail: makhnenko@paton.kiev.ua

SUGGESTED CITATION
B.R. Tsaryk, O.F. Muzhychenko, O.V. Makhnenko (2022) Mathematical model of determination of residual stresses and strains in friction stir welding of aluminium alloy. *The Paton Welding J.*, **9**, 33–40.

JOURNAL HOME PAGE
https://pwj.com.ua/en

Received: 09.06.2022
Accepted: 11.11.2022

DOI: https://doi.org/10.37434/tpwj2022.09.07

MICROPLASMA SPRAYING OF COATINGS USING ZIRCONIUM WIRE

S.G. Voinarovych[1], D.L. Alontseva[2], O.M. Kyslytsia[1], S.M. Kaliuzhnyi[1], T.V. Tsymbalista[1], M.M. Dyman[1]

[1]E.O. Paton Electric Welding Institute of the NASU
11 Kazymyr Malevych Str., 03150, Kyiv, Ukraine
[2]D. Sekirbayev East-Kazakhstan Technical University
69 Protozanov Str., Ust-Kamenogorsk, Kazakhstan

ABSTRACT

The work is devoted to studying the process of microplasma spraying of coatings from zirconium wire. Technological possibility of formation of porous biocompatible Zr-coatings with bulk porosity in the range from 2 to 20 % and up to 300 μm size is demonstrated. It is shown that controlling the content of bulk porosity in Zr-coating allows changing elasticity modulus, reducing it by 14 times compared to the source cast material that allows getting closer to a bone modulus and reducing the stress shielding effect. The values of the adhesion strength of Zr-coating to the base from an alloy of VT6 grade were determined, its average value being higher than 26.9 ± 4.7 MPa and meeting the international requirements of ISO 13179-1:2021. Based on the obtained investigation results, the values of technological parameters were established for spraying of biocompatible Zr-coatings by the method of microplasma spraying of the wire from KTTs-110 grade alloy that allows forming functional coatings on the surface of different types of endoprostheses, which will provide a stronger and more reliable bonding of the endoprosthesis with the osseous tissue.

KEYWORDS: microplasma spraying, zirconium coating, endoprostheses, porosity, adhesion

INTRODUCTION

The development and application of biocompatible materials intended for using as substitutes for biological tissues and organs are one of the primary tasks of the modern materials science and medicine. Nowadays, in the world medical practice, metallic endoprostheses with a porous Ti-coating are most widely used [1]. Hip joint endoprostheses with Ti-coating on their surface are manufactured by well-known world manufacturers, including Procter & Gamble, DePuy, Stryker and are used as systems of cementless fixation in trauma medical practice [1, 2]. Nowadays, such cementless systems are implanted to patients of all ages and are getting ever more widespread due to the presence of a network of pores of a complex shape and a developed surface morphology, which promotes germination of osseous tissue, providing a reliable secondary fixation of an endoprostheses with a bone. An ingrowth of osseous tissues in the implant pores is a continuous process, which leads to the formation of three-dimensional lattices and a partial or complete filling of a porous space in Ti-coating [3, 4].

Analysis of literature sources shows different opinions regarding the optimal size of the coating pores for the implant surfaces. One of the researchers who dealt with the issue of establishing the regularities of the process of bone formation during implantation of hydroxyapatite ceramics with different sizes of pores to rats, were the staff scientists of the I.M. Frantsevich Institute of Materials Science of the NASU. In their research works, they used samples with pores in the ranges of 20–45, 80–150, 150–350 and 600–800 μm. According to the authors, more intense bone formation was observed at the sizes of pores of 80–150 μm [5]. The authors of [6] also showed that for a successful ingrowth of blood vessels it is necessary to provide the size of a pore of at least 150 μm.

However, from the results of the literature analysis, it is impossible to make a clear conclusion about the optimal size of pores, since this value is probably significantly dependent on the research conditions. Thus, in the range of 25–500 μm pores, the most positive effect on fixation and growth of pore cells was manifested by the pores of 25 and 200 μm, in the range of 85–325 μm — 325 μm, in the range of 75–900 μm — 400 μm, and in the case of studying a range of 300–1000 μm, the best fixation and growth of cells occurred at 600 μm [7].

In [8], the authors conducted studies on laboratory animals to determine the adhesion strength of cylindrical implants, made of a porous coating produced from titanium powder of different fraction, with adjacent osseous tissues. They showed that within 2–3 months, the shear strength reaches a maximum of 17–18 MPa in the range of pores sizes of 100–300 μm. At the same time, the pore larger than 300 μm reduced the adhesion strength of a bone with the implant. In addition, it was shown that the adhesion strength of

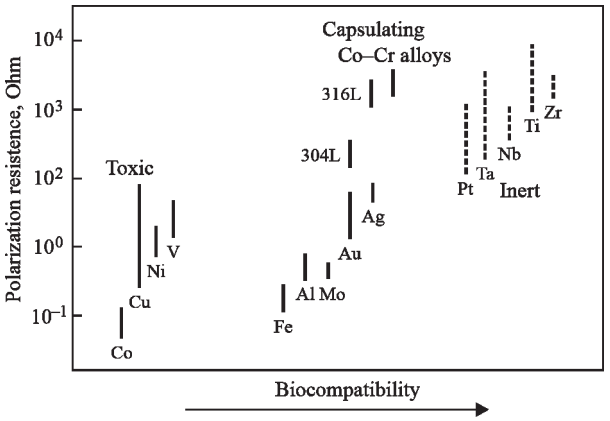

Figure 1. Relationship between polarization resistance and biocompatibility of pure metals, Co–Cr alloys and stainless steel [9]

the implants with an osseous tissue, on the surfaces of which, coatings from spongy particles were produced, having a microporous surface, is by 8–11 % higher than that in the implants produced from spherical powders. This is explained by the fact that in the case of a contact of the coating formed from spongy particles with an osseous tissue, a more closer bonding is formed due to a complex and developed configuration of a porous space.

In recent decades, there is a growing interest to more advanced materials that can be used in the manufacture of endoprostheses. One of such materials is zirconium that has high corrosion resistance, electrolytic neutrality and a necessary mechanical strength. Currently, taking into account the high biocompatibility of zirconium (Figure 1), the prospect of this material for using in the manufacture of endoprosthesis is considered [10].

According to the available literature data on the practical use of zirconium and alloys on its base, they are bioinertic materials that do not suppress the growth of osseous and soft tissues, and also do not cause visible morphological changes in inner organs [11].

At the same time, despite the progress in the use of zirconium and its alloys in the medical practice, insufficient attention is paid to the study of zirconium coatings and technologies of their spraying on the surfaces of different endoprostheses. One of such technologies that can be used to form biocompatible coatings on the surfaces of endoprostheses is microplasma spraying (MPS), developed by scientists of the PWI of the NASU [12, 13].

The aim of the work is to investigate the process of microplasma spraying of coatings from Zr-wire with the evaluation of the impact of MPS parameters on the structure, as well as mechanical characteristics of produced coatings, such as elasticity modulus and adhesion strength of a coating with a base.

EQUIPMENT, MATERIALS AND RESEARCH PROCEDURES

To conduct studies, the coatings were sprayed from Zr-wire of a solid cross-section of grade KTTs-110 with a diameter of 0.3 mm, on the surfaces of the samples from VT6 alloy. The chemical composition of the wire is shown in Table 1. Previousy, the surface of the samples was subjected to gas-abrasive treatment using a normal electrocorundum of grade 25AF-30 according to GOST 28818–90 at compressed air pressure of 0.6 MPa.

The Zr-wire spraying was carried out in the MPN-004 installation for microplasma spraying. This installation is designed for spraying wear-resistant, corrosion-resistant, thermal protective, biocompatible, decorative and other types of coatings used in various fields of engineering.

The MPN-004 installation consists of a power source and a panel for current, gas consumption and wire feed rate control. The plasma jet is formed by the microplasmatron of the original design using argon gas of the highest or the first grade. The feed of spraying wire materials is provided by the MP-04 feed mechanism, which is placed on the casing of the microplasmatron. The temperature mode of operation of the casing parts of the microplasmatron is provided by an autonomous cooling unit.

To carry out the experiments, in order to evaluate the influence of MPS parameters on the structure formation of zirconium coatings, the method of multifactorial planning of the experiment with a half-replica 2^{4-1} was chosen. As independent variable factors, current strength, plasma gas consumption, spraying distance and wire feed rate were chosen.

The microstructure and surface morphology of the produced Zr-coatings were studied in a scanning electron microscope SEM 515 (Philips, the Netherlands).

For the qualitative and quantitative analysis of a bulk porosity, an optical procedure (image analysis method) was used, which consists in determination of the area proportion, that contains detected pores, to the entire cross-sectional area of the coating. Digital images were processed with the use of Image-Pro Plus software (Media Cybernetics, USA), which allows measuring porosity (identifying inclusions that

Table 1. Chemical composition of Zr-wire of KTTs-110 grade, wt.%

Zr	Nb	Hf	Fe	Ca	O	Si	Ni	C	Cr
99.5	0.9–1.1	0.01	0.05	0.03	0.11–0.14	0.02	0.02	0.02	0.02

Table 2. Matrix of planning the experiment of MPS from Zr-wire

Mode number	I, A	Q_{pl}, l/h	H, mm	V_w, m/min
1	26	240	120	4.8
2	26	240	40	2.9
3	26	160	120	2.9
4	26	160	40	4.8
5	16	240	120	2.9
6	16	240	40	4.8
7	16	160	120	4.8
8	16	160	40	2.9

differ in color and brightness) and determining the percentage of pores in the cross-sectional area of the coating.

Mechanical measurements of the adhesion strength of the coatings to the base were carried out by the method of a normal separation according to the adhesive procedure using VK-9 glue (Khimprom, Ukraine) in accordance with the ASTM C633-13(2021) standard in a mechanical rupture machine MTS318.25 (MTS Systems Corporation, USA) (Figure 2).

The procedure of studying the dependence of elasticity modulus on bulk porosity of the coating consisted in the three-point bending of coated samples when the coating is in the compression and in the tension zones and by recording the load diagram. The functional relationship between porosity and elasticity modulus of the coating was established by constructing linear regression curves by the method of least squares, a more detailed description of the procedure is presented in [14].

Figure 2. MTS318.25 testing complex with fixed Zr-coated samples

RESEARCH RESULTS AND DISCUSSION

To study the structure and bulk porosity of microplasma coatings from Zr-wire, coated samples were produced according to the matrix of the mathematical planning of the experiment (Table 2).

Analysis of the microstructure of the surfaces of the microplasma zirconium coatings showed that de-

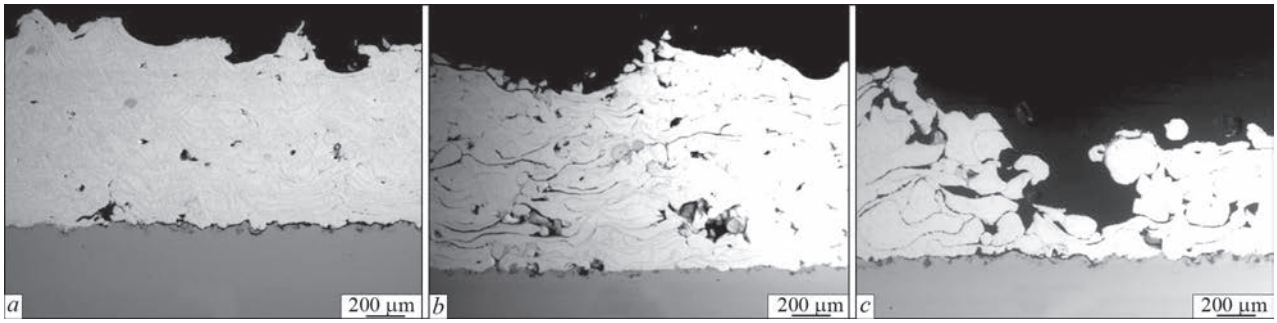

Figure 3. Microstructure of zirconium coating: *a* — mode 4; *b* —7; *c* — 8

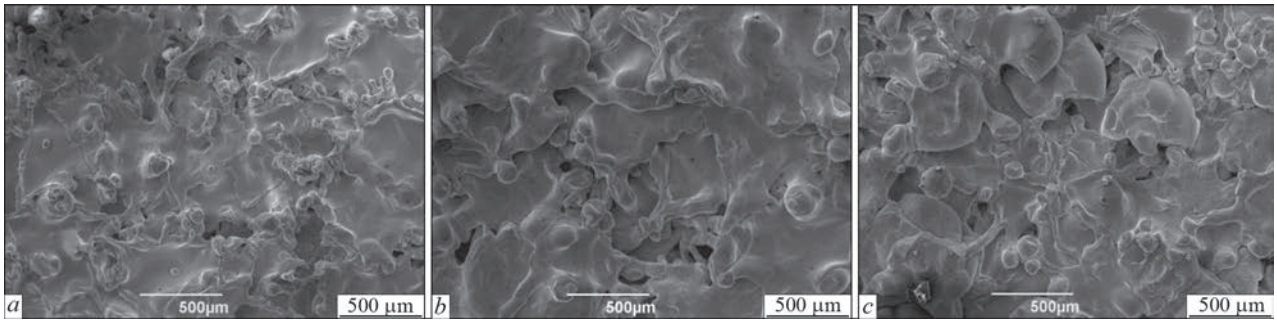

Figure 4. Morphology of zirconium coating surface: *a* — mode 4; *b* — 7; *c* — 8

Table 3. Average value of porosity of microplasma Zr-coatings depending on mode MPS parameters

Mode number	1	2	3	4	5	6	7	8
Porosity, %	3.5±0.14	4.0±0.02	6.0±0.4	2.8±0.1	8.7±0.78	3.6±0.14	8.3±0.72	20.3±2.0

pending on the technological mode of spraying, the coatings can be divided into 3 groups (Figures 3, 4):

1. If, when approaching the base, the particles are completely molten, then depending on their velocity, temperature before the impact, degree of their deformation and crushing during layering, the structures, shown in Figure 3, *a* can be formed. Such dense structures are formed from completely molten particles and have a typical, in most cases, lamellar structure (modes Nos 1, 2, 4, 6).

2. If, when approaching the base, together with the molten particles, the particles that began to solidify are present, then the structures are formed, which are characterized by lamellas of a greater thickness than in the structures of the 1st group, with a larger number of pores and partially deformed particles that were fixed (Figure 3, *b*). When the particles that began to solidify hit the surface of the base, the thermal and kinetic energy is not sufficient for a complete deformation of the particles, which, in the case of their significant number, leads to the formation of granular-disc-like and granular structures with the presence of pores. Such structures are typical for the coatings produced on the modes with a longer spraying distance (modes Nos 3, 5, 7).

3. If the coatings formation occurs from (partially) solidified (but those that are in a plastic state) particles and have an insignificant velocity, then the coatings are formed with a structure, that is characterized by a large number of bulk pores with a size of up to 300 μm (Figure 3, *c*). The coatings with such a structure cannot be produced in the case of forming coatings from powder materials, since a high probability of its destruction due to a low cohesive strength arises. This is explained by the presence of a significant number of unmolten particles with an insufficient volume of a liquid phase, the interaction of which does not provide strong bonds in the process of the coating formation. In the case of the wire spraying, when due to a short spraying distance and the process features, that guarantee a complete melting of sprayed particles in the plasma jet, which subsequently provides a collision of the particles with the base, that are completely or partially in the liquid phase, resulting in the formation of the coatings with a sufficient cohesive strength due to a larger area of mutual contact between the particles during their deformation.

The performed analysis of the surfaces of the produced Zr-coatings showed that the surfaces of the coatings have a developed morphology, which was formed from the molten and partially solidified particles that were fixed on the surface due to the existing liquid phase (modes Nos 4, 7, 8). Such particles provide the formation of a coating with a larger specific surface area, which contributes to the further reliable fixation of the implant in a bone.

The results of the studies of the average bulk porosity of Zr-coatings produced by the method of microplasma spraying on the modes, according to the matrix of the experiment, are presented in Table 3.

The analysis of the data on bulk porosity (Table 3) shows that the maximum values of bulk porosity of Zr-coatings produced on the mode No. 8, are 20.3 ± 2.0 %, and the pores size is in the range of 100–300 μm (Figure 4). The presence of such percentage of bulk porosity and the size of pores in the coatings on the surfaces of endoprostheses, according to literature data [1, 3], will contribute to germination of vessels to the pores of the coating, which will positively affect the formation and nutrition of an osseous tissue that will provide a reliable fixation and osseointegration of an endoprosthesis in the human body.

However, a considerable amount of bulk porosity in the coating can change the mechanical properties

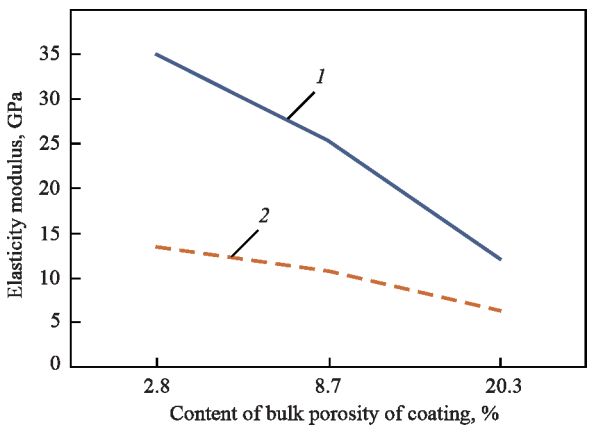

Figure 5. Dependence of elasticity modulus of Zr-coating on bulk porosity: *1* — butt; *2* — tension

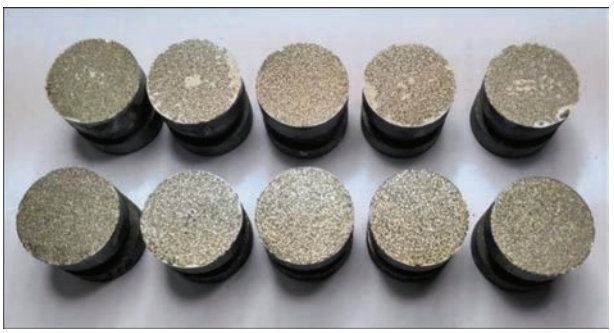

Figure 6. Nature of destruction of Zr-coated samples

of both the most formed coating as well as the entire structure as a whole [3]. From literature sources it is known that for some ceramic, metal and metal-ceramic materials, the value of bulk porosity significantly affects the value of elasticity modulus [15]. Previous studies on finding a functional relationship of bulk porosity with elasticity modulus showed that elasticity modulus of microplasma Zr-coatings depends on bulk porosity (Figure 5) [14]. An increase in bulk porosity of the coating allows changing elasticity modulus of Zr-coating, reducing it in the range: 13.5–6.5 GPa (tension) and 35–12 GPa (compression).

From the abovementioned it can be concluded that by changing the value of bulk porosity, it is possible to influence elasticity modulus of the coating and approach it to a bone modulus, which is 0.2–18 GPa [15]. This will provide a reduction in the stress shielding effect, that affects a bone resorption and ultimately will provide a more reliable fixation of a metal implant [16].

With an increase in coating bulk porosity, its mechanical properties are accordingly reduced, but they should meet certain requirements. In particular, for titanium coatings on the surfaces of endoprostheses, in accordance with the requirements of the international standard of quality ISO 13179-1:2021, the average static adhesion peel strength of the coating with the base should be greater than 22 MPa.

The obtained result of the study and calculation of the average adhesion strength of the microplasma zirconium coatings, sprayed (mode No. 8) to the base of VT6 alloy, is 26.9 ± 4.7 MPa. After mechanical tests, the zones of destruction of the coating–counter sample were evaluated (Figure 6), that showed the destruction occurs in the middle of the coating layer. The amount of the coating left on the surface of the base is more than 95 %. Therefore, the obtained value characterizes the cohesive strength of the coating. This indicates that the value of the average adhesion strength of the microplasma zirconium coating, sprayed to the titanium base, exceeds 26.9 ± 4.7 MPa and meets the requirements of ISO 13179-1:2021.

CONCLUSIONS

1. As a result of the analysis of literature data, the prospect of using Zr-coatings on the surfaces of parts of endoprostheses contacting with a bone, and the requirements for the coatings microstructure were determined.

2. The technological feasibility of forming porous coatings from Zr-wire with the adhesion strength of more than 26.9 ± 4.7 MPa with the base from VT6 alloy with the porosity from 2.8 to 20.3 % and the size of pores of up to 300 μm was shown.

3. It was found that controlling the content of bulk porosity of Zr-coating, it is possible to change elasticity modulus, reducing it by 14 times from the source material, which allows approaching the modulus of a bone and reducing the stress shielding effect, which will make possible to use these coatings on the surfaces to provide a more reliable and stronger adhesion between the implant and a bone.

The project was completed in the framework of financing by the National Academy of Sciences of Ukraine under a grant 0121U112006.

REFERENCES

1. Matassi, F., Botti, A., Sirleo, L. et al. (2013) Porous metal for orthopedics implants. *Clinical Cases in Mineral and Bone Metabolism*, 10(**2**), 111–115, PMID: 24133527. DOI: https://doi.org/10.11138/ccmbm/2013.10.2.111
2. Cizek, J., Matejicek, J. (2018) Medicine meets thermal spray technology: A review of patents. *J. of Thermal Spray Technology*, 27(**8**), 1251–1279. DOI: https://doi.org/10.1007/s11666–018–0798–8
3. Civantos, A., Dominguez, C., Pino, R.J. et al. (2019) Designing bioactive porous titanium interfaces to balance mechanical properties and in vitro cells behavior towards increased osseointegration. *Surface and Coatings Technology*, **368**, 162–174. DOI: https://doi.org/10.1016/j.surfcoat.2019.03.001
4. Liu, W., Liu, S., Wang, L. (2019) Surface modification of biomedical titanium alloy: Micromorphology, microstructure evolution and biomedical applications. *Coatings*, 9(**4**), 249. DOI: https://doi.org/10.3390/coatings9040249
5. Malyshkina, S.V., Dedukh, N.V., Gruntovsky, G.Kh. et al. (1998) Morphological features of osseous tissue change in plasty of defects by hydroxyapatite ceramics. *Ortopediya, Travmatologiya i Protezirovanie*, **3**, 110–114 [in Russian].
6. Dubok, V.A. (2000) Bioceramics – yesterday, today, tomorrow. *Poroshk. Metallurgiya*, **7–8**, 69–87.
7. Torres–Sanchez, C., Al Mushref, F.R.A., Norrito, M. et al. (2017) The effect of pore size and porosity on mechanical properties and biological response of porous titanium scaffolds. *Materials Sci. and Engineering: C*, 77, 219–228. DOI: https://doi.org/10.1016/j.msec.2017.03.249
8. Cook, S.D., Georgette, F.S., Skinner, H.B., Haddad, R.J (1984). Fatique properties of carbon- and porous-coated Ti–6Al–4V-alloy. *J. of Biomedical Materials Research*, **18**, PMID: 6736080. DOI: https://doi.org/10.1002/jbm.820180504
9. Kurodaa, D., Niinomib, M., Morinagac, M. et al. (1998) Design and mechanical properties of new β tipe titanium alloys for implants materials. *Materials Sci. and Engineering*, 243(**1–2**), 244–249. DOI: https://doi.org/10.1016/S0921–5093(97)00808–3
10. Pilipenko, N.N., Drobyshevskaya, A.A., Azhazha, R.V. et al. (2013) Zirconium-based materials for producing medical implants. *Zhurnal KhNU*, **1059**, 105–109 [in Russian].
11. Sherepa, K.M., Parfenov, A.V., Zyushmanovich, I.S. (1992) To problem of application of zirconium alloys for endoprosthesis and means of osteosynthesis. *Meditsinskaya Tekhnika*, **5**, 14–16. PMID: 1474864 [in Russian]
12. Borisov, Yu.S., Kislitsa, A.N., Vojnarovich, S.G. (2006) Peculiarities of the process of microplasma wire spraying. *The Paton Welding J.*, **4**, 26–31.
13. Alontseva, D.L., Borisov, Yu.S., Voinarovych, S.G. et al. (2018) Development of microplasma spraying technology

for applying biocompatible coatings. *Materials Physics and Mechanics*, **39**, 102–110. DOI: https://doi.org/10.18720/MPM.3912018_16
14. Moltasov, A., Dyman, M., Kaliuzhnyi, S. et al. (2022) Dependence of the elasticity modulus of microplasma coatings made of titanium grade VT1–00 and zirconium grade KTC-110 on their porosity. *Series on Biomechanics*, 37(**2**). DOI: https://doi.org/10.7546/SB.36.2022.02.14
15. Loskutov, V.S., Dekhtyar, L.I. (1985) Mechanical properties of plasma sprayed coatings of zirconium boride, copper, and composites of them. *Soviet Powder Metallurgy and Metal Ceramics*, 24(**7**), 570–572. DOI: https://doi.org/10.1007/BF00795194
16. *Mohamad Ikhwan Zaini* Ridzwan, Solehuddin Shuib, Hassan A.Y., Shokri A.A., Mohamad Ibrahim M.N. (2007) Problem of stress shielding and improvement to the hip implant designs. *J. of Medical Sciences*, 7(**3**), 460–467. DOI: https://doi.org/10.3923/jms.2007.460.467

ORCID
S.G. Voinarovych: 0000-0002-4329-9255,
D.L. Alontseva: 0000-0003-1472-0685,
O.M. Kyslytsia: 0000-0001-8894-4660,
S.M. Kaliuzhnyi: 0000-0002-8132-3930,
T.V. Tsymbalista: 0000-0001-9569-7776,
M.M. Dyman: 0000-0002-5886-1124

CONFLICT OF INTEREST
The Authors declare no conflict of interest

CORRESPONDING AUTHOR
S.G. Voinarovych
E.O. Paton Electric Welding Institute of the NASU
11 Kazymyr Malevych Str., 03150, Kyiv, Ukraine.
E-mail: serge.voy@gmail.com

SUGGESTED CITATION
S.G. Voinarovych, D.L. Alontseva, O.M. Kyslytsia, S.M. Kaliuzhnyi, T.V. Tsymbalista, M.M. Dyman (2022) Influence of parameters of magnetron sputtering Microplasma spraying of coatings using zirconium wire. *The Paton Welding J.*, **9**, 41–46.

JOURNAL HOME PAGE
https://pwj.com.ua/en

Received: 18.07.2022
Accepted: 11.11.2022

DOI: https://doi.org/10.37434/tpwj2022.09.08

HIGH PERFORMANCE EQUIPMENT FOR TANDEM MMA WELDING (SURFACING)

M.P. Drachenko, O.E. Korotynskyi

E.O. Paton Electric Welding Institute of the NASU
11 Kazymyr Malevych Str., 03150, Kyiv, Ukraine

ABSTRACT

In the paper special attention is given to application of pulsed-arc tandem welding by coated electrodes. Mock-ups of equipment for tandem welding and surfacing were developed and studied. A scheme was proposed for tandem arc welding by stick coated electrodes, including capacitive energy storage devices, as well as a device-attachment that allows using any welding current source to perform this kind of welding operations. The attachment operation is based on the principle of controlling the electrode melting rate that ensures their uniform mutual burnout. Also shown are time diagrams, which clarify the principle of operation of the device, photos of surfaced samples, oscillograms of currents supplied to the welding electrodes.

KEYWORDS: tandem arc welding, capacitive energy storage devices, pulse-time regulation of electrode melting rate

INTRODUCTION

Pulsed-arc welding now occupies one of the leading positions in engineering production and other industries. In this connection the questions of increasing the energy effectiveness of the power source for realization of various technological processes are becoming particularly relevant. At present more and more attention is given to design of equipment for tandem arc welding (TAW). As shown in [1], the main advantage of this welding process consists in improvement of the productivity and quality of the welded joints. At analysis of TAW a number of authors [2–4] pay special attention to the question of electromagnetic interaction of the electrode fields that influence the spatial state of the welding arcs. It is exactly their instability that leads to fluctuation of energy parameters of the process and thus influences the variation of welding parameters. As regards manual arc welding with stick electrodes, another advantage of the equipment for the tandem process should be noted which consists in a significant simplification of hardware realization of the equipment, in which electric energy storage devices based on supercapacitors are used.

The objective of this work is development and investigation of the electric and technological properties of the mock-up of the device for manual tandem arc welding (MTAW) with stick electrodes.

One of the first studies related to development of a device for MTAW, is a patent [5]. The disadvantages of equipment described in this patent are its bulkiness, need for two separate power sources, as well as inconvenience of operation. In this connection, we proposed a device [6] and a special kind of electrode holder, which do not have the above drawbacks.

One of the variants of application of such a structure is the hardware complex of the power source (PS)

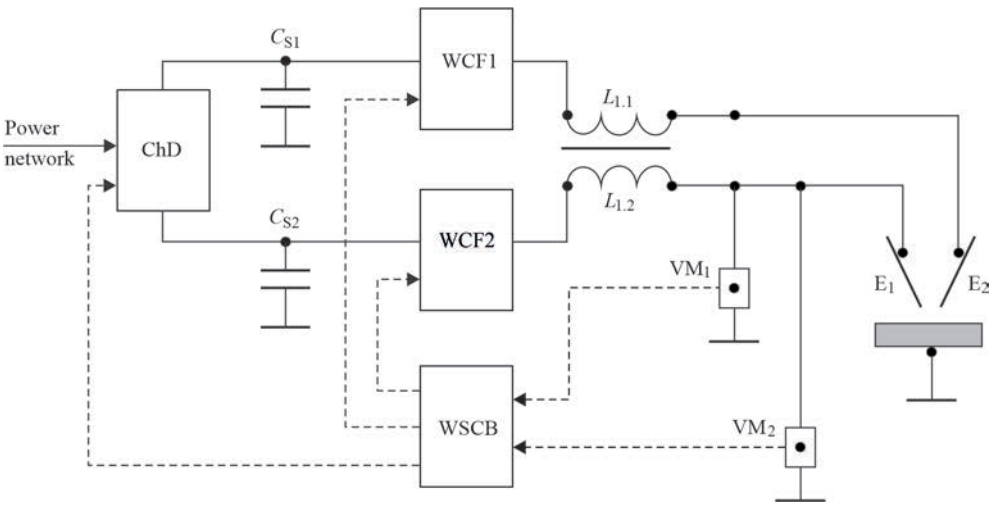

Figure 1. Block-diagram of two-channel source for TAW: ChD — charging device; C_{S1}, C_{S2} — capacitive electric energy storage devices; WCF1, WCF2 — welding current formers; WSCB — welding system control block; VM_1, VM_2 — voltage meter; $L_{1.1}$, $L_{1.2}$ — switching choke; E_1, E_2 — MMA welding electrodes

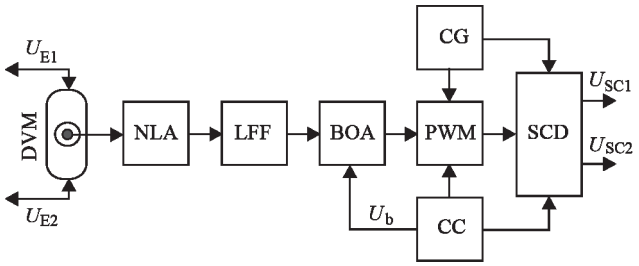

Figure 2. Block-diagram of the controller of electrode burnout rate equalizer at tandem MMA welding; DVM — differential voltage meter; NLA — normalizing logarithmic amplifier; LFF — lower frequency filter; BOA — balancing operating amplifier; PWM — pulse-width modulator; SCD — switch control driver; CG — clock generator; CC — control controller; U_{E1}, U_{E2} — voltages of welding electrodes; U_b — balancing voltages; U_{SC1}, U_{SC2} — switch control voltages

for tandem-MMA welding by a twin electrode, as well as its application for effective surfacing. A feature of such a PS is the possibility of a separate current supply to each of the electrodes. Here, regulation of this current can be independent or mutually synchronized. The block-diagram of such a PS is shown in Figure 1.

DESCRIPTION OF THE DESIGN OF THE DEVELOPED MOCK-UP

PS mock-up consists of the charging device block (ChD) which jointly implements the function of power factor correction (PFC). Its main purpose is transfer of the energy flow in the controlled mode to capacitive energy storage devices C_{S1}, C_{S2}, which are made of high-capacitance powerful capacitors, as well as current shape correction. The above-mentioned capacitors at the same time are energy sources for two welding current formers WCF1, WCF2, which are exactly the devices these forming currents I and I_2. The device operating algorithm is set by the welding system control block (WSCB). WSCB performs equalizing of currents of each of the electrodes by signals of voltage sensors VS_1, VS_2, which read the signals from the outputs of switching chokes $L_{1.1}$, $L_{1.2}$.

The scheme described in Figure 1 uses PFC, which is part of ChD module. This module is made by the classical scheme of step-up voltage converter [7], the load for which are storage capacitors C_{S1}, C_{S2}. On the other hand, connected to these capacitors are WCF1, WCF2 users of stored energy, which are voltage inverters designed by "skew bridge" scheme. Such a topology of the mock-up ensures galvanic decoupling of the output circuits of generation of mutually-independent welding currents.

CONTROL OF ELECTRODE MELTING RATE

At tandem-MMA welding the question of mutual equalizing of electrode melting rate is relevant. Usually, the electrode melting rate can be different, as a result of the influence of various destabilizing factors, leading to violation of the technological process and deterioration of the weld quality. Such defects are usually found at application of local PS for each electrode. It is particularly obvious in the case, when PS have steeply-falling VAC, or if not the same electrodes with different parameters are used. Therefore, at development of PS for tandem welding-surfacing (TWS) a relevant issue is monitoring and control of the electrode melting rate, which depends on electric power, supplied to the welding arc. Pulsed modulation of welding current is one of the methods to regulate the electrode melting rate. Regulation of power supplied to the welding arc is performed by selection of the pulse amplitude, pulse duration and pause duration.

In case of powering twin electrodes (tandem-welding) from locally independent welding PS with variable modulation of welding current pulses, the electrode melting rate can be regulated on the base of control of voltage difference across the welding electrodes. Realisation of the described algorithm is shown in Figure 2.

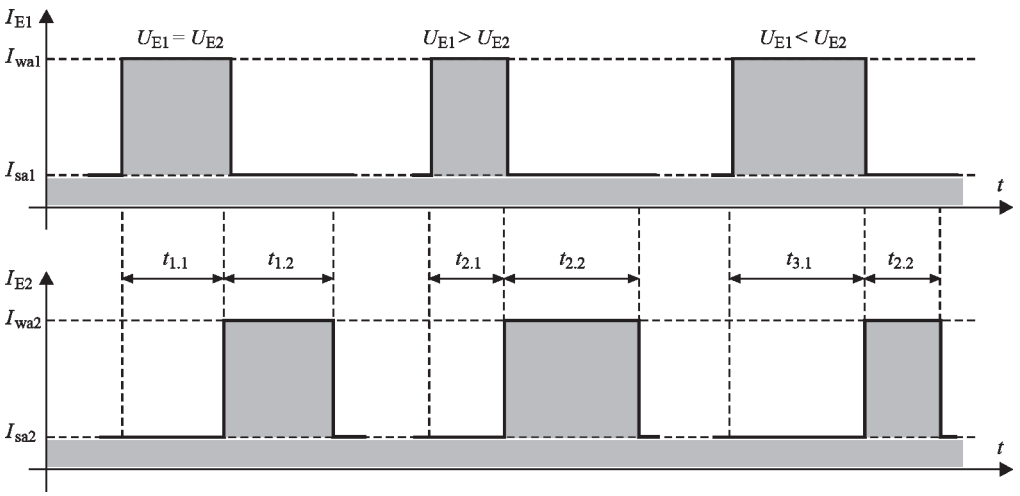

Figure 3. Diagram of operation of welding electrode melting rate equalizer: $t_{x.1}$ — first electrode welding current pulse duration; $t_{x.2}$ — second electrode welding current pulse duration; I_{wa1}, I_{wa2} — amplitudes of welding current pulses of the first and second electrodes ($I_{wa1} + I_{wa2}$); I_{sa1}, I_{sa2} — amplitude values of standby current of the first and second electrodes ($I_{sa1} + I_{sa2}$)

Figure 4. Photo of electrode holder with independent power source

Signals acting on the electrodes, are fed to the differential voltage meter (DVM), mounted at the device input. This signal proportional to voltage difference on welding electrodes $U_{E1} - U_{E2} = \Delta U_E$ is fed to the input of the normalizing logarithmic amplifier (NLA) which generates the required difference signal, and then it is applied to the input of balancing operating device (BOA), from the output of which the control signal comes to the input of pulse-width modulator (PWM).

Balancing of PWM operation is performed by voltage U_b applied to one of BOA inputs. Clock generator (CG) assigns the frequency of PWM operation and also controls the operation of power key switch control drivers (SCD). The latter generates the pulses of power key control voltage at its outputs. The diagram of SCD module operation is shown in Figure 3.

EXPERIMENTAL TRIALS OF PS MOCK-UP

A special electrode holder (Figure 4) with separate connections of each of the electrodes to different power sources was made to study the developed device (see Figure 1).

Experimental verification of operation of PS laboratory mock-up was performed in the following modes.

Figure 5. Surfaced samples produced with twin electrodes with independent power supply (for description of *a*, *b* see the text)

1. Welding mode — tandem movement of the electrodes (Figure 5, *a*).

2. Melting mode — frontal movement of the electrodes (Figure 5, *b*).

The modes of tandem welding with electrodes of the same or different grades were studied. The oscillograms of welding currents at application of different electrodes are shown in Figure 6, *b* and those with the same electrodes in Figure 6, *a*.

The oscillogram in Figure 6, *a* shows the mode, when the currents of the first and second electrodes are the same, and thus the total current (upper diagram) is a practically constant value.

The second oscillogram corresponds to the mode of different currents of individual electrodes. In this case, as one can see from Figure 6, *b*, the total current is pulsed with the frequency of 5 Hz. As was already noted, this frequency can be easily changed in real-time in a broad range of frequencies.

These surfacing current diagrams were derived, allowing for mode stabilization at technological procedures, which was performed by superposition of constant standby current on the arcs.

The technology of tandem arc welding (surfacing) can be realized using practically any standard welding machine. It requires developing an additional device,

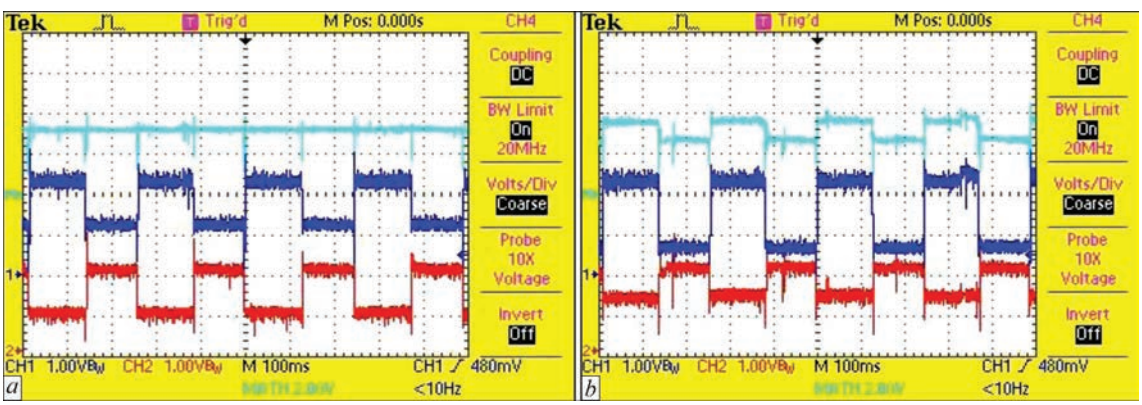

Figure 6. Oscillograms illustrating PS operation (for description of *a*, *b* see the text)

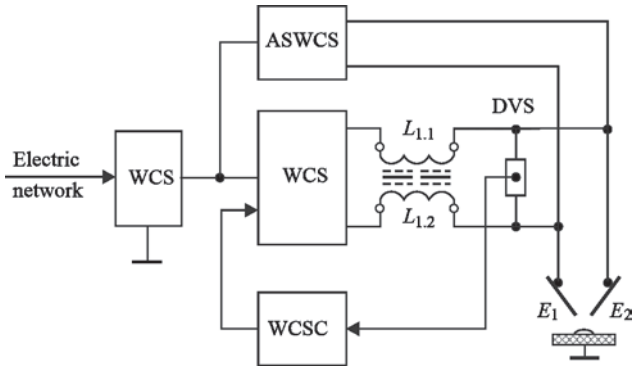

Figure 7. Functional block-diagram of the device-attachment for tandem MMA welding: WCS — welding current source; ASWCS — arc standby welding current source; WCS — welding current switch; WCSC — welding current switch controller; $L_{1.1}$, $L_{1.2}$ — switching inductances; DVS – differential voltage sensor; E_1, E_2 — MMA welding electrodes

which would generate two welding currents powering the respective stick electrodes.

Based on the results of technological tests of the developed mock-up (see Figure 1), we proposed, made and tested a special device for inverter power source of any type, which allows realization of the mode of pulsed-dosed tandem arc welding or surfacing by coated electrodes. Its block-diagram is shown in Figure 7, and its appearance — in Figure 8.

Here, stabilization and control of energy parameters of the technological process are performed by the welding current source, which can be any batch-produced welding system selected by the user. This greatly enhances the capabilities of the described process of tandem arc welding.

The main module of this device which realizes the technological process of tandem welding is welding current switch (WCS). Current distribution by the respective electrodes is performed by a specialized controller WCSC (welding current switch controller), as part of which the device operates (Figure 2). In order to ensure the high stability of welding arc burning, an additional block is envisaged in the developed device — the welding arc standby current source (WASCS).

Testing of this module was performed together with the batch-produced source, made by the ”skew” bridge scheme. Proceeding from the results of the performed work, it should be noted that the mode of pulsed-dosed energy transfer to the welding arc is quite promising for repair-restoration technologies.

CONCLUSIONS

1. A scheme of welding power source for TAW with stick electrodes is proposed in the work, which uses a rather simple control algorithm, based on the principle of time-pulse transformation of welding current.

2. Proceeding from the conducted studies, an original device for control of welding electrode melting rate was developed, for which a Ukrainian patent was obtained.

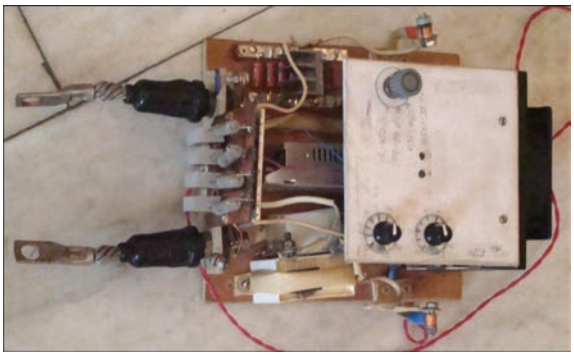

Figure 8. Device-attachment for tandem MMA welding

3. Experimental results of electric and technological tests of the developed power source are given, which confirm its high technical characteristics.

REFERENCES

1. Dilthey, U., Stein, L., Woeste, K., Reich, F. (2003) Latest development and trends in high-efficient welding technologies. *The Paton Welding J.*, **10–11**, 146–152.
2. Ueyama, T., Ohnawa, T., Yamazaki, K. et al. (2005) High-speed welding of steel sheets by the tandem pulsed gas metal arc welding system. *Transact. of JWRI*, 34(**1**), 11–18.
3. Tsybulkin, G.A. (2018) Effect of own magnetic fields on electric arcs in tandem-arc welding. *The Paton Welding J.*, **3**, 12–15.
4. (2021) *Welding by several electrodes*. Ukraine. https://msd.com.ua/svarka/
5. Knyazkov, A.F., Saraev, Yu.N., Timoshenko, A.K., Kolesin, S.A. (1983) *Method of twin-electrode welding with short circuits of arc gap and device for its realization*. RF Patent 998039 [in Russian].
6. Korotynskyi, O.E., Skopyuk, M.I., Drachenko, M.P. (2020) *Power source for tandem arc MMA welding*. Patent on utility model 140340, Ukraine [in Ukrainian].
7. Korotynsky, A.E. (2002) State-of-the-art, tendencies and prospects of development of high-speed welding converters (Review). *The Paton Welding J.*, **7**, 36–37.

ORCID

M.P. Drachenko: 0000-0002-4485-2403,
O.E. Korotynskyi: 0000-0002-6461-8980

CONFLICT OF INTEREST

The Authors declare no conflict of interest

CORRESPONDING AUTHOR

O.E. Korotynskyi
E.O. Paton Electric Welding Institute of the NASU
11 Kazymyr Malevych Str., 03150, Kyiv, Ukraine.
E-mail: epis@ukr.net

SUGGESTED CITATION

M.P. Drachenko, O.E. Korotynskyi (2022) High performance equipment for tandem MMA welding (surfacing). *The Paton Welding J.*, **9**, 47–50.

JOURNAL HOME PAGE

https://pwj.com.ua/en

Received: 29.05.2022
Accepted: 11.11.2022

DOI: https://doi.org/10.37434/tpwj2022.09.09

INFLUENCE OF THE PARAMETERS OF THE PROCESS OF PLASMA-ARC SPHEROIDIZATION OF CURRENT-CONDUCTING WIRE FROM LOW-CARBON STEEL ON THE GRANULOMETRIC COMPOSITION OF THE PRODUCED POWDERS

D.V. Strogonov[2], V.M. Korzhyk[1, 2], Yi Jianglong[2], A.Yu. Tunik[2], O.M. Burlachenko[2], A.O. Alyoshyn[3]

[1]China-Ukraine Institute of Welding, Guangdong Academy of Sciences,
Guangdong Provincial Key Laboratory of Advanced Welding Technology
510650, Guangzhou, China
[2]E.O. Paton Electric Welding Institute of the NASU
11 Kazymyr Malevych Str., 03150, Kyiv, Ukraine

ABSTRACT

The possibility of producing spherical powders by application of the technology of plasma-arc spraying of current-conducting wire of 1.6 mm dia. from low-carbon steel was experimentally confirmed. It was found that at different parameters of plasma arc spraying in the general case the main fraction of the powder is 25–250 μm fraction, which amounts to 95 % of the powder overall volume, quantity of particles of < 25 and 250–315 μm fractions in optimum spraying modes is at a rather low level and is not more than 5 %. The plasma-arc spraying mode was selected, which will ensure a change of the granulometric composition towards increase of the content of fine fractions (< 80 μm), which are in great demand in the field of additive 3D printing technologies: current — 280 A; wire feed rate — 12.0 m/min; arc gap length — 8 mm; plasma gas flow rate — 50 l/min; concurrent gas flow rate — 60 m^3/h; gap between plasma-forming and compression nozzle — 1 mm; cathode immersion depth — 1 mm. The shape and structure of the atomized particles was studied, most of which generally have a regular spherical shape. Here, the sphericity coefficient depends on process parameters and is equal to 0.7–0.9 on average at optimal spraying modes. In the total mass of the obtained spherical powders the share of satellites and isolated particles of an irregular shape is close to 1–3 %.

KEYWORDS: current-conducting wire, plasma-arc spraying; melt dispersion, powder spheroidization, solidification, spherical powder, mode parameters, granulometric composition

INTRODUCTION

Intensive development of powder metallurgy, additive technologies of 3D printing of metallic products (selective and direct laser melting and sintering (SLM, SLS, DMLS, granular metallurgy etc.)) requires creation of new materials in form of spherical granules and powders of complexly-doped alloys, refractory metals and intermetallics with set granulometric composition and rigid requirements to shape of particles (sphericity coefficient) and presence of minimum amount of defective particles [1].

The most widespread methods of production of such granules and powders are the technologies of gas atomization (GA) and plasma rotating electrode process (PREP) [2, 3]. However, regardless the large number of advantages these technologies have a series of disadvantages, including complexity of manufacture of < 100 μm powders; problems related to manufacture of rod stock for PREP; closed argon pores and relatively low sphericity coefficient for GA etc. [4, 5].

Today a technology of plasma-arc spraying being of a wide practical interest [6–9] is a perspective method for production of spherical powders with set granulometric composition. Among the advantages of this method are simplicity of the equipment that significantly simplifies the process of powder production and presence of large number of the parameters due to which it is possible to regulate the granulometric composition in a wide range as well as possibility of production of spherical powders of refractory materials [10–12].

Currently, there are not enough investigations on effect of the parameters of plasma-arc spraying mode on nature of distribution of sprayed particles on fractions, the results of the investigations are scattered, no information available on effect of some structural parameters of plasmatrons on change of granulometric composition of the particles being sprayed. Therefore, the aim of this work is investigation of effect of the mode parameters of plasma-arc spraying on a process of melt dispersion and change of granulometric composition of powder.

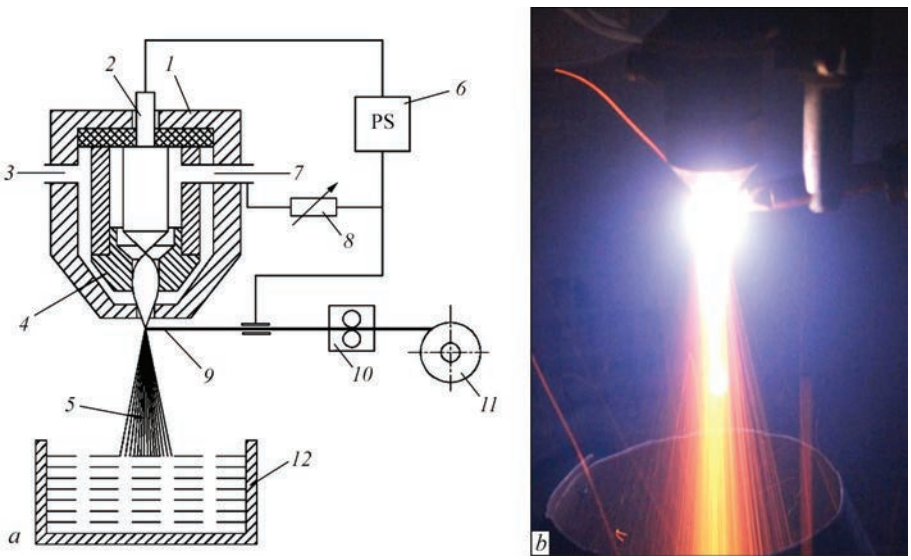

Figure 1. Scheme of the process of plasma-arc spraying and spheroidization of current-conducting wire (*a*) and appearance of spraying process (*b*): *1* — plasmatron operating chamber; *2* — rod electrode (cathode); *3* — channel for concurrent gas feed; *4* — plasma-forming nozzle; *5* — jet of particles being sprayed; *6* — power supply; *7* — channel for supply of plasma-forming gas; *8* — current-limiting resistor; *9* — wire (anode); *10* — feeding mechanism; *11* — wire coil; *12* — fridge with water

EXPERIMENT PROCEDURE AND EQUIPMENT

An essence of the process of plasma-arc spraying lies in melting of a current-conducting wire (anode) which is entered in a zone of high-speed plasma jet and further fragmentation of the melt stripping from a wire end [13]. An arc burns between a nonconsumable tungsten cathode and a current-conducting wire (anode) being fed through a plasmatron nozzle. Working (plasma-forming) gas entering an operating chamber is heated with an electric arc and comes out from the nozzle in form of a plasma jet. Open section of a discharge out of the plasma-forming nozzle is blown round by a gas flow coming out of a circular gap between the plasmatron nozzles [14]. Among the peculiarities of this method is the fact that melting and jet spraying of the wire material is carried out by argon plasma, meanwhile melt fragmentation and acceleration of disperse particles is performed by a jet of cold concurrent gas. This provides minimum losses on evaporation of wire material (up to 2 %), obtaining the optimum fraction composition of disperse phase, reaching a near-sonic velocity by the particles of sprayed material etc. [15]. The technological experiments were carried out using a plasma-arc spraying unit PLAZER-30 [16], which was modified for realization of the process of spraying and spheroidization of steel wire and powder production (Figure 1).

Indicated equipment was used for examination of the granulometric composition of particles in spraying of low-carbon steel wire (anode) of ER70S-6 grade (Sv-08G2S) of 1.6 mm diameter (Table 1).

According to earlier obtained practical data, an optimum mode was selected using a criterion of visual assessment of shape of the plasma jet at its reaching a minimum opening angle and process stability. It was used for corresponding change of the parameters of mode in order to determine the effect of each of them on change of the particle granulometric composition. High grade argon I1 according to ISO 14175–2008 “Welding consumables — Gases and gas mixtures for fusion welding and allied processes” was used as a plasma-forming gas and air was used as a concurrent gas, nozzle diameter made 3 mm.

Effect of the variable parameters of spraying was investigated is the next ranges, namely current — 220–265 A, plasma-forming gas consumption — 30–70 l/min, concurrent gas consumption — 30–60 m^3/h, wire feed rate — 9.5–12.5 m/min, cathode-anode distance — 8–12 mm, gap between the nozzle and ring electrode — 1–3 mm, cathode immersion depth — 0–1 mm (Table 2).

Besides, there were considered such structural parameters of the plasmatron as a gap between inner and outer nozzle 1–3 mm, through which concurrent gas is passed constricting the plasma jet, and cathode immersion depth 0–1 mm (Figure 2).

Table 1. Composition of wire of 1.6 mm diameter of ER70S-6 (Sv-08G2S) grade, wt.%

Steel	C	Si	Mn	P	S	Cr	Ni	Fe
Sv-08G2S DSTU 2246–70	0.05–0.11	0.70–0.95	1.80…–.10	0.03	0.025	< 0.20	< 0.25	Base

Table 2. Experimental modes of plasma-arc spraying of wire from Sv-08G2S steel of 1.6 mm diameter

Number of mode	Current, A	Arc voltage, V	Consumption		Cathode–anode distance, mm	Length of cathode immersion, mm	Distance between the nozzles, mm	Wire feed rate, m/min
			argon l/min	air m^3/h				
1	220	75	40	48	8	0.5	2	10.5
2	235	76	–»–	–»–	–»–	–»–	–»–	–»–
3	250	80	–»–	–»–	–»–	–»–	–»–	–»–
4	235	72	30	–»–	–»–	–»–	–»–	–»–
5	–»–	76	40	–»–	–»–	–»–	–»–	–»–
6	–»–	78	50	–»–	–»–	–»–	–»–	–»–
7	–»–	69	40	36	–»–	–»–	–»–	–»–
8	–»–	76	–»–	48	–»–	–»–	–»–	–»–
9	–»–	79	–»–	60	–»–	–»–	–»–	–»–
10	–»–	76	–»–	48	8	–»–	–»–	–»–
11	–»–	82	–»–	–»–	10	–»–	–»–	–»–
12	–»–	93	–»–	–»–	12	–»–	–»–	–»–
13	–»–	72	–»–	–»–	8	0	–»–	–»–
14	–»–	76	–»–	–»–	–»–	0.5	–»–	–»–
15	–»–	77	–»–	–»–	–»–	1.0	–»–	–»–
16	–»–	84	–»–	–»–	–»–	0.5	–»–	–»–
17	–»–	76	–»–	–»–	–»–	–»–	–»–	–»–
18	–»–	69	–»–	–»–	–»–	–»–	3	–»–
19	–»–	76	–»–	–»–	–»–	–»–	2	9.5
20	–»–	76	–»–	–»–	–»–	–»–	–»–	10.5
21	–»–	76	–»–	–»–	–»–	–»–	–»–	11.5

The wire was sprayed in a vessel filled with water from distance 500 mm, time of spraying made 200 s. Selection of samples for examination of the granulometric composition of powder, morphology of surface etc. was carried out using a laboratory vibro shaker Analissettte 3 Spartan (Germany) with a set of sieves 25–500 μm, weight of the sample made not less than 100 g of powder. Examination of the grain- size composition of laboratory batches of the powder was carried out using the method of sieve analysis according to the procedure ISO 2591-1:1998 "Test sieving — Part 1: Methods using test sieves of woven wire cloth and perforated metal plate" with the help of vibro shaker Analissettte 3 Spartan with a set of sieves: 25–40, 40–63, 63-80, 80–100, 100–125, 125–160, 160–200, 200–250, 250–315, 315–400, 400–450, 450–500 μm [17]. Value of pressure of the plasma jet was measured from the nozzle section to substrate at distance of 100 mm using electron scales of RADWAG PS grade 1000/R2 using procedure [18]. Examination of shape of the particles, their microstructure was carried out using the methods of optical (microscopes UNITRON Versamet -2 and Neophot-21) and analytical scanning electron microscopy (PHILIPS SEM 515 microscope). Description of shape of the particles was performed using the procedure of ISO 9276-6:2008 standard "Representation of results of particle size analysis — Part 6: Descriptive and quantitative representation of particle shape and morphology" [19].

RESULTS OF EXPERIMENTS AND THEIR ANALYSIS

Experimental check of the size of dispersed particles showed that in spraying of current-conducting com-

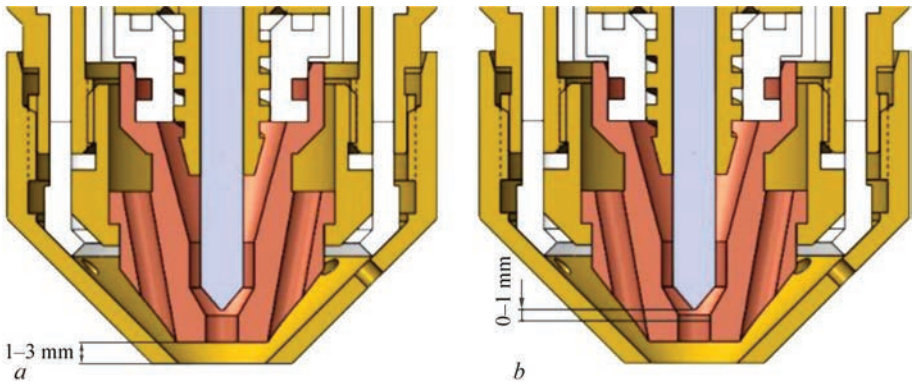

Figure 2. Investigated structural parameters of the plasmatron: *a* — gap between plasma-forming and constriction nozzles; *b* — distance at cathode immersion in relation to the nozzle

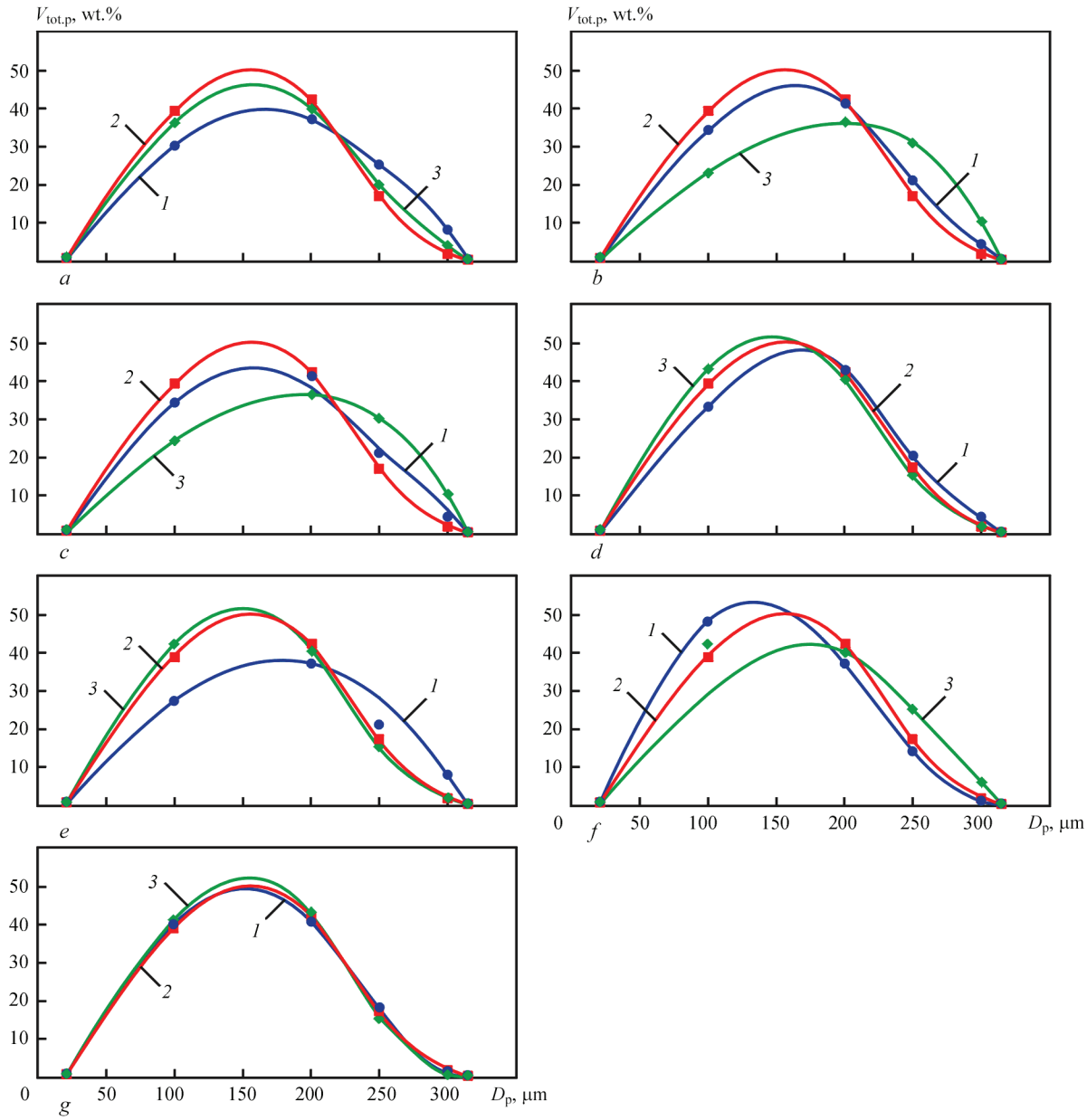

Figure 3. Dependence of granulometric composition of powder on current indices (*a*), A: *1* — 220; *2* — 235; *3* — 250; wire feed rate (*b*), m/min: *1* — 9.5; *2* — 10.5; *3* — 11.5; length of arc gap (*c*), mm: *1* — 8; *2* — 10; *3* — 12; consumption of plasma gas (*d*), l/min: *1* — 30; *2* — 40; *3* — 50; consumption of concurrent gas (*e*), m^3/h: *1* — 36; *2* — 48; *3* — 60; lengths of gap between plasma-forming and constriction nozzles (*f*), mm: *1* — 1; *2* — 2; *3* — 3; depth of cathode immersion (g), mm: *1* — 0; *2* — 0.5; *3* — 1.0

pact wire ER70S-6 the main fraction is 25–250 μm which makes 95 % of total weight of powder, amount of fraction particles < 25 μm and 250–315 μm at optimum modes of spraying is at sufficiently low level and do not exceed 5 %.

The curves of distribution of the granulometric composition of particles depending on spraying mode (Figure 3) were plotted. For convenience of description of these indices there was calculated an average diameter of the particles (D_p).

The analysis of obtained data revealed that increase of current from 235 to 250 A results in increase of the average size of particles by 7 % from 138 to 147 μm, respectively, and at 220 A current by 24 % from 138 to 171 μm (Figure 3, *a*). At that in both cases portion of the particles with size less than 80 μm decreases in the interval of values from 39 to 30 % of total powder weight ($V_{tot.p}$).

At visual evaluation of the spraying process it was observed that melting of the wire takes place mainly in a periphery part of the plasma jet.

The same effect reveals at increase of rate of wire feed from 10.5 to 11.5 m/min that results in rise of the average size of the particles by 33 % from 138 to 184 μm, respectively, and at wire feed rate from 9.5 m/min by 9 % from 138 to 151 μm (Figure 3, *b*). At that in both cases the portion of particles with size less than 80 μm decreases in the interval range from 39 to 23 % from powder total weight.

Authors of works [20, 21] explain the change of granulometric powder composition to the side of coarser fraction by the fact that due to change of the indices of current from some optimum value the wire melting takes place, mainly, in the periphery zone of the jet where its gas-dynamic pressure and level of concentration of energy significantly lower than along the axis. This creates the prerequisites for drop transfer of metal.

In order to investigate the phenomenon there was carried out spraying at current rise to 265 A and wire feed rate to 12.5 m/min. This mode provides location of an end of wire being sprayed along the axis of plasma jet due to what there is a change of granulometric composition of the particles to the side of smaller fraction, the average size of the powder decreases by 13 % to 120 μm. At that portion of the particles with size less than 80 μm rises from 39 to 44 % of total powder weight.

It is explained by the fact that increase of effective heat power of the plasma jet promotes a change of nature of transfer of electrode material from drop to spray one (due to decrease of surface tension forces at increase of overheating of liquid metal) that significantly rises outcome of small fraction of the powder [22, 23].

Increase of cathode–anode distance from 8 to 10 mm results to the fact that the average size of the particles rises by 11 % to 153 μm despite voltage growth from 76 to 82 V (Figure 3, *b*). Increase of distance to 12 mm promotes further rise of voltage from 82 to 100 V that leads to increase of power coming into the wire from 19 to 24 kW i.e. by 22 %. However, fractional composition of the particles shifts in a direction of coarser fractions, at that the average size of the particles increases by 34 % from 138 to 185 μm. Rise of length of the arc gap from 8 to 12 mm provokes decrease of portion of particles with sizes less than 80 μm in the interval of values from 39 to 24 % of total powder weight.

It is caused by decrease of a coefficient of anode heating due to rising loss of heat energy of the plasma jet on radiation and convection in a section of arc gap and drop of jet speed and, as a result, decrease of its dynamic effect on material being sprayed at increase of the distance from plasmatron nozzle [24, 25].

Consumption of the plasma-forming gas has more complex effect on the processes of dispersion of wire material melt than other parameters mentioned above (Figure 3, *d*). Thus, for example, increase of consumption from 30 to 40 l/min results in rise of dispersion of the sprayed particles. At that the average size of the granules decreases per 8 % from 150 to 138 μm, further shift of the fraction composition of particles takes place at rise of consumption from 50 l/min, the average size of particles drops by 4 % from 138 to 133 μm. However, further rise of consumption to 70 l/min leads to coarser fraction, the average size of the particles at that increases from 133 to 142 μm. Rise of the plasma gas consumption from 30 to 50 l/min provokes increase of portion of particles with size less than 80 μm from 39 to 43 % of the total powder weight.

Increase of gas consumption from 30 to 40 l/min and then to 50 l/min promotes rise of arc voltage from 72 to 76 and 80 V, respectively, due to its extension by gas flow, at that value of the arc gap is stable. This leads to growth of heat power and efficiency of wire heating, gives the possibility of rise of dynamic effect of the jet on the wire end (Table 2) and, thus, intensifies process of drops detachment from the wire end.

Nevertheless, further rise of gas consumption to 70 l/min results in a shift of fraction composition of the particles to the side of coarser fraction, at that the average size of the particles rises by 12 % from 138 to 154 μm. Further increase of consumption from 50 to 70 l/min provokes decrease of portion of the particles with size less than 80 μm from 43 to 36 % of the total powder weight.

This can be caused by cooling of the jet due to large heat expenses for heating of increased amount of the plasma-forming gas. Thus, it is necessary to note that at consumption of the plasma-forming gas less than 30 l/min there is an increase of wear of tungsten cathode.

Increase of consumption of a concurrent flow (air) from 36 to 48 m^3/h promotes rise of dispersion of the particles being sprayed, at that the average diameter of powder decreases by 21 % from 167 to 138 μm (Figure 3, *e*). Further increase of consumption of the concurrent flow from 48 to 60 m^3/ h does not provoke significant change of the granulometric composition, the average diameter of the particles decreases by 6 % from 138 to 129 μm. Increase of consumption of the concurrent flow from 36 to 60 m^3/h provides increase of the portion of the particles of size less than 80 μm from 32 to 41 % of the total powder weight.

Visual evaluation of the spraying process allows observing that in general case increase of consump-

Table 3. Calculation of forward pressure of plasma jet at 100 mm spraying distance

Number	Gas consumption, l/min	Area of spot being sprayed, mm^2	Pressure load, g	Forward pressure (σ), MPa
1	30	176	312	0.0177
2	40	181	356	0.0196
3	50	190	409	0.0215
4	70	212	514	0.0242

tion of the concurrent gas promotes more intensive constriction of the plasma jet that freely expends at the nozzle exit. This causes rise of a temperature gradient on the plasma axis jet, length and rate of its outcome [26]. Nevertheless, rise of consumption of the concurrent gas is possible to some conditions that are stipulated by plasmatron structure, namely inner intersection of a system of holes, through which concurrent gas passes. Also, it is necessary to note that at its consumption less than 36 m^3/h there is a decrease on average by 30–40 % of operation life of the inner plasmatron parts such as plasma-forming and protective nozzles.

Rise of the nozzle gap from 3 to 2 mm leads to decrease of fractional composition of the particles of finer fraction, the average diameter of the particles drops by 18 % from 163 to 138 μm and at 1 mm gap by 15 % from 138 to 117 μm (Figure 3, *f*). At that decrease of the gap between nozzles from 3 to 1 mm allows significantly rising portion of the particles with size less than 80 μm from 29 to 48 % of the total weight powder.

Change of the gap from 3 to 2 mm and then to 1 mm promotes increase of arc voltage from 69 to 76 and 84 V, respectively. It takes place due to change of an angle of interaction of concurrent flow and argon plasma that leads to more intensive local constriction of the plasma jet in the place of melting and detachment of drops of wire melt. This allows significantly rising rate of the jet and intensity of dispersion of the particles being sprayed. However, analysis of the appearance of the particles being sprayed shows that decrease of the gap from 3 to 1 mm leads to increase of a level of turbulence of the plasma jet that is observed in intensification of a process of drops coagulation at their collision between each other.

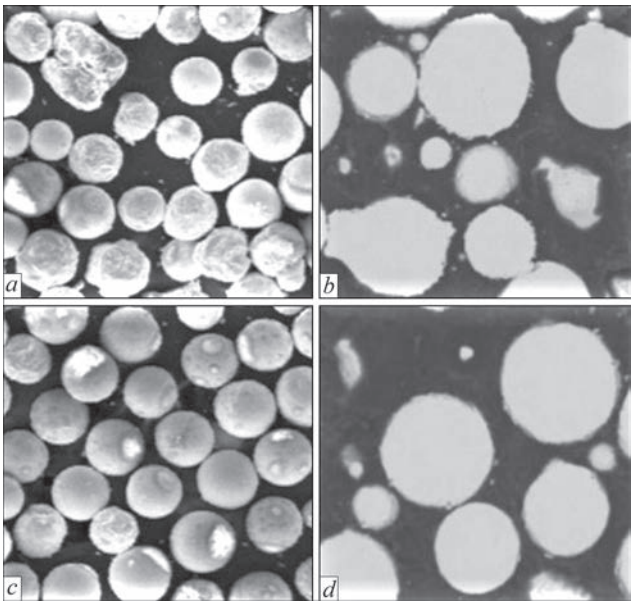

Figure 4. Morphology (*a*, *c*) and microstructure (*b*, *d*) of powders of 40–80 μm fraction obtained using the technology of plasma-arc spraying of compact wire ER70S-6 at inappropriate (*a*, *b*) and optimum (*c*, *d*) modes: I = 235 A; ω_{fw} = 9.5 m/min; l = 10 mm; G_1 (argon) = 30 l/min; G_2 (air) = 36 m^3/h (*a*, *b*); I = 235 A; V_{fp} = = 10.5 m/min; l = 8 mm; G_1 (argon) = 40 l/min; G_2 (air) = 48 m^3/min (*c*, *d*)

Increase of the immersion depth from 0 to 0.5 mm somewhat rises dispersion of particles being sprayed, their average size at that reduces by 5 % from 145 to 138 μm (Figure 3, *g*). Further increase of this value to 1.0 mm results in insignificant decrease of particles size to the side of finer fraction, change of the average size makes 2 %, i.e. a decrease from 138 to 134 μm. But we consider a change of fractional composition of the particles less than 80 μm then increase of depth of cathode immersion in the value interval from 0 to 1.0 mm allows insignificant rise of the portion of this fraction from 39 to 41 % of the total powder weight.

Change of the immersion depth from 0 to 0.5 mm and then to 1.0 mm promotes increase of arc voltage from 72 to 76 and 77 V, respectively, due to its extension and this results in small rise of heat power. Also, it is necessary to note that here the position of wire relatively to plasma-forming nozzle is stable, that gives the possibility to preserve initial dynamic effect of the jet on the wire end. However, further rise of cathode immersion depth deteriorates the conditions of arc stabilizing in the middle of a plasmatron operating chamber and creates the conditions for twin arc forming.

Thus, it is shown the possibility of regulation of the size of particles of obtained powder in a specific range of values of the granulometric composition by means of variation of the main technological parameters of the plasma-arc spraying of current-conducting wire. By the example of spraying of current-conducting wire of low-carbon steel ER70S-6 (Sv-08G2S) of 1.6 mm diameter it was determined an optimum mode, which will provide the maximum portion (60–75 %) of fine fractions (< 80 μm), which are of high demand in the field of additive technologies of 3D printing. They are current — 280 A; wire feed rate — 12.0 m/min; length of arc gap — 8 mm, consumption of plasma-forming gas — 50 l/min; consumption of concurrent gas 48 m^3/h; gap between plasma-forming and constriction nozzles — 1 mm; depth of cathode immersion — 1 mm.

The results of examination of morphology and microstructure of the particles of obtained powder show that in all examined powder samples the particles in general have regular spherical shape, at that the coefficient of sphericity depends on the parameters of the process and makes 0.7–0.9 at optimum spraying modes. The typical defects in the obtained powder are

the satellites, portion of which for the optimum modes of spraying on average not more than 1–3 %. Also, there are separate particles of irregular shape and particles with closed porosity.

Figure 4 demonstrates a comparative analysis of appearance of the particles, obtained at optimum and nonoptimum modes of the process of plasma-arc spheroidization. It can be seen that at inappropriate modes there is a larger amount of defective particles, the level of their sphericity is somewhat smaller (0.65–0.75). This is explained by the fact that melting and dispersion of the melt from wire end at optimum modes take place mainly on the plasma jet axis, where it is significantly larger gas-dynamic pressure and level of energy concentration than on the periphery. This creates the prerequisites for change of type of transfer of electrode metal from drop to spray one, rise of amount of fine disperse fraction, increase of heat of its overheating and, as a result, more effective spherical shape of the particles [27].

In this aspect it is necessary to note that plasma-arc spraying of steel wire was carried out in air atmosphere. This process of the wire end melting and melt dispersion is performed in argon plasma, however, solidification and formation of particles of the powders takes place in air atmosphere and in water that can be a factor effecting formation of indicated portion of the particles with closed porosity and of imperfect spherical shape.

CONCLUSIONS

1. It is shown the possibility of production of spherical powders by means of application of the technology of plasma-arc spraying of current-conducting wire of 1.6 mm diameter low-carbon steel. Heating and melting of electrode material (anode) was performed in argon shielding atmosphere and constriction and acceleration of the argon plasma jet, its protection from jet mixing with air atmosphere was carried out using concurrent high-velocity air flow being fed through circular gas between the plasma-forming and shielding plasmatron nozzles. Further movement of the sprayed particles and their solidification take place in air atmosphere and in water.

2. It is discovered that in general case the main fraction in plasma-arc spheroidization of low-carbon steel current-conducting wire is fraction of 25–250 μm, which makes 95 % of the total powder weight, amount of the particles of < 25 μm fraction and 250–315 μm under optimum spraying modes lies at sufficiently low level and does not exceed 5 %.

3. It is determined that among the examined technological parameters current, wire feed rate, arc gap length, consumption of concurrent gas and gap between plasma-forming and constriction nozzles have the highest impact on the granulometric composition of the obtained powders. Variation of indicated parameters can regulate the granulometric composition of the obtained powders in a wide range of values, namely obtaining powder fraction not less than 80 μm up to 48 % from their total volume, at that the average diameter of the particles can vary in 117–184 μm interval.

4. It was selected a mode of plasma-arc spraying, which would provide change of the granulometric composition to the side of content of fine fractions (< 80 μm), which are of high demand in the field of additive technologies of 3D printing, namely current — 280 A; wire feed rate — 12.0 m/min; length of arc gap — 8 mm; consumption of concurrent gas — 48 m^3/h; gap between plasma-forming and constriction nozzles — 1 mm; depth of cathode immersion — 1 mm.

5. It is shown that most of the particles in general have regular spherical shape, coefficient of powder sphericity makes on average 0.7–0.9. Portion of the satellites and separate particles of irregular shape makes around 1–3 % in the total weight of the obtained spherical powders.

The work was carried out under support of the following projects:

1. GDAS'Project of Science and Technology Development 2021GDASYL-20210302006;

2. Strategic project of the Academy of Sciences of Guangdong Province, (GDAS'Project of Science and Technology Development, 2020GDASYL-20200301001), China;

3. The National Key Research and Development Program of China — in the framework of the strategy «One Belt — One Road» (grant number 2020YFE0205300).

REFERENCES

1. Sun, P., Fang, Z., Zhang, Y. et al. (2017) Review of the methods for the production of spherical Ti and Ti alloy powder. *JOM*, **69**, 1853–1860. DOI: https://doi.org/10.1007/s11837-017-2513-5
2. Brika, S., Letenneur, M., Alex-Dion, C., Brailovski, V. (2020) Influence of particle morphology and size distribution on the powder flowability and laser bed fusion manufacturability of Ti–6Al–4V alloy. *Additive Manufacturing*, **31**, 732–748. DOI: https://doi.org/10.1016/j.addma.2019.100929
3. Yim, S., Bian, H., Aoyagi, K., Yamanaka, K. (2021) Spreading behavior of Ti–48Al–2Cr–2Nb powders in powder bed fusion additive manufacturing process: Experimental and discrete element method study. *Additive Manufacturing*, **73**, 337–353. DOI: https://doi.org/10.1016/j.addma.2021.102489
4. Nie, Y., Tang, J., Teng, J., Ye, X. et al. (2020) Particle defects and related properties of metallic powders produced by plasma rotating electrode process (PREP). *Advanced Powder Technology*, **31**, 2912–2920. DOI: https://doi.org/10.1016/j.apt.2020.05.018

5. Chen, G., Zhao, S., Tan, P. et al. (2018) A comparative study of Ti–6Al–4V powders for additive manufacturing by gas atomization, plasma rotating electrode process and plasma atomization. *Powder Technology*, **333**, 38–46. DOI: https://doi.org/10.1016/j.powtec.2018.04.013
6. *Advanced plasma atomization (APA) process*. https://www.advancedpowders.com/powders-every-technology
7. *Advanced plasma atomization process*. https://www.ge.com/additive/plasma-atomization-technology
8. Entezarian, M., Allaire, F., Tsantrizos, P. et al. (1996) Plasma atomization: A new process for the production of fine, spherical powders. *JOM*, **48**, 53–55. DOI: https://doi.org/10.1007/BF03222969
9. Petrunichev, V.A., Kudinov, V.V., Kulagin, I.D. (1965) Producing of spheroidized metallic powder by wire spraying. Izvestiya AN SSSR. Metally, **2**, 68–94 [in Russian].
10. Strukov, N.N., Shitsyn, Yu.D., Belinin, D.S. (2011) Controlling of powder particle size in plasma spraying of bar material. Vestnik PGTU, **3**, 117–121 [in Russian].
11. Bykovskiy, O.G., Lapteva, A.N., Mischenko, S.P., Pasko, N.N. (2015) Heat content and structure of particles in plasma spraying with a current-conducting wire. *Welding Inter.*, 30(**5**), 383–388. DOI: https://doi.org/10.1080/09507116.2015.1090168
12. Rusev, G.M., Rusev, A.G., Ovsyannikov, V.V. et al. (2013) Effect of mode parameters of plasma spraying using current-carrying wire on fractional composition of sprayed particles. *The Paton Welding J.*, **1**, 44–46. DOI: https://doi.org/10.15407/tpwj2013.01.02
13. Kudinov, V.V. (1966) Heating of current-conducting wire by constricted arc. *Svarochn. Proizvodstvo*, **4**, 11–13 [in Russian].
14. Korzhyk, V.M., Khaskin, V.Yu., Yao Yuhui et al. (2022) Influence of accompanying compressing air flow on the coating structure and properties in plasma-arc spraying by consumable current-conducting wire. *The Paton Welding J.*, **2**, 3–10. DOI: https://doi.org/10.37434/tpwj2022.02.01
15. Kharlamov, M.Yu., Krivtsun, I.V., Korzhik, V.N. et al. (2008) Effect of the type of concurrent gas flow on characteristics of the arc plasma generated by plasmatron with anode wire. *The Paton Welding J.*, **6**, 14–18.
16. Korzhik, V.N., Korob, M.F. (2012) Mechanized line PLAZER 30PL-W for plasma-arc wire spraying of coatings on large-sized parts of «shaft» type. Svarshchik, **4**, 13–15 [in Russian].
17. *ISO 2591-1:1988:* Test sieving — Pt 1: *Methods using test sieves of woven wire cloth and perforated metal plate*.
18. Bykovsky, O.G., Lapteva, A.N., Fomenko, A.V. et al. (2014) Influence of material kind and technology of spraying on plasma jet structure and its pressure on substrate. *Svarshchik*, **3**, 39–41 [in Russian].
19. *ISO 9276-6:2008:* Representation of results of particle size analysis — Pt 6: *Descriptive and quantitative representation of particle shape and morphology*.
20. Sytnikov, N.N. (1987) Influence of steel wire feed speed on nature of metal spraying with plasma jet. *Avtomatich. Svarka*, **8**, 63–64 [in Russian].
21. Karp, I.N., Rudoj, A.V. (1991) Influence of steel wire feed speed on dispersion of metal by air jet. *Avtomatich. Svarka*, **10**, 36–38 [in Russian].
22. Kudinov, V.V. (1966) Heating of current-conducting wire by constricted arc. *Svarochn. Proizvodstvo*, **4**, 11–13 [in Russian].
23. Bobrov, G.V., Privezentsev, V.I., Umnova, L.V. (1965) Formation of particles in melting of wire in plasma jet. *Poroshk. Metallurgiya*, **1**, 79–86 [in Russian].
24. Krasnov, A.N. (1965) Plasma spraying of tungsten. *Poroshk. Metallurgiya*, **3**, 1–5 [in Russian].
25. Krasnov, A.N. (1965) Plasma spraying of molybdenum. *Poroshk. Metallurgiya*, **1**, 1–5 [in Russian].
26. Gulyaev, I.P., Gulyaev, P.Yu., Korzhyk, V.N. et al. (2015) Experimental investigation of process of plasma-arc wire spraying. *The Paton Welding J.*, **3–4**, 36–41. DOI: https://doi.org/10.15407/tpwj2015.03.04
27. Petrunichev, V.A., Titkov, V.V. (1977) To mechanism of wire plasma spraying. *Fizika i Khimiya Obrabotki Materialov*, **1**, 14–16 [in Russian].

ORCID

D.V. Strogonov: 0000-0003-4194-764X,
V.M. Korzhyk: 0000-0001-9106-8593,
Yi Jianglong: 0000-0002-2018-713,
A.Yu. Tunik: 0000-0001-6801-6461,
O.M. Burlachenko: 0000-0003-2277-4202,
A.O. Alyoshyn: 000-001-9696-6800

CONFLICT OF INTEREST

The Authors declare no conflict of interest

CORRESPONDING AUTHOR

V.M. Korzhyk
E.O. Paton Electric Welding Institute of the NASU
11 Kazymyr Malevych Str., 03150, Kyiv, Ukraine.
E-mail: vnkorzhyk@gmail.com

SUGGESTED CITATION

D.V. Strogonov, V.M. Korzhyk, Yi Jianglong, A.Yu. Tunik, O.M. Burlachenko, A.O. Alyoshyn (2022) Influence of the parameters of the process of plasma-arc spheroidization of current-conducting wire from low-carbon steel on the granulometric composition of the produced powders. *The Paton Welding J.*, **9**, 51–58.

JOURNAL HOME PAGE

https://pwj.com.ua/en

Received: 17.06.2022
Accepted: 11.11.2022

NVO «Chervona Hvilya» is 25!

In September Kyiv PJSC “NVO Chervona Hvilya” celebrates its 25th anniversary.

From the moment of its foundation in the distant 1997, the Company’s history is inseparably connected with titanium production, as well as development and introduction of electron beam technologies.

Creation of the first in Ukraine full cycle of titanium ingot production became the initial goal of the young company’s activity. A shop section on quality preparation of titanium scrap for remelting was set up at the enterprise. A procedure for production of high-quality titanium ingots by electron beam remelting from the charge, completely consisting from scrap and wastes, was developed together with “Titan” Science-Production Center of the E.O. Paton Electric Welding Institute. As a result, inexpensive and high-quality ingots and slabs appeared in the world titanium market already one year after, which were purchased by titanium industry major players in the USA, Europe and China. NVO “Chervona Hvilya” quickly transformed from raw material exporter into titanium scrap importer and Ukraine’s largest exporter of titanium semi-finished products.

With time, most of the companies, which generated a lot of titanium wastes, decided to add electron beam melting furnaces to their traditional fleet of melting systems — and a real boom of such equipment began in the titanium world. Therefore, the owners of NVO “Chervona Hvilya” decided to refocus their activity from metal production to development of the most modern electron beam melting equipment: they had grounds to believe that no one else had such a combination of knowledge of the features of melting technology with their own real production practice.

With this purpose, a Design Bureau of Vacuum Metallurgy Equipment was established in 2005 with a team of high-class designers, engineers and technologists. The first large electron beam melting furnace for production of 10 t titanium ingots was designed and built already three years later. Then there were other projects, related not only to titanium, but also to other costly metals.

It should be noted that gas-discharge electron guns always were the base of all the company developments, both in terms of technology and design. A unique combination of exceptional technological capabilities, wide range of technical operating conditions and ease of maintenance made these guns an indispensable tool for many vacuum metallurgy processes. Gas-discharge electron beam guns of up to 600 kW power, developed by Company engineers are used all over the world for melting and refining titanium, niobium, tantalum, molybdenum, vanadium, zirconium, silicon and platinum in modern EB-PVD systems and for special welding applications.

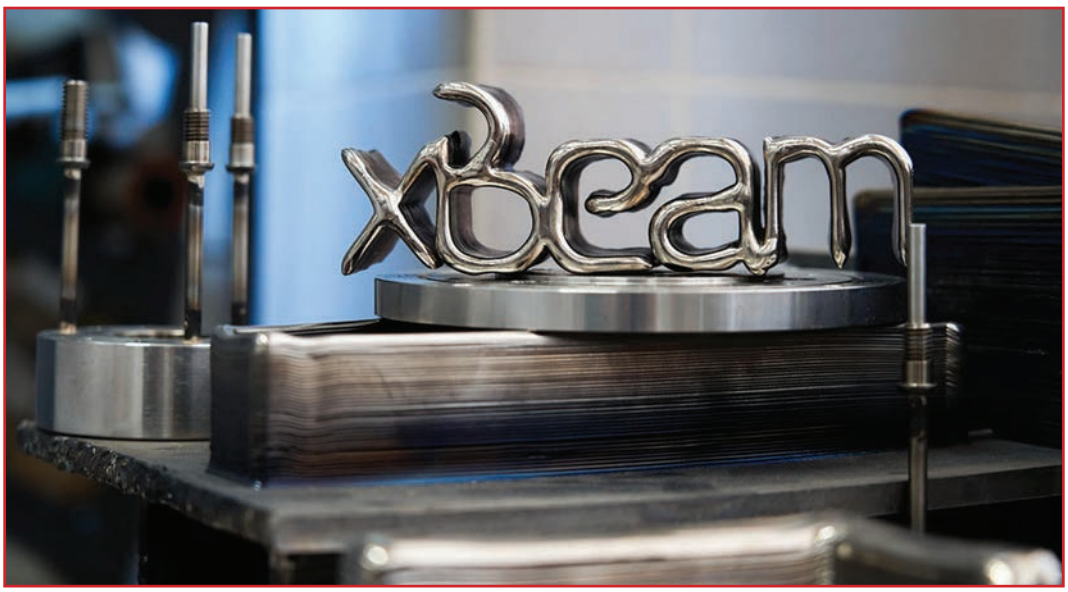

Exceptional ability of gas-discharge electron guns to directly generate profiled electron beams, including hollow ones, became a precondition for development in 2014 of the technology of 3D printing, known as xBeam 3D Metal Printing. This development became the start of a new stage in Company development in adaptive manufacturing sector. Technical characteristics of the special electron gun and features of

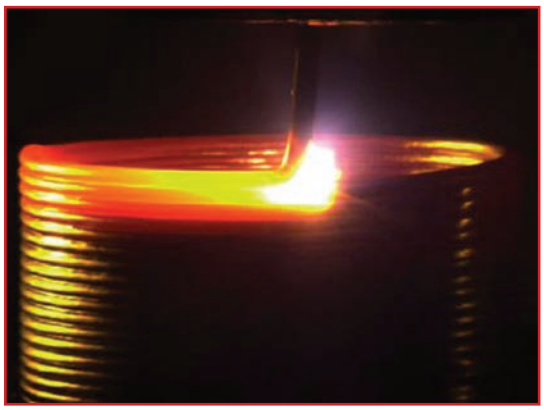

the technological process of deposition ensure significant competitive advantages of this technology. The first orders for 3D xBeam printing systems began coming already at the development stage. By that time independent investigations had already proved the possibility of 3D printing of titanium products, which by their properties are not inferior to the quality of the traditional forged metal that is critical for the aerospace industry.

Scientific investigations always had a special place in NVO "Chervona Hvilya" activity, as the Company's main business is development of high-tech equipment that requires both fundamental theoretical substantiation of the technological and engineering solutions and confirmation of the obtained results by profound studies of the structure and properties of metal products, manufactured by the developed procedures. A combination of extensive experience of Company engineers in design of vacuum systems with profound knowledge of the technologists on physical metallurgy allows not only competing with the best foreign technologies, but often surpassing them due to unconventional engineering solutions. Innovations developed by NVO "Chervona Hvilya" team are protected by patents and applications for inventions in Ukraine, USA, Germany, China, etc. Company's scientists and technologists are regular members and presenters at international conferences in the sectors of titanium production, electron beam and additive technologies.

Recently, the main direction of scientific-engineering research and development of NVO "Chervona Hvilya" is studying the technological capabilities of profiled electron beams, which can be generated by gas-discharge electron guns with different configuration of electrode systems. Successful scientific research activity of NVO "Chervona Hvilya" would be impossible without the procedural and practical cooperation with partners from academic and university environment, among which we can note G.V. Kurdyumov Institute of Metal Physics of the NAS of Ukraine, NTUU "Igor Sikorskyi KPI", TWI and University of Manchester (Great Britain), Shanghai University of Science and Technology (China), and, certainly, the E.O. Paton Electric Welding Institute of the NAS of Ukraine, with which the history of Company's development is closely connected from foundation and up to now.

At present NVO "Chervona Hvilya" continues developing and improving the technological and engineering base. The Company team consists of about twenty scientists, including one doctor and two candidates of science, engineers and designers, who have realized dozens of research and industrial projects.

During the entire 25 years of its history, the Company has relied on three main principles, namely proprietary technologies, proprietary equipment design and proprietary operation experience. It has always helped effectively covering the entire path from development to introduction and gaining recognition of leading companies all over the world.

We believe that our best developments are still ahead.

We invite you to cooperation.

Director of NVO "Chervona Hvilya"
Dmytro Kovalchuk

CHERVONA HVILYA
https://xbeam3d.com/